

Università di Pisa Department of Physics - Master Degree in Physics

$\begin{tabular}{ll} Muon momentum reconstruction in \\ Icarus-T600 LArTPC via multiple scattering \\ \end{tabular}$

Supervisor:

Candidate:

Giovanni Chiello

Co-supervisors:

Dr. Filippo Varanini

Prof. Simone Donati

Dr. Alberto Guglielmi

Contents

In	trod	uction		1
1	Act	ive an	d Sterile Neutrinos	Ę
	1.1	Neutr	ino phenomenology	٦
		1.1.1	Neutrino interactions	7
		1.1.2	Neutrino oscillations	Ć
	1.2	Oscilla	ation experiments	14
		1.2.1	Experimental anomalies	16
	1.3	Sterile	e neutrino models	19
		1.3.1	Status and perspectives	20
2	ICA	RUS	in the SBN program	23
	2.1	Short	Baseline Neutrino program	23
		2.1.1	Physics goals	25
		2.1.2	Neutrino beams	27
		2.1.3	Liquid Argon TPC	30
	2.2	The I	CARUS-T600 detector	32
		2.2.1	TPC read-out electronics	35
		2.2.2	Light Collection System	38
		2.2.3	Cosmic Ray Tagger	40
		2.2.4	Trigger system and DAQ	41
3	Eve	nt rec	onstruction in ICARUS	45
	3.1	Data	processing chain	45
		3.1.1	Calibration Ntuples	47
	3.2	TPC :	reconstruction	48
		3.2.1	Signal processing	48
		3.2.2	Hit finding procedure	50
		3.2.3	Pandora Pattern Recognition	52
	3.3	Energ	y reconstruction	57
		3.3.1	Calorimetric reconstruction	59
		3 3 9	Range-based reconstruction	6/

	3.4	Monte Carlo simulation	65
4	MC	S momentum reconstruction	69
	4.1	Multiple Coulomb scattering	70
		4.1.1 The Highland formula	72
		4.1.2 MCS as a tool to measure muon momentum	72
	4.2	"Gran Sasso" algorithm	73
		4.2.1 Measurement error contributions	75
		4.2.2 Estimate of muon momentum	76
	4.3	"MicroBooNE" algorithm	77
		4.3.1 Tuning of the Highland formula	78
		4.3.2 Estimate of muon momentum	80
	4.4	Comparison of the two algorithms	80
5	MC	S analysis on MC muon tracks	83
	5.1	Characterization of the muon sample	84
	5.2	"Gran Sasso" algorithm performance	89
		5.2.1 Combining the Collection plane with other planes	93
		5.2.2 Extension to 3D for the "Gran Sasso" algorithm	97
	5.3	"MicroBooNE" algorithm performance	98
	5.4	Results of analysis on MC muon tracks	100
6	MC	S analysis on real muon tracks	101
	6.1	Characterization of the muon sample	102
	6.2	"Gran Sasso" algorithm performance	105
		6.2.1 Combining the Collection plane with other planes	108
		6.2.2 Extension to 3D for the "Gran Sasso" algorithm	111
	6.3	"MicroBooNE" algorithm performance	112
	6.4	Results of analysis on real muon tracks	114
C	onclu	isions	115
\mathbf{A}	ppen	dix A: Covariance matrices	119
Bi	ibliog	graphy	123

Introduction

Neutrinos are among the most interesting particles to study, because they are the lightest and weakest interacting particles, yet they have had and continue to have a huge influence on the formation of the universe as we know it today. The more we learn about their behavior the closer we get to understanding how nature works. Nearly a hundred years have passed since Pauli's proposal, the first postulation about the existence of neutrinos, and we still struggle to comprehend their properties and their behaviour.

The discovery of neutrino oscillations, and its direct implication that neutrinos are massive particles — whereas the theory of the Standard Model (SM) predicts neutrinos to be massless particles — has represented a significant blow to the Standard Model and a strong hint in favor of Beyond the Standard Model physics. Additionally, despite well-established models of neutrino oscillations among the three active neutrinos, various anomalies have been recorded in short baseline experiments, leading to the hypothesis of at least one sterile neutrino and thus of a 3+1 neutrino mixing model. These anomalies were reported at accelerators (LSND, MiniBooNE), at Gallium-based experiments (GALLEX, SAGE), at nuclear reactors (for example, Neutrino-4). However, it is important to emphasize that globally the results do not agree with each other and, although each anomaly can be explained by a 3+1 model, no model is currently able to successfully fit all the experimental results at once.

The ICARUS T600 detector is a large-scale Liquid Argon Time Projection Chamber (LArTPC) operating as the far detector in the Short Baseline Neutrino (SBN) program at Fermilab. This program is based on three LArTPC detectors: SBND, MicroBooNE and ICARUS, positioned at different baselines along the Booster Neutrino Beam (BNB) — respectively 110 m, 470 m and 600 m. Additionally, ICARUS is gathering off-axis neutrinos from the Neutrinos at the Main Injector (NuMI) beam. The main physics goal of the SBN program is to conduct a definitive search for eV-scale sterile neutrinos by investigating both ν_{μ} disappearance and ν_{e} appearance in the BNB. Moreover, SBN will provide the opportunity to study ν -Ar cross sections in the energy range relevant to future long-baseline LArTPC-based experiments such as DUNE, and to search for BSM physics. The use of the LArTPC technology presents a significant advantage for ICARUS and SBN, enabling a precise three dimensional imaging of events at millimeter scale and accurate calorimetric reconstruction by matching information through the read-out of the drift electron signal by three anode wire planes with different orientations. This provides three

different reconstruction planes or reconstruction views: Induction-1, Induction-2 and Collection. Additionally, this technology enables a clear differentiation between photon and electron electromagnetic showers, and the rejection of the neutral current (NC) interaction background noise.

In a LArTPC the energy of photons and electrons can be reconstructed by accurate calorimetric measurements of the electromagnetic shower. In general, the energy of a fully contained charged particle – such as a muon – can be accurately measured by calorimetric techniques, through energy deposition, or with range-based techniques, from the distance traveled inside the detector or range using the continuous slowing-down approximation (CSDA). This method cannot be used for particles escaping the active volume – which are mostly muons. In the absence of a magnetic field Multiple Coulomb Scattering (MCS) serves as the only alternative for estimating the momentum of muons that escape the detector. This momentum measurement via MCS is particularly useful in those neutrino interactions within the energy range of 0 – 3 GeV, which are those occurring in the BNB and NuMI beams. A fraction of these muons generated in the ν_{μ} charged current (CC) interactions are emitted at large angles and escape the detector, thereby preventing a calorimetric or range-based energy measurement.

The ICARUS and the MicroBooNE collaborations have independently developed two different algorithms to determine the muon momentum via MCS techniques. For historical reasons, the first algorithm is called "Gran Sasso" algorithm – it was developed for ICARUS when it was still at Gran Sasso – and measures scattering angles in the 2D Collection view relying on a χ^2 -like function to determine muon momentum. The second algorithm, called "MicroBooNE" algorithm – it was developed for MicroBooNE – measures 3D scattering angles and performs a maximisation of the function that parametrizes the likelihood that the observed scattering angles match expectations for a given momentum. This thesis is the first attempt to apply these two algorithms to events collected by the ICARUS detector at FNAL. The sample I used consists in 2391 simulated stopping muon tracks and 2255 real stopping muon tracks, with momentum $0.4-1~{\rm GeV}\,{\rm c}^{-1}$. Stopping muons are chosen for this analysis since, for contained muons, momentum can be determined from range through CSDA; this momentum from range or $p_{\rm range}$ can be used as a benchmark for the momentum reconstructed via MCS, or $p_{\rm MCS}$.

I used two parameters to characterize the performance of these algorithms: bias and resolution. The bias quantifies the average difference between the reconstructed momentum p_{MCS} and the known momentum p_{range} , while the resolution quantifies the width of the distribution. Then, I developed an innovative version of the "Gran Sasso" algorithm that operates on all the three reconstruction views, rather than just the Collection view — as in the original version. Moreover, the momentum p_{MCS} in Collection view can be combined with p_{MCS} in Induction-2 view, or in Induction-1 view, or even with both: this slightly improve the performance in terms of bias and resolution. I developed also another version of the "Gran Sasso" algorithm, that works with 3D scattering angles: the characterization of this version, together with the "MicroBooNE" algorithm — intrinsically working with 3D angles — shows that the latter is slightly better.

In the sample of Monte Carlo stopping muon tracks, the "Gran Sasso" algorithm in the three reconstruction views shows a small bias and a resolution that depends on momentum as expected, ranging from about 32% at low momentum to 16% at high momentum; combining the views or switching to 3D slightly decrease the resolution, bringing it from 26% at low momentum to 14% at high momentum. In the sample of real stopping muon tracks, the bias is greater than that measured in the MC analysis, but still on the order of a few percent (< 10%) and this could suggest the presence of some detector effects not accounted for in the Monte Carlo, that increases at high momenta and should be further investigated. The resolution is slightly worse with respect to the resolution found for MC tracks, ranging from about 40% at low momentum to 18% at high momentum; combining the views or switching to 3D slightly decrease the resolution, bringing it from 32% at low momentum to 16% at high momentum.

The obtained results are significant from a physics perspective, as they will enable at least a twofold increase in the statistics of BNB ν_{μ} CC interactions and a threefold increase in the statistics of NuMI ν_{μ} CC interactions. This is crucial for improving the study of neutrino oscillations in the ν_{μ} disappearance channel and searching for 3+1 oscillations.

This thesis is organized as follows:

- 1. Chapter 1 presents an introduction of the present understanding of neutrinos and their interactions, and the phenomenon of oscillation, along with the most significant anomalies observed at short baselines and the hypothesis of sterile neutrinos;
- 2. Chapter 2 introduces the SBN program at Fermilab and the working principle of liquid Argon TPC, focusing on the ICARUS-T600 detector and its main components (the TPC in particular, the PMTs, the CRT, the trigger and the DAQ);
- 3. Chapter 3 describes the event reconstruction employed by the ICARUS detector and the main energy and momentum reconstruction techniques, that are calorimetric and range-based reconstruction techniques;
- 4. Chapter 4 explains the Multiple Coulomb Scattering theory and presents the developed algorithms designed to infer the muon momentum from MCS angle, the reasons why MCS is crucial to estimate momentum for muon exiting tracks, and the introduced improvements to the "Gran Sasso" algorithm;
- 5. Chapter 5 shows how these algorithms are applied to an ICARUS MC stopping muons sample, characterizing the performance of such algorithms in terms of bias and resolution;
- 6. Chapter 6 shows how these algorithms are applied to an ICARUS real stopping muons sample, comparing the results obtained with experimental muon tracks to those obtained with simulated muon tracks;
- 7. finally, results and future perspectives are summarized in the Conclusions.

Chapter 1

Active and Sterile Neutrinos

1.1 Neutrino phenomenology

The idea of neutrino was put forward by Wolfgang Pauli in 1930 [1] to explain how beta decay could conserve energy, momentum and angular momentum. Pauli imagined the existence of a new light neutral particle with ½ spin, undetected at that time, and he called it neutron using the same suffix used for naming the proton and the electron [2]. From 1920 to 1927 C. D. Ellis and W. A. Wooster further established that the beta decay spectrum is continuous [3] and thus not compatible with the discrete energy spectrum predicted by the energy conservation for a two-body decay; this was confirmed in an improved experiment by L. Meitner and W. Orthmann where it became evident that the energy per beta decay absorbed in a thick-walled calorimeter was equal to the mean of the electron energy spectrum and not to its maximum [4]. Such results hinted at only two possibilities: the conservation of energy is valid only statistically, which means this principle might be violated in any given decay - this was the possibility advocated by Niels Bohr – or the conservation of energy is always valid, but at the same time in such decays the electron was emitted together with another very penetrating radiation, consisting of new neutral particles [2]. This new particle was then called "neutrino" by Enrico Fermi in July 1932 during a conference in Paris and at the Solvay Conference in October 1933, and again in his first publication of a theory for beta decay [5].

The name *neutrino* was jokingly coined by Edoardo Amaldi during a conversation with Fermi at the Institute of Physics of via Panisperna in Rome, in order to distinguish this light neutral particle from Chadwick's heavy neutron [6]. Fermi describes the beta decay no more as a two-body decay but as a three-body decay, with a continuous energy spectrum that satisfies both the conservation of energy and angular momentum. According to Fermi's theory, neutron could decay in a proton, an electron and a neutrino in a simple reaction

$$n \to p + e^- + \overline{\nu_e} \tag{1.1}$$

Now we know that the product of neutron beta decay is an *electron antineutrino*, but at that time it was enough to unify Pauli's neutrino with Paul Dirac's positron and Werner Heisenberg's neutron–proton model, and to give a solid theoretical basis for future experimental work [7].

The hypothesis advanced by Bohr about the violation of the energy theorem had been ruled out by the experimental evidence of an upper bound in electron energy, bound that is not expected if the conservation of energy is invalid since any amount of energy would be statistically available in at least a few decays [2]. The natural explanation of the beta decay was at the end of the day the one proposed by Pauli, and he publicly emphasized that this undetected neutrino must have been an actual particle [8].

The first direct detection of a neutrino dates back to 1956, in an experiment conducted by C. Cowan and F. Reines at the Savannah River Plant. This experiment was based on the idea that a neutrino detection is *rare but not impossible* [9]: in fact, during the inverse beta decay process

$$\overline{\nu_e} + p \to n + e^+ \tag{1.2}$$

the positron quickly undergoes matter-antimatter annihilation yielding a prompt flash of light, while the neutron is captured and produces a delay light. The coincidence of both the events represents the unique signature of the interaction. After months of data taking, the results showed about three neutrino interactions per hour in the detector, and this allowed Reines and Cowan to claim the experimental discovery of the neutrino [10].

In 1962 the experiment at the Brookhaven National Laboratory confirmed that more than one type of neutrino exists, in particular they found a neutrino associated to the muon. In their experiment, Lederman, Schwartz and Steinberger used a beam of neutrinos created from the in-flight decay of pions and kaons; the products of such neutrino interactions were detected in a spark chamber, where the distinctive topological signature of outgoing muons was differentiated from that of electrons, and they were able to claim the existence of the *muon neutrino* [11].

Once again, the neutrino family was enlarged in 2001. After the discovery of the tau lepton [12] they began to search for the third neutrino associated with the tau and they found it after 25 years from the discovery of the tau lepton, by the DONUT experiment at Fermilab [13]. The first indication of this third neutrino came from the observation of missing energy and momentum in tau decays, similar to the beta decay that led to the discovery of the electron neutrino.

The tau neutrino is the second most recent discovered particle of the Standard Model (the most recent is the Higgs boson in 2012) and its existence had already been deduced by both theoretical consistency and experimental data from LEP [14]. In fact, in 1989 the ALEPH detector measured the Z-boson decay width, and assuming the invisible width is just the decay width of the process $Z \to \nu \overline{\nu}$, the number of neutrinos interacting weakly was found to be

$$N_{\nu} = 2.984 \pm 0.008 \tag{1.3}$$

This is a restriction on the number of *active neutrinos* — weakly-interacting neutrinos — which resulted to be 3 [15]. There could exist additional neutrinos as long as they do not participate in SM interactions, and these are often called *sterile neutrinos*.

1.1.1 Neutrino interactions

In the theoretical framework of the Standard Model (SM), that so far is the best theory we have to describe elementary particles and their interactions [16], neutrinos are massless fermions that neither interact electromagnetically, as they do not carry electric charge, nor interact strongly, as they do not carry color charge as well; hence, they interact exclusively weakly. Moreover, SM neutrinos only exist with left chirality and SM antineutrinos only exist with right chirality: this is in accordance with the SM assumption that neutrinos are massless and with the experimental evidence that neutrinos have left-handed helicity and antineutrinos have right-handed helicity [17], since for massless particles chirality is identical to helicity.

According to SM, there are two kinds of weak interaction [18]: the charged-current interaction (CC), with the weakly-interacting fermions which form a current with a non-zero electric charge – and is thus mediated by the charged W^{\pm} boson – and the neutral-current interaction (NC), with the weakly-interacting fermions which form a current with a zero electric charge – and is thus mediated by the neutral Z boson. SM describes three flavors of neutrinos (ν_e, ν_μ, ν_τ) that are named after the charged lepton they couple to in CC interactions: for each neutrino, there exists the corresponding antineutrino which has opposite lepton number and opposite helicity.

When neutrinos interact through either the charged or neutral weak currents, they may scatter off the target nucleons through different kinds of processes. The most relevant of these neutrino scattering processes in the SBN energy regime - around 1 GeV - are the following [19]:

• the NC elastic scattering, where a neutrino (antineutrino) scatters off the nucleon it comes into contact with, and the initial products of the reaction remain intact

$$\nu_{\ell}(\overline{\nu_{\ell}}) + N \to \nu_{\ell}(\overline{\nu_{\ell}}) + N \tag{1.4}$$

• the CC quasi-elastic scattering, where a neutrino (antineutrino) scatters off a nucleon to produce the corresponding charged lepton (antilepton) and the other nucleon

$$\nu_{\ell}(\overline{\nu_{\ell}}) + N \to \ell^{-}(\ell^{+}) + N' \tag{1.5}$$

• the multi-nucleon emission, a process conceptually similar to CC quasi-elastic scattering but the neutrino interacts with one or more nucleons inside the nucleus, such as

$$\nu_{\ell} + (n+p) \to \ell^{-} + (p+p)$$
 (1.6)

This is possible because of the existence of short-range interactions in heavy nuclei.

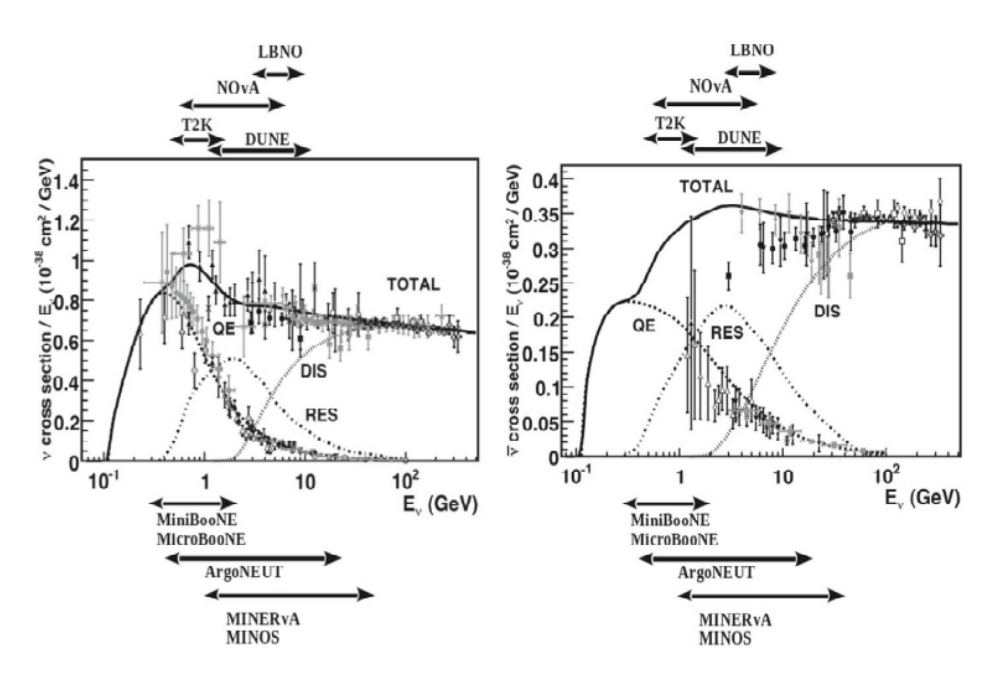


Figure 1.1: CC total cross section per nucleon per unit energy of the incoming particles vs neutrino on the left, and antineutrino on the right, energy for quasi-elastic scattering (QE), resonant interactions (RES) and deep inelastic scattering (DIS). The solid line represents the sum of all the cross sections. Taken from [21].

• pion production processes, which can be distinguished into *resonant processes* where the neutrino-nucleon scattering produces a resonance which quickly decays into a nucleon and another particle (usually a charged pion), such as

$$\nu_{\ell} + p \stackrel{\Delta^{++}}{\to} \ell^{-} + \pi^{+} + p \tag{1.7}$$

and *coherent processes* where the transferred momentum is low and the neutrino interacts with the entire nucleus, rather than the nucleons within it. Coherent scattering is not only responsible for the production of pions but also of many other particles such as photons.

• the *deep inelastic scattering*, dominant for high energies, where the neutrino has enough energy to interact with an individual quark which forms the nucleon it comes into contact with, emitting a shower of hadrons in a process called hadronization, such as

$$\nu_{\ell}(\overline{\nu_{\ell}}) + N \to \nu_{\ell}(\overline{\nu_{\ell}}) + X \tag{1.8}$$

$$\nu_{\ell}(\overline{\nu_{\ell}}) + N \to \ell^{-}(\ell^{+}) + Y \tag{1.9}$$

with N the hadronized nucleon and X, Y the CC, NC induced hadron showers respectively.

More information on neutrino interactions with matter can be found in [20].

Moveover, in figure 1.1 there is a global and complete overview of CC neutrino-nucleon cross section, from which it is evident that for low energies QE process is dominant, while for high energies DIS process is the dominant one. Multi-nucleon emission has large theoretical uncertainties and is not shown.

1.1.2 Neutrino oscillations

As indicated in the previous section, according to the Standard Model neutrinos are massless particles with only left chirality. The phenomenon of *neutrino oscillations*, which implies that neutrinos have non-zero masses and therefore may have also right chirality, is thus BSM physics and will require at some point a modification to the SM theory [22].

The concept of neutrino masses and oscillations was initially proposed by B. Pontecorvo in 1957 [23], thinking of an analogy between leptons and hadrons, and suggesting that neutrinos could oscillate similarly to the $K_0 - \overline{K_0}$ system. At that time, only one type of neutrino was known, and oscillation was thought to be only between neutrinos and antineutrinos. Subsequently, with the discovery of the muon neutrino, Pontecorvo naturally extended his idea to encompass two neutrinos [24]. The first phenomenological theory of two-neutrino mixing was soon proposed by V. Gribov and B. Pontecorvo in 1969 [25]. A full phenomenological theory of neutrino mixing and oscillation would have been developed later, but it is important to observe that Pontecorvo already anticipated solar neutrinos could oscillate even before the first experimental results.

Solar neutrino problem

The first hint of neutrino oscillation came from the Homestake experiment. In 1968, R. Davis and J. N. Bahcall carried out a radio-chemical experiment to count solar neutrinos and verify the Standard Solar Model (SSM). Theoretical calculations were conducted by Bahcall, while Davis managed the experimental part. Bahcall determined the expected rate at which the detector should capture neutrinos; however, Davis's experiment yielded only one third of this expected figure [26]. This significant discrepancy in results gave rise to the *solar neutrino problem*.

Homestake experiment detected solar neutrinos through the capture reaction on a C₂Cl₄ target

$$\nu_e + {}^{37}\text{Cl} \to e^- + {}^{37}\text{Ar}$$
 (1.10)

and the events seen by the experiment were only about a third of the predicted number by the SSM. Other radio-chemical experiments, such as GALLEX [27] and SAGE [28], together with the water Cherenkov Kamiokande experiment [29], confirmed the solar neutrino problem. Neutrino oscillation was not identified as the source of the deficit until the SNO experiment provided clear evidence of neutrino flavor change in 2001 [30], since it was sensible to

$$\nu_e + d \to p + p + e^- \tag{1.11}$$

$$\nu_x + d \to p + n + \nu_x \tag{1.12}$$

$$\nu_x + e^- \to \nu_x + e^- \tag{1.13}$$

from which it was possible to measure the composition of the neutrino flux and provide a model independent test of neutrino flavour change.

Atmospheric neutrino anomaly

A similar problem was found in 1986 by the Irvine-Michigan-Brookhaven [31] and Kamiokande [32] experiments, which observed a deficit in the muon neutrino component expected from the atmospheric neutrino flux, giving rise to the so-called *atmospheric neutrino anomaly*.

Atmospheric neutrinos came from the interactions between cosmic rays and atmospheric nuclei, which entails the production of mesons such as pions that decay mainly into

$$\pi^{\pm} \to \mu^{\pm} + \nu_{\mu}(\overline{\nu_{\mu}}) \tag{1.14}$$

Moreover, many of these muon undergo secondary muon decays as

$$\mu^{\pm} \to e^{\pm} + \nu_e(\overline{\nu_e}) + \overline{\nu_{\mu}}(\nu_{\mu}) \tag{1.15}$$

These neutrinos are called *atmospheric neutrinos* and a rough estimation is that there are two times more muon neutrinos than electron neutrinos, but the observed rate of muon neutrinos was lower than the expected rate. This anomaly has been resolved by the SuperKamiokande experiment that started in 1996. After two years of data taking, SuperKamiokande announced in 1998 the clear observation of a deficit of muon neutrinos, consistent with the hypothesis of neutrino oscillation [33].

Neutrino mixing

In the actual paradigm, neutrinos can be described through the flavour eigenstates which are the well known ν_e, ν_μ, ν_τ accounting respectively for electron, muon and tau neutrino; they can be described as well through the mass eigenstates which are denoted by ν_1, ν_2, ν_3 . If neutrinos were massless, there would be no neutrino oscillations and these two basis would be identical, which means that flavour eigenstates – those undergoing weak interactions and experimentally detectable – are at the same time mass eigenstates – those subject to time evolution [34].

If neutrinos have non-zero mass, these two basis are related by a unitary transformation different from the identity, and flavour eigenstates can be written as a superposition of mass eigenstates and viceversa: calling ν_{α} the flavour eigenstates and ν_{i} the mass eigenstates,

$$|\nu_{\alpha}\rangle = \sum_{i=1,2,3} U_{\alpha i}^* |\nu_i\rangle \tag{1.16}$$

$$|\nu_i\rangle = \sum_{\alpha=e,\mu,\tau} U_{\alpha i} |\nu_{\alpha}\rangle \tag{1.17}$$

where U is known as Pontecorvo-Maki-Nakagawa-Sakata or PMNS matrix [35]. As well as CKM matrix describes the quark mixing, PMNS matrix describes the neutrino mixing.

In the assumption that neutrinos are Dirac particles, U_{PMNS} can be expressed in terms of three

mixing angles θ_{12} , θ_{13} and θ_{23} and one Dirac CP-violating phase δ according to

$$U_{\text{PMNS}} = R_{23}(\theta_{23})\Gamma(\delta)R_{13}(\theta_{13})\Gamma^{\dagger}(\delta)R_{12}(\theta_{12})$$
(1.18)

where R_{ij} represents an Euler rotation by θ_{ij} in the ij-plane and $\Gamma = \text{diag}(1, 1, e^{i\delta})$; explicitly

$$U_{\text{PMNS}} = \begin{pmatrix} 1 & 0 & 0 \\ 0 & c_{23} & s_{23} \\ 0 & -s_{23} & c_{23} \end{pmatrix} \begin{pmatrix} 1 & 0 & 0 \\ 0 & 1 & 0 \\ 0 & 0 & e^{i\delta} \end{pmatrix} \begin{pmatrix} c_{13} & 0 & s_{13} \\ 0 & 1 & 0 \\ -s_{13} & 0 & c_{13} \end{pmatrix} \begin{pmatrix} 1 & 0 & 0 \\ 0 & 1 & 0 \\ 0 & 0 & e^{-i\delta} \end{pmatrix} \begin{pmatrix} c_{12} & s_{12} & 0 \\ -s_{12} & c_{13} & 0 \\ 0 & 0 & 1 \end{pmatrix}$$
(1.19)

with $s_{ij} = \sin \theta_{ij}$ and $c_{ij} = \cos \theta_{ij}$. The range of these mixing parameters is determined by

$$\theta_{12}, \theta_{13}, \theta_{23} \in \left[0, \frac{\pi}{2}\right]$$
 $\delta \in [0, 2\pi]$ (1.20)

If neutrinos were Majorana particles, i.e. if neutrinos were their own antiparticles ($\nu = \overline{\nu}$) then the most general form of U_{PMNS} matrix contains two additional phases ϕ_1, ϕ_2 and is obtained by $U \to U \cdot U_{\text{M}}$ with $U_{\text{M}} = \text{diag}(1, e^{i\phi_1}, e^{i\phi_2})$; in any case, these Majorana phases have no observable effects in neutrino oscillations [36].

Propagation and interference

In the vacuum, since $|\nu_k\rangle$ are mass eigenstates, their time evolution is subject to Schroedinger equation and can be defined by a plane wave solution of the form

$$|\nu_k(t)\rangle = e^{-iE_k t} |\nu_k(0)\rangle \tag{1.21}$$

with $|\nu_k(0)\rangle = |\nu_k\rangle$ and $t \neq 0$. Substituting this result into (1.16) the propagation of a flavour eigenstate $|\nu_{\alpha}\rangle$ at a generic time t can be written in the form

$$|\nu_{\alpha}(t)\rangle = \sum_{k} U_{\alpha k}^{*} e^{-iE_{k}t} |\nu_{k}\rangle = \sum_{\gamma} \left(\sum_{k} U_{\alpha k}^{*} e^{-iE_{k}t} U_{\gamma k} \right) |\nu_{\gamma}\rangle$$
 (1.22)

This implies that, if the neutrino was produced at time t = 0 in a pure flavour eigenstate $|\nu_{\alpha}\rangle$, the probability of measuring the neutrino in a flavour eigenstate $|\nu_{\beta}\rangle \neq |\nu_{\alpha}\rangle$ at a time t is

$$P_{\alpha \to \beta}(t) = |\langle \nu_{\beta} | \nu_{\alpha}(t) \rangle|^2 = \sum_{k,j} U_{\alpha k}^* U_{\beta k} U_{\alpha j} U_{\beta j}^* e^{-i(E_k - E_j)t}$$

$$\tag{1.23}$$

Using the ultrarelativistic approximation $|\vec{\mathbf{p}_k}| = p_k \gg m$, which applies to all currently observed neutrinos since their masses are less than 1 eV and their energies are at least 1 MeV,

$$E_k = \sqrt{p_k^2 + m_k^2} \simeq p_k + \frac{m_k^2}{2p_k} \simeq E + \frac{m_k^2}{2E}$$
 (1.24)

and using also $t \simeq L$ where L is the distance travelled by the neutrino, equation (1.23) becomes

$$P_{\alpha \to \beta}(L) = \delta_{\alpha\beta} - 4\sum_{k>j} \operatorname{Re}(u)\sin^2\left(\frac{\Delta m_{kj}^2 L}{4E}\right) \pm 2\sum_{k>j} \operatorname{Im}(u)\sin\left(\frac{\Delta m_{kj}^2 L}{2E}\right)$$
(1.25)

with $u = U_{\alpha k}^* U_{\beta k} U_{\alpha j} U_{\beta j}^*$ and $\Delta m_{kj}^2 = m_k^2 - m_j^2$. In equation (1.25) the first term represents the no-oscillation case, the second term corresponds to the three-flavour oscillation with amplitude given by Re(u) and phase depending on the mass splitting and on the L/E ratio – the latter typically fixed by the experimental conditions – while the third term accounts for CP violation and its sign depends on whether neutrinos (+) or antineutrinos (-) are oscillating [37]. The oscillation probability of $\alpha \neq \beta$ channels indicates the transition probability, while for $\alpha = \beta$ channels it indicates the survival probability.

The neutrino oscillation framework so far presented is valid in vacuum, where all flavour eigenstates interact equally; the presence of matter changes the game [38]. The MSW effect, or matter effect, involves CC and NC coherent neutrino scatterings off electrons or nucleons in a medium: if NC scattering equally impacts the three neutrino flavours, CC scattering only impacts only electron neutrinos and this leads to a modification of oscillation probabilities [39] which has a huge importance in experiments at long baselines.

Two-neutrino case

It is worth considering the two-flavour neutrino mixing matrix

$$U = \begin{pmatrix} \cos \theta & \sin \theta \\ -\sin \theta & \cos \theta \end{pmatrix} \tag{1.26}$$

In this scenario, the only parameter is the real mixing angle θ and there are no complex phases to eventually quantify the CP violation. However, it is still useful to consider this model since in many cases the oscillation phenomenology can be well approximated by the two-flavour model. If the neutrino at time t=0 is in a flavour eigenstate $|\nu_{\alpha}\rangle$ the probability to find the neutrino in the flavour eigenstate $|\nu_{\beta}\rangle \neq |\nu_{\alpha}\rangle$ after a distance L is

$$P_{\alpha \to \beta}(t) = |\langle \nu_{\beta} | \nu_{\alpha}(t) \rangle|^2 = \sin^2(2\theta_{ij}) \sin^2\left(\frac{\Delta m_{ij}^2 L}{4E}\right)$$
 (1.27)

This equation describes an oscillating function of L, where $\sin^2(2\theta_{ij})$ describes the oscillation amplitude where the oscillation length depends on the mass splitting Δm_{ij}^2 and is given by

$$\lambda_{ij} = \frac{4\pi E}{\left|\Delta m_{ij}^2\right|} \tag{1.28}$$

Note that this oscillation probability is unchanged for $\Delta m_{ij}^2 \to -\Delta m_{ij}^2$ and for $\theta_{ij} \to \pi/2 - \theta_{ij}$

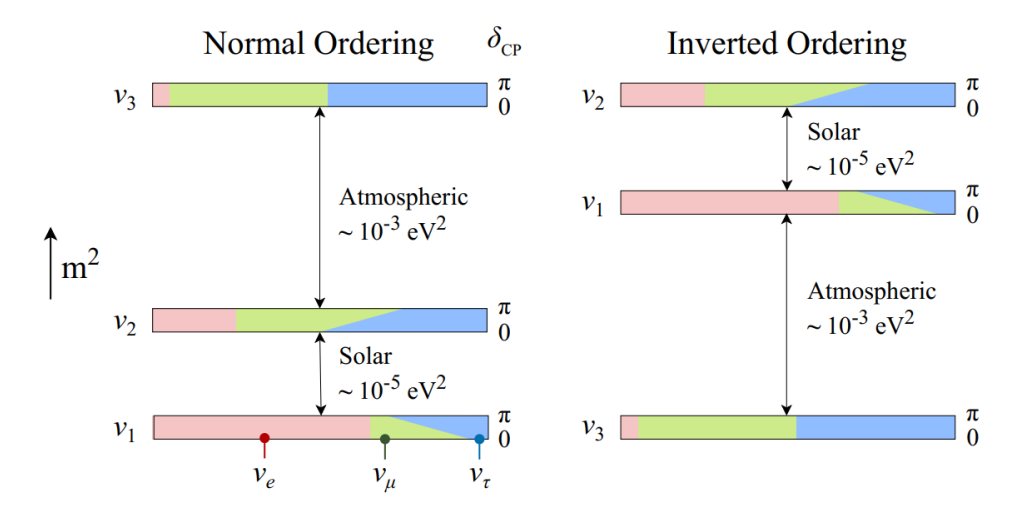


Figure 1.2: On the left, graphical representation of NMO; on the right, graphical representation of IMO. The atmospheric mass splitting is roughly two order of magnitude greater than the solar mass splitting. The contribution of the three flavour eigenstates ν_e, ν_μ, ν_τ to each mass eigenstates ν_1, ν_2, ν_3 is highlighted for two possible values of δ . Note that, because of an horizontal reflection symmetry, showing δ from 0 to π is enough even if δ ranges from 0 to 2π . Taken from [41].

showing that two-neutrino oscillations in vacuum do not probe the hierarchy of the masses m_i and m_j [34]. For energies $E \gg \Delta m_{ij}^2 L$ the oscillation frequency is too low – and the oscillation length is therefore too high – and there is no observable effect; the same occurs for energies $E \ll \Delta m_{ij}^2 L$ since the oscillation frequency is too high – and the oscillation length is therefore too low – and the observable flux averages at $\frac{1}{2}\sin^2{(2\theta)}$. An experiment will thus be sensitive only to energies $E \sim \Delta m_{ij}^2 L$, which implies a mass splitting of

$$\Delta m^2 \sim \frac{E}{L} \tag{1.29}$$

This means that, in order to maximize the sensitivity to neutrino oscillations, it is important to choose both an appropriate neutrino energy E and an appropriate baseline L.

Neutrino mass ordering

It is evident from equation (1.25) that oscillation experiments are not sensitive directly to the absolute values of neutrino masses but only to their squared mass differences. From the unitarity condition required by the $U_{\rm PMNS}$ matrix it follows that

$$\Delta m_{12}^2 + \Delta m_{23}^2 + \Delta m_{31}^2 = 0 ag{1.30}$$

so only two of the three mass splittings are independent. The mass splitting $\Delta m_{21}^2 = m_2^2 - m_1^2$ is called solar mass splitting and is known to be $\Delta m_{21}^2 \sim 10^{-5} \,\mathrm{eV}^2 > 0$ thanks to matter effects [40]. The mass splitting $|\Delta m_{32}^2| \sim |\Delta m_{31}^2| \sim 10^{-3} \,\mathrm{eV}^2$ is called atmospheric mass splitting and its sign is currently unknown, since it is measured only via neutrino oscillations in vacuum [33], and this leads to two possibilities for the neutrino mass hierarchy, pictured in Figure 1.2:

- 1. the third mass eigenstate has the largest mass, i.e. $m_1 < m_2 < m_3$, therefore $\Delta m_{31}^2 > 0$ and this is known as Normal Mass Ordering (NMO) or Normal Hierarchy;
- 2. the third mass eigenstate has the smallest mass, i.e. $m_3 < m_1 < m_2$, therefore $\Delta m_{31}^2 < 0$ and this is known as Inverted Mass Ordering (IMO) or Inverted Hierarchy;

1.2 Oscillation experiments

The formulation of the most general Lagrangian of the Standard Model for massless neutrinos involves 19 parameters, whose numerical values are established by experiments [42]. Expansions of the Standard Model with massive neutrinos, in the hypothesis of Dirac neutrinos, require 7 additional parameters $m_1, m_2, m_3, \theta_{12}, \theta_{13}, \theta_{23}, \delta$, and the numerical values of these parameters might be eventually found through oscillation experiments.

Oscillation experiments can be classified into appearance experiments which test the transition probability and detect the appearance of some neutrino flavour different from those produced in the source, and disappearance experiments which test the survival probability and measure the flux decrease of those neutrino flavours produced in the source. The parameters determined by the oscillation experiments are the three mixing angles, the two mass splittings and the CP violating phase: from 1998 the precision of these parameters has significantly improved, so that we are currently in the so-called "precision era" of neutrino physics [41]. Note that such kind of experiments are not capable to measure the absolute masses m_1, m_2, m_3 .

Solar neutrino experiments

As explained in section 1.1.2, solar neutrinos have caused many challenges for particle physicists, but at the same time they have enabled the discovery of neutrino oscillations. Solar neutrinos are produced mainly in the pp chains and the CNO cycle reactions and have MeV-scale energies. Several solar neutrino experiments have been performed and continue to run, in order to detect neutrinos from the Sun: the dominant parameters θ_{12} and Δm_{12}^2 have been determined to be

$$\sin^2 \theta_{12} = 0.307^{+0.013}_{-0.012}$$
 $\Delta m_{21}^2 = (7.53 \pm 0.18) \times 10^{-5} \,\text{eV}^2$ (1.31)

These values were taken from [37] and have been constrained by Gallium experiments such as GALLEX [27] and SAGE [28], by Cherenkov experiments such as SuperKamiokande [43], SNO [30] and Borexino [44], and by KamLAND [45].

Atmospheric neutrino experiments

As explained in section 1.1.2, atmospheric neutrinos are produced in the interactions between cosmic rays and atmosphere nuclei with energies in a GeV-TeV range. In this case the dominant

parameters are θ_{23} and Δm_{23}^2 which have been determined to be

$$\sin^2 \theta_{23} = 0.547^{+0.024}_{-0.018}$$
 $\Delta m_{32}^2 = (2.437 \pm 0.033) \times 10^{-3} \,\text{eV}^2$ (1.32)

$$\sin^2 \theta_{23} = 0.534^{+0.024}_{-0.021}$$
 $\Delta m_{32}^2 = -(2.519 \pm 0.033) \times 10^{-3} \,\text{eV}^2$ (1.33)

These values refer to the NMO and IMO case, respectively, were taken from [37] and have been provided mainly by SuperK [43] and by IceCube [46].

Reactor experiments

Nuclear reactors can emit $\overline{\nu_e}$ from beta decays of unstable elements such as ²³⁸U and ²³⁹Pu, with energies peaking at around 3 MeV and extending up to 8 MeV. They are the major sources of human-produced neutrinos and have helped to solve the solar neutrino problem.

 $\overline{\nu_e}$ disappearance channel is the only available one to study neutrino oscillations with nuclear reactors, and the inverse beta decay (IBD) $\overline{\nu_e} + p \rightarrow e^+ + n$ provides a way to detect electron antineutrinos in the relevant energy range. Reactor experiments at medium baseline of $\sim 50 \, \mathrm{km}$ are sensitive to θ_{13} mixing angle, which remained unmeasured for a long time. The first reactor experiments, in fact, has been conducted at short baseline such as CHOOZ in France with a $\sim 1 \, \mathrm{km}$ baseline [47], or at long baseline such as KamLAND in Japan with a $\sim 180 \, \mathrm{km}$ baseline [45] and were only used to constraint the solar and atmospheric parameters.

The first accurate measure of θ_{13} mixing angle come from medium-baseline experiments such as Double CHOOZ in France [48], Daya Bay in China [49] and RENO in Korea [50] which led to

$$\sin^2 \theta_{13} = (2.20 \pm 0.07) \times 10^{-2} \tag{1.34}$$

This value is taken from [37], from which θ_{13} appears to be smaller than the other two mixing angles, as opposed to the case of CKM matrix in which all three angles are small.

Accelerator experiments

In accelerators, intense proton beams colliding with a fixed target produce mesons, which are then selected and focused, and finally decay into neutrinos. Such neutrinos have energies from $\sim 100\,\mathrm{MeV}$ to $\sim 100\,\mathrm{GeV}$: combining it with the advantage of being able to select the baseline L, it is possible to have some control over the E/L ratio and thus over the observable oscillation parameters. Accelerator experiments operate both in the appearance and in the disappearance channels with two detectors: the near detector studies the unoscillated flux of neutrinos while the far detector observes the oscillated spectrum of neutrinos — the adjectives "near" and "far" refer to the distance from the neutrino source. Both detectors typically use the same technology and target nucleus, to minimize the systematic uncertainties.

The first generation of long baseline experiments includes K2K which used a ν_{μ} neutrino beam

from KEK and MINOS which used the ν_{μ} neutrino beam from Fermilab, and mainly aimed to confirm the existence of neutrino oscillations. In Europe the experiment OPERA was able to confirm the $\nu_{\mu} \to \nu_{\tau}$ oscillation appearance with 6.1 σ significance, with the ν_{μ} neutrino beam from SPS at CERN [51]. The second generation of long baseline experiments was designed to observe $\nu_{\mu} \to \nu_{e}$ oscillation with precise measurements of the unknown oscillation parameters θ_{23} , θ_{13} and the CP-violating phase δ , and the mass ordering: the experiments were T2K as the successor of K2K [52] and NO ν A as the successor of MINOS [53] and reported a slight preference for NMO. The third generation of long baseline experiments is currently under preparation and includes HyperK in Japan and DUNE in the US.

1.2.1 Experimental anomalies

Despite the well-established three-flavor neutrino mixing framework, described in section 1.1.2, numerous experimental anomalies have been observed so far. For example, discrepancies in the observed and expected electron neutrino fluxes from Gallium based experiments gave rise to the Gallium anomaly; a deficit in the observed flux of antineutrinos emitted from nuclear reactors, compared to theoretical predictions, is related to several nuclear reactors anomalies; an excess of $\overline{\nu_e}$ in a $\overline{\nu_\mu}$ beam has produced the LSND anomaly, and similarly an excess of ν_e in a ν_μ beam has led to the MiniBooNE anomaly. The detailed description of all these anomalies follow.

Gallium anomaly

The Gallium Experiment (GALLEX) in Italy [27] and the Soviet-American Gallium Experiment (SAGE) in Russia [28] were designed to detect neutrinos and measure their flux via the reaction

$$\nu_e + {}^{71}\text{Ga} \to e^- + {}^{71}\text{Ge}$$
 (1.35)

The observed flux of ν_e detected by these experiments was found to be significantly lower than what was expected by knowing the radioactive sources activity. This deficit was studied more accurately by the Baksan Experiment on Sterile Transitions (BEST) [54], which reported a larger deficit and confirmed this *Gallium anomaly*. The ratios between observed and predicted rates as a function of the average path length of neutrinos are reported in Figure 1.3 and can be fitted with an average ratio of $R = 0.80 \pm 0.04$ [55].

Reactor anomalies

Nuclear reactor experiments, particularly at short distances from the reactor core, had observed a deficit in the observed flux of electron antineutrinos: more specifically, the measured rate of $\overline{\nu_e}$ was slightly lower than expected, with the measured/expected ratio of $R=0.976\pm0.024$ [56]. By combining this result with other reactor experiments at longer baseline, such as Chooz and

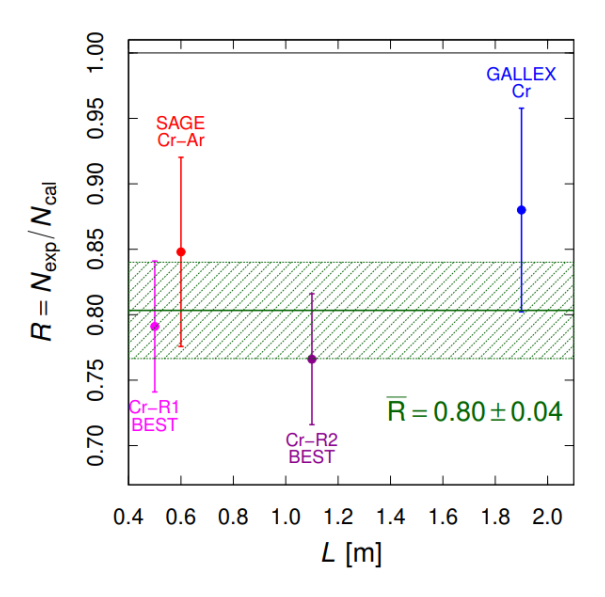


Figure 1.3: Ratios between observed and predicted ν_e flux at the GALLEX, SAGE, BEST experiments. Taken from [55].

KamLAND, it results in a larger average deficit of 5.7% at $R = 0.943 \pm 0.023$ [56]. This is known as Reactor Antineutrino Anomaly (RAA) and its origin is still unknown, since several models have been proposed to better define the reactor antineutrino fluxes. If RAA is due to neutrino mixing, then it could be explained by an energy-independent suppression of $\overline{\nu_e}$ flux at short distances, which requires $|\Delta m^2| \gtrsim 1 \, \text{eV}^2$: since this is much larger than solar and atmospheric mass splittings, it may suggest the existence of a fourth (sterile) neutrino. Such hints have then motivated reactor experiments at a very short baseline from the core.

Neutrino-4 is one of these experiments designed to search for RAA anomaly. The experimental setup consists in a Gd-doped liquid scintillator detector, sensitive to IBD reaction of electron antineutrinos on protons, and was built to measure the flux and the spectrum of reactor $\overline{\nu_e}$ as a function of the distance from the reactor core, being able to sample baseline of $L \sim 6-12\,\mathrm{m}$. The results of this experiment agree with the hypothesis of a fourth neutrino and with other experimental results such as GALLEX, SAGE and BEST but at the same time are strongly rejected by other experiments, such as PROSPECT or STEREO [57].

LSND anomaly

The LSND (Liquid Scintillator Neutrino Detector) anomaly refers to an unexpected excess of electron antineutrino events observed in neutrino oscillation experiments conducted at the Los Alamos National Laboratory from 1993 to 1998: in particular, in an almost pure $\overline{\nu_{\mu}}$ beam and at a baseline of $\sim 30 \,\mathrm{m}$, it was found an anomalous excess of $\overline{\nu_{e}}$ [58].

A 800 MeV proton beam was used to produce pions: most of π^- 's stopped in the target while π^+ 's and their daughters μ^+ 's decayed and produced ν_{μ} , $\overline{\nu_{\mu}}$, ν_{e} with a little contamination of $\overline{\nu_{e}}$. Electron antineutrinos are identified through the IBD reaction with protons, which produced positron and a delay photon from neutron capture: this signal might be mimicked by accidental

coincidence between a positron-like and a neutron-like signal, or by π^- 's and μ^- 's decays in the source. However, an excess of $87.9\pm22.4\pm6.0\,\overline{\nu_e}$ events over the expected background was found and this can be hardly interpreted as due to other particles than $\overline{\nu_e}$ [59].

If this excess is interpreted as a $\overline{\nu_{\mu}} \to \overline{\nu_{e}}$ oscillation, given the short-baseline approximation $\Delta m_{21}^2 \sim \Delta m_{31}^2 = 0$, the best-fit oscillation point is given by

$$\sin^2(2\theta) \sim 0.003$$
 $\Delta m^2 \sim 1.2 \,\text{eV}^2$ (1.36)

which means this experiment implies three independent mass splittings, and therefore a fourth neutrino; moreover, it implies at least one neutrino has a mass greater than 0.4 eV [59].

MiniBooNE anomaly

The MiniBooNE experiment at Fermilab was designed to test of the LSND results. It consisted in a Cherenkov detector exposed to the Booster Neutrino Beam, able to provide a 99.5% pure ν_{μ} beam with an average energy of $\sim 600\,\mathrm{MeV}$ and a baseline of 541 m, in order to provide a similar L/E ratio with respect to LSND and thus to be sensitive to the same oscillation parameters. This experiment could detect different final states through the analysis of the Cherenkov light-ring shapes, produced by the different charged particles such as electron, muons and pions.

The final results of MiniBooNE showed an excess of data over background prediction in both neutrino and antineutrino data sets, concentrated in the low energy region $E_{\nu} \in (200, 475) \text{MeV}$ and for this reason called *Low Energy Excess*, corresponding to 560.6 ± 119.6 and 77.4 ± 28.5 excess events in neutrino and antineutrino modes respectively [60].

In this case, the final best-fit parameters for the full data sets were found to be

$$\sin^2(2\theta) \sim 0.807$$
 $\Delta m^2 \sim 0.043 \,\text{eV}^2$ (1.37)

Several checks were conducted on the MiniBooNE data to ensure accurate background estimation, yet no significant contribution was identified that could account for the excess of events.

In 2013, results from the ICARUS experiment regarding the search for a $\nu_{\mu} \rightarrow \nu_{e}$ signal due to the LSND anomaly with CNGS neutrino beam were disclosed. ICARUS results substantially constrained the allowed options for the LSND anomaly to a narrow parameter space around

$$\sin^2(2\theta) \sim 0.005$$
 $\Delta m^2 \sim 0.5 \,\text{eV}^2$ (1.38)

showing an overall agreement with the LSND and MiniBooNE results [60]. This result strongly limits the MiniBooNE anomaly, suggesting an instrumental or otherwise unexplained nature of the low energy signal. The MicroBooNE experiment addressed the MiniBooNE anomaly with the same beam and baseline, but using the same LArTPC technology of ICARUS: the results refused the hypothesis that ν_e CC interactions are fully responsible for MiniBooNE anomaly [61].

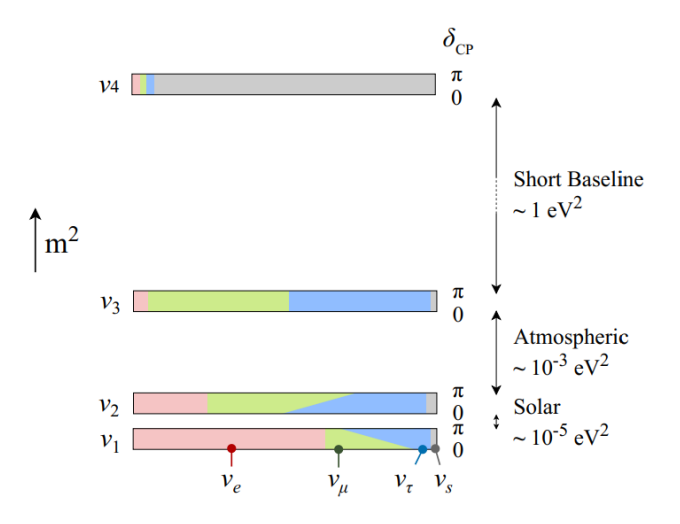


Figure 1.4: Representation of the neutrino mass splittings and flavour mixing, for the 3+1 model, in the assumption of NMO i.e. $\nu_1 < \nu_2 < \nu_3 < \nu_4$. Taken from [41].

1.3 Sterile neutrino models

The experimental anomalies reported at Gallium-based experiments, at nuclear reactors and at accelerators could be thought as short-baseline oscillations due to an additional neutrino mass state ν_4 with a mass splittings $\Delta m_{41}^2 \sim 1 \,\mathrm{eV}^2$ that cannot be detected by experiments at longer baselines. As already explained in section 1.1, there are only 3 active neutrinos and thus any additional state may exist only as a sterile neutrino: note that such state would not be directly detectable, but only through the oscillations it induces on the three active states.

In a 3+N model, with 3 the number of active neutrinos and N the number of sterile neutrinos, the PMNS matrix from Equation (1.19) can be extended to a $(3+N) \times (3+N)$ matrix. The simplest of these models is the 3+1 model which involves only 1 sterile neutrino ν_s and a fourth mass state ν_4 : assuming the existence of this sterile neutrino, the ν_s contribution to the other mass states has to be small as well as ν_e, ν_μ, ν_τ contributions to the ν_4 mass state. This is well depicted in a schematic way in figure 1.4.

The assumption of $|\Delta m_{41}^2| \gg |\Delta m_{31}^2|$, Δm_{21}^2 is well supported from experimental results: in the limit where the atmospheric and solar mass splittings are negligible, short-baseline oscillations can be approximated by the two-flavour mixing case, for example [62]

$$P(\nu_e \to \nu_e) \simeq 1 - 4|U_{e4}|^2 \left(1 - |U_{e4}|^2\right) \sin^2\left(\frac{\Delta m_{41}^2 L}{4E}\right) = 1 - \sin^2\left(2\theta_{ee}\right) \sin^2\left(\frac{\Delta m_{41}^2 L}{4E}\right) \quad (1.39)$$

$$P(\nu_{\mu} \to \nu_{\mu}) \simeq 1 - 4|U_{\mu 4}|^{2} \left(1 - |U_{\mu 4}|^{2}\right) \sin^{2}\left(\frac{\Delta m_{41}^{2} L}{4E}\right) = 1 - \sin^{2}(2\theta_{\mu\mu}) \sin^{2}\left(\frac{\Delta m_{41}^{2} L}{4E}\right)$$
(1.40)

$$P(\nu_e \to \nu_\mu) \simeq 4|U_{e4}|^2|U_{\mu 4}|^2 \sin^2\left(\frac{\Delta m_{41}^2 L}{4E}\right) = \sin^2(2\theta_{\mu e}) \sin^2\left(\frac{\Delta m_{41}^2 L}{4E}\right)$$
(1.41)

are the oscillation probabilities respectively for ν_e disappearance, for ν_{μ} disappearance and for ν_{μ} appearance (in a ν_e flux) with effective mixing angles defined in the above formulas. Note

that no explicit assumption about $U_{\tau 4}$ or U_{s4} are made – by unitary conditions it is known that

$$|U_{e4}| + |U_{u4}| + |U_{\tau 4}| + |U_{s4}| = 1 (1.42)$$

The focus is on these three oscillation probabilities since these are the transition channels which have been studied more extensively and where the short-baseline anomalies occur [62].

The 2 new CP-violating phases from the extended 4×4 mixing matrix do not lead to observable effects unless if both effects from Δm_{41}^2 and either Δm_{31}^2 or Δm_{21}^2 are simultaneously relevant. Most notably, the relationships among Equations (1.39), (1.40) and (1.41) imply that, if both U_{e4} and $U_{\mu4}$ are nonzero, then ν_e disappearance, ν_μ disappearance and ν_μ to ν_e appearance must all occur at the same L/E ratio [62].

1.3.1 Status and perspectives

Recently, several experiments have been proposed and conducted to tackle neutrino anomalies, revealing a complex picture with *contradictory results*. As of now, there is no definitive evidence either confirming or ruling out the existence of sterile neutrinos.

The LSND anomaly, which consists in an excess in the $\overline{\nu_e}$ appearance channel, can be interpreted in terms of short baseline $\nu_{\mu} \to \nu_{e}$ oscillations in the 3+1 model, with a mass splitting Δm_{41}^2 and an oscillation strength $\sin^2{(2\theta_{\mu e})}$ given by (1.36). Similarly, the MiniBooNE LEE anomaly can be interpreted in the 3+1 model with a mass splitting and an oscillation strength given by (1.37). Note that the best fit using the 3+1 model does not fully match the MiniBooNE data, and that the allowed regions of parameters from LSND and MiniBooNE are in overall agreement. On the other side, the KARMEN experiment found no evidence of oscillation in the $\overline{\nu_e}$ appearance channel, excluding therefore part of the allowed region in the $\left(\sin^2{(2\theta_{\mu e})}, \Delta m_{41}^2\right)$ plane [63]; the experiments ICARUS and OPERA provided strong limits on the allowed regions as defined in (1.38). A comparison of the best fit region is showed in Figure 1.5. In the same way, the Gallium anomaly discussed in section 1.2.1 can be interpreted in terms of short baseline neutrino oscillations in the ν_e disappearance channel. The results from Gallium based experiments give a mass splitting Δm_{41}^2 and an oscillation strength $\sin^2{(2\theta_{ee})}$ of

$$\sin^2(2\theta_{ee}) \sim 0.14$$
 $\Delta m_{41}^2 \gtrsim 0.6 \,\text{eV}^2$ (1.43)

However, these results are not in agreement with those from LSND and MiniBooNE. Again, tensions arise from reactor experiments: the Neutrino-4 experiment [64] hints at

$$\sin^2(2\theta_{ee}) \sim 0.36 \pm 0.12$$
 $\Delta m_{41}^2 \sim (7.30 \pm 0.13 \pm 1.16) \,\text{eV}^2$ (1.44)

which are not compatible with results from other reactor-based experiments. In fact, no evidence of oscillations was found in experiments such as Bugey [65], NEOS [66], PROSPECT [67] and

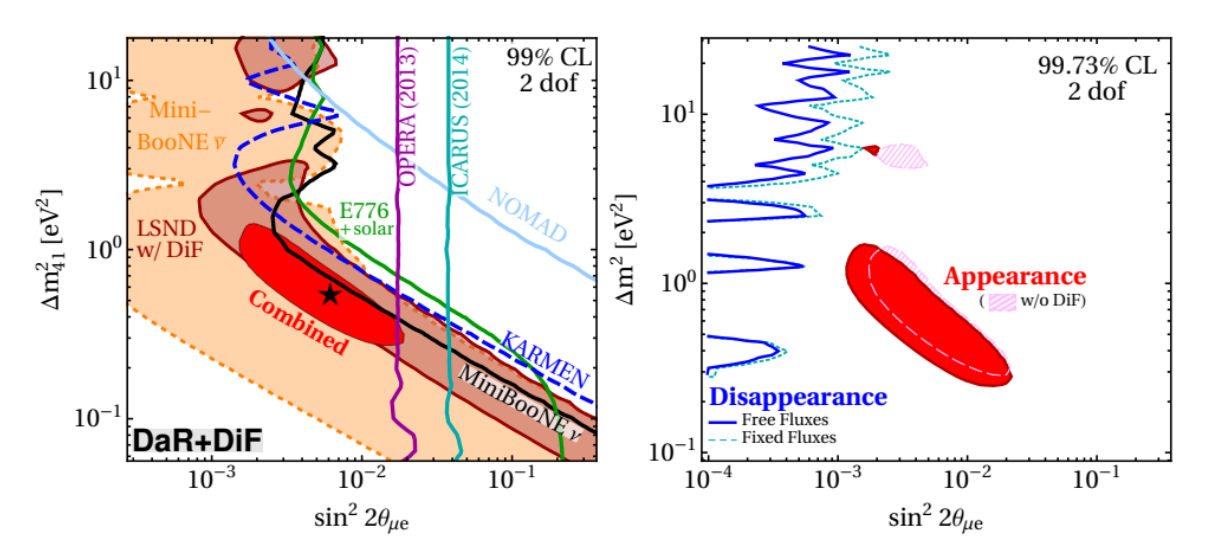


Figure 1.5: On the left, preferred regions by several $\nu_{\mu} \rightarrow \nu_{e}$ appearance experiments in the 3+1 scenario, at 99% CL for 2 degrees of freedom. On the right, preferred region of short-baseline appearance experiments (red region), compared to the region excluded by disappearance experiments (blue line) at 99.73% CL for 2 degrees of freedom. Taken from [62].

STEREO [68]. The search for short baseline oscillations in reactor-based experiments is also influenced by uncertainties related to reactor anti-neutrino fluxes, that may be reduced by using segmented detectors such as in Neutrino-4, PROSPECT and STEREO, or with ratios between detectors at different baselines such as in Bugey and NEOS.

Finally, overall, no signals of oscillation have been observed yet in ν_{μ} and $\overline{\nu_{\mu}}$ disappearance channels, addressed mainly by short baseline experiments using a ν_{μ} or $\overline{\nu_{\mu}}$ beam as the main one, such as in MiniBooNE and MINOS. Overall, the sterile neutrino framework appears controversial and future precision experiments such as the Short Baseline Neutrino program at Fermilab are expected to give a definitive answer to the sterile neutrino question, since it has access to both the ν_e appearance and ν_{μ} disappearance channels at the same time and it will be able to compare neutrino spectra at different baselines.

Chapter 2

ICARUS in the SBN program

ICARUS stands for "Imaging Cosmic And Rare Underground Signals" and dates back to 1977 when Carlo Rubbia first proposed a new type of neutrino detector [69]. This new detector started to be pre-assembled in 1997 in Pavia (Italy) where it was mounted and exposed to cosmic rays at the surface, aiming to test the detector's features and performance for the first time [70]. After the tests, the detector was moved to the underground Gran Sasso National Laboratories (LNGS) and it started operation in 2010 with the CNGS¹ beam and with cosmic rays.

The ICARUS collaboration carried out successfully a 3-year-long run, collecting from 2010 to 2013 around 3000 CNGS neutrino events as well as cosmic rays and atmospheric neutrinos. ICARUS proved the optimal detection capabilities of the liquid Argon TPC technology, and the strategies implemented for the Argon recirculation and purification systems have led to an outstanding achievement in terms of Argon purity, which is crucial for enabling physics studies with large-scale LArTPC detectors, paving the way for future similar experiments. In 2013, ICARUS conducted a search for an LSND-like anomalous signal using data from LNGS [71]: this search significantly constrained the parameter space allowed for the LSND and MiniBooNE anomalies, as cited in section 1.3.1.

Upon the conclusion of operations at LNGS, ICARUS was moved to CERN for an extensive overhaul, where it remained from 2015 to 2017. Following the overhaul, it was then shipped to FNAL and positioned at a shallow depth, to serve as the far detector in the SBN program [72].

2.1 Short Baseline Neutrino program

The Short Baseline Neutrino (SBN) program at Fermilab was devised primarily to investigate short-baseline neutrino oscillations [72], aiming to explore the hypothesis of light sterile neutrinos as an explanation for anomalies found in previous neutrino experiments, notably LSND, as explained in section 1.2.1. This program includes three LArTPC detectors strategically po-

¹CERN Neutrinos to Gran Sasso

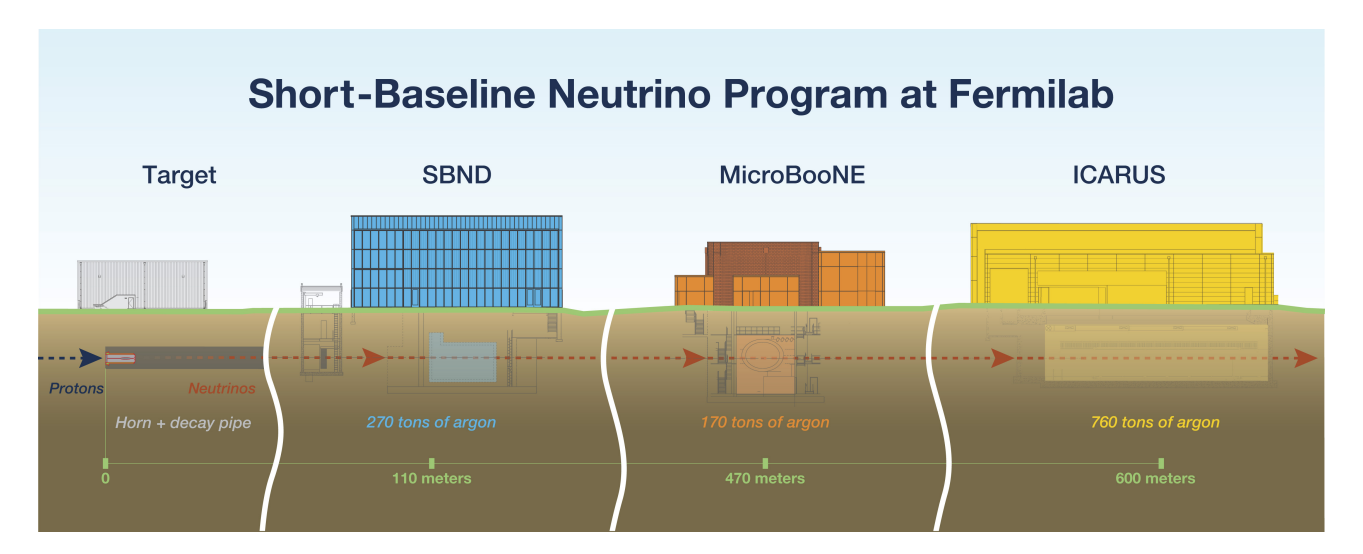


Figure 2.1: Fermilab's Short-Baseline Neutrino Program uses three detectors sitting in one neutrino beam. The Short-Baseline Near Detector (SBND) is the closest to where the neutrino beam is created. MicroBooNE, the first of the three detectors to become operational, sits in the middle. ICARUS, the largest of the three, is the furthest. Taken from Fermilab Creative Service.

sitioned along the Booster Neutrino Beam (BNB) at Fermilab, each at varying distances from the target. The main characteristics of these detectors are summarized in Table 2.1.

	Baseline	Total LAr mass	Active LAr mass
SBND	110 m	220 ton	112 ton
MicroBooNE	470 m	170 ton	89 ton
ICARUS	600 m	760 ton	476 ton

Table 2.1: Summary of the main SBN detector features.

The three SBN detectors are all based on Liquid Argon Time Projection Chamber (LArTPC) technology, as will be explained in section 2.1.3. Utilizing the same detection technology and medium for neutrino interactions allows to minimize systematic uncertainties when comparing event distributions at various locations along the beam and searching for oscillation signals.

The neutrino spectra observed at ICARUS — the far detector within the SBN program — will be juxtaposed with those recorded at a distance of 110 m from the BNB target by SBND, which is presently undergoing commissioning. Meanwhile, the MicroBooNE detector, located in the Liquid Argon Test Facility (LArTF) at a distance of 470 m, has concluded its data collection phase, yielding groundbreaking insights into ν -Argon interactions. Finally, ICARUS-T600 serves as the far detector in the SBN program, boasting a 476-ton active mass and situated 600 m from the target. The detector concluded its commissioning phase in June 2022 and has since been actively collecting physics data. Figure 2.1 illustrates the layout of the SBN project. The placements of the detectors were strategically chosen to optimize sensitivity to neutrino oscillations over short baselines.

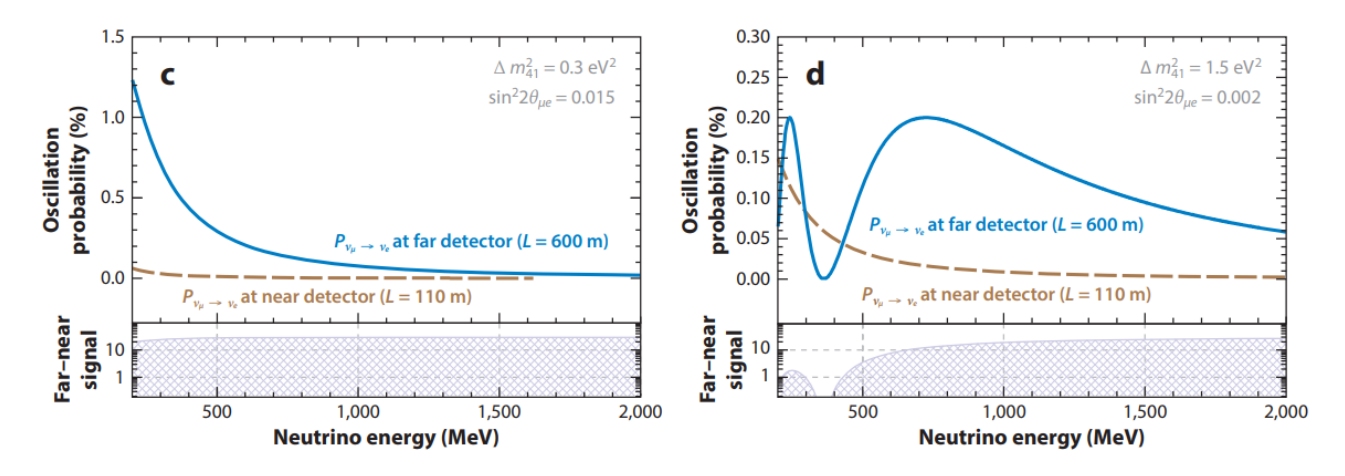


Figure 2.2: $\nu_{\mu} \rightarrow \nu_{e}$ oscillation probability as a function of energy in the 3+1 model at 110 m and 600 m, for two sets of parameters: $\Delta m_{41}^2 = 0.3 \,\mathrm{eV}^2$ and $\sin^2{(2\theta_{\mu e})} = 0.015$ on the left, $\Delta m_{41}^2 = 1.5 \,\mathrm{eV}^2$ and $\sin^2{(2\theta_{\mu e})} = 0.002$ on the right. The lower panels in each plot show ICARUS over SBND appearance probability ratio. Taken from [73].

2.1.1 Physics goals

The SBN program at Fermilab offers the possibility to conduct precision searches for new physics in neutrinos by recording millions of neutrino CC and NC interactions on Argon, shedding light on neutrino physics at the GeV energy scale. SBN primary objective is to investigate the potential existence of eV mass-scale sterile neutrinos and this is of paramount importance, necessitating follow-up experiments to either validate or refute the existence of these hypothesized neutrino states. A discovery would not only unveil new physics but also pave the way for further exploration in this field, while a clear null result from SBN would help close the long-standing puzzle of anomalies in neutrino physics.

Moreover, there will be opportunities to conduct high-precision studies on neutrino interactions with argon, laying the groundwork for future experiments based on LArTPC technology such as DUNE. SBN will serve as a platform for the development of LArTPC neutrino detector technology. Finally, the program will explore several Beyond the Standard Model (BSM) theories. A more comprehensive overview of the physics objectives of SBN is provided below.

Sterile neutrino searches

The SBN program was crafted with the deployment of multiple LArTPC detectors at precise baselines, aiming to enhance sensitivity to short-baseline sterile neutrino oscillations both in the $\nu_{\mu} \rightarrow \nu_{e}$ appearance and $\nu_{\mu} \rightarrow \nu_{\mu}$ disappearance channels [72]. Leveraging the SBND-ICARUS near-far detector combination facilitates direct comparison of events between the near and far detectors, and LArTPC technology offers a significant advantage for SBN in its sensitive search for anomalous neutrino signals. As detailed in section 2.1.3, the radiation length of Argon $X_0 = 14 \,\mathrm{cm}$, coupled with millimeter-scale event imaging and reconstruction capabilities, allows for clear differentiation between photon and electron-induced electromagnetic showers, capability

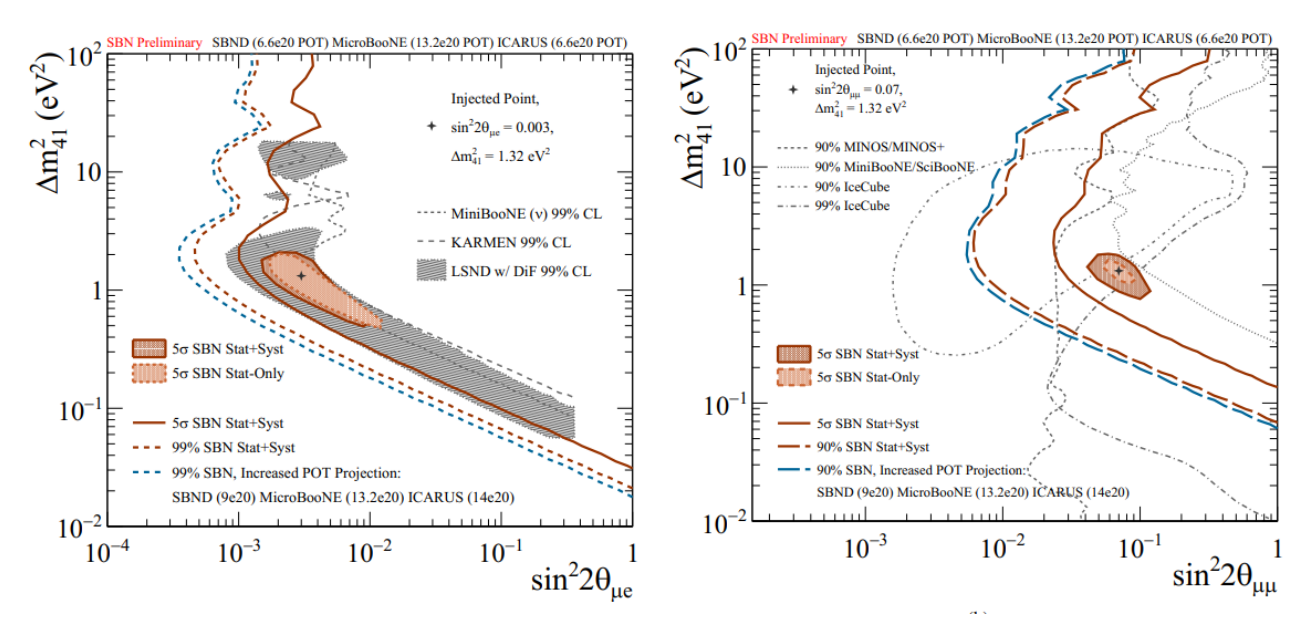


Figure 2.3: Status of the expected SBN sterile neutrino oscillation sensitivities with existing data, for the ν_e appearance channel on the left, and for the ν_μ disappearance channel on the right [41].

lacking in Cherenkov detectors like MiniBooNE. Notably, the global $\nu_{\mu} \to \nu_{e}$ appearance data point towards a mass splitting Δm_{41}^2 ranging between $0.3 \,\mathrm{eV}^2$ and $1.5 \,\mathrm{eV}^2$, with mixing strength $\sin^2{(2\theta_{\mu e})}$ between 0.002 and 0.015, as discussed in section 1.3.1.

Figure 2.2 illustrates the $\nu_{\mu} \to \nu_{e}$ oscillation probability both for SBND at a baseline of 110 m and for ICARUS at a baseline of 600 m, presenting two sets of parameters: $\Delta m_{41}^2 = 0.3 \,\mathrm{eV}^2$, $\sin^2{(2\theta_{\mu e})} = 0.015$ and $\Delta m_{41}^2 = 1.5 \,\mathrm{eV}^2$, $\sin^2{(2\theta_{\mu e})} = 0.002$. The oscillations are identifiable in the far detector across that entire range of oscillation parameters measured by global analyses. For larger Δm_{41}^2 values, a slight oscillation signal emerges at low neutrino energies in the near detector as well. However, the distinctive shape and heightened oscillations at most energies observed in the far detector maintain an high sensitivity when utilizing the near-far combination.

Overall, the SBN program is expected to gather data for a minimum of three years to encompass the allowed region associated with the LSND anomaly, with a sensitivity of 5σ . The current status of projected SBN oscillation sensitivities for the $\nu_{\mu} \rightarrow \nu_{e}$ appearance and the $\nu_{\mu} \rightarrow \nu_{\mu}$ disappearance channels is illustrated in Figure 2.3. All statistical uncertainties are calculated assuming a 6.6×10^{20} POT exposure from the BNB for both SBND and ICARUS, equivalent to approximately three years of operation. Systematic uncertainties linked to event rates and fluxes are determined through dedicated BNB simulations [74], while an uncorrelated detector systematic uncertainty of 3% is assumed. It's important to underline that simultaneous study of the ν_{e} -appearance and ν_{μ} -disappearance channels, made possible by utilizing an intense muon neutrino beam and multiple detectors, is crucial for addressing the existing tension between the data from these two channels.

The ICARUS detector will focus on seeking evidence for sterile neutrino claims made by the Neutrino-4 experiment [64] during its early runs, before the activation of the SBND detector,

i.e. oscillations in the ν_{μ} disappearance channel with BNB and in the ν_{e} disappearance channel with NuMI produce patterns at the same $L/E \sim 1-3 \mathrm{m \, MeV^{-1}}$ but with energies higher by a factor of 100 compared to the Neutrino-4 case. It's noteworthy that the L/E effect is primarily associated with energy variation, considering that the baseline can be assumed as constant and large for both BNB and NuMI.

Cross section measurements

Precise measurements of neutrino-Argon cross sections are essential for any experiment employing the LArTPC approach, including the DUNE experiment [75, 76]. Neutrino interactions with Argon in the energy range of $\sim 1\,\text{GeV}$ encompass a wide array of final states. In addition to leptons in the primary CC channels, more complex CC or NC states are possible, such as those involving the emission of nucleons, pions, or other hadrons. The SBN program is well-positioned for such a study due to the excellent particle identification capabilities of LArTPC technology. Moreover, the BNB provides neutrinos spanning from a few hundred MeV up to a few GeV, with its flux thoroughly characterized by extensive studies with MiniBooNE [74].

Furthermore, the three detectors within the SBN program are expected to capture millions of neutrinos, enabling them to achieve world-leading measurements of ν_{μ} -Ar and ν_{e} -Ar cross sections. ICARUS also receives neutrinos from the off-axis NuMI beam, characterized by a larger electron neutrino content and a different energy spectrum compared to the BNB, as well as MicroBooNE and neutrino-Argon cross section can be also studied from NuMI beam. A first measurement of the neutrino-Argon interaction cross section has been made available by the MicroBooNE collaboration [77].

BSM physics searches

At SBN, the excellent event reconstruction and particle identification capabilities of LArTPC technology, combined with high-intensity neutrino beams, allow for exploration of new physics scenarios. BSM theories mainly involve either deviations from standard neutrino oscillations or the emergence of novel experimental signatures, which include the existence of heavy sterile neutrinos, dark neutrino sectors, light dark matter, and decays of light sterile neutrinos [73].

2.1.2 Neutrino beams

The ICARUS detector primarily relies on the on-axis BNB [72], with additional value derived from independent investigations into off-axis neutrinos from NuMI [78]. These studies are also pertinent for upcoming long baseline experiments employing similar technology such as DUNE. A more detailed description of the neutrino beams used in SBN follows.



Figure 2.4: Map of the Fermilab neutrino beamline area showing the axis of the BNB (yellow dashed line) and approximate locations of the SBN detectors at 110 m, 470 m, 600 m. The pink line indicates the axis of the NuMI neutrino beam. Taken from [72].

Booster Neutrino Beam

SBN program utilizes the Booster Neutrino Beam (BNB) generated through a multistep process. Protons are first extracted from the 400 MeV Linac and accelerated to a kinetic energy of 8 GeV in the Booster synchrotron, then directed onto a beryllium target, producing a secondary beam mainly composed of pions. The fluxes of these particles are well understood, thanks to detailed calculations developed by the MiniBooNE collaboration [74] and data on hadron production acquired by the HARP experiment [79].

To focus the secondary particles, a magnetic polarizing horn is utilized, delivering 174 kA in 143 µs pulses synchronized with the proton delivery. Based on the horn's polarization, positive or negative particles are selectively focused and collimated, while the others are defocused. The focused mesons propagate through a 50 m long tunnel, where the majority decay to produce ν_{μ} and ν_{e} . The dominant decay channel for pions is $\pi^{+} \to \mu^{+}\nu_{\mu}$, with a branching ratio $\sim 99.988\%$. The length of the decay pipe is optimized to maximize the production of $\nu_{\mu}/\overline{\nu_{\mu}}$ while minimizing the probability of secondary muons decaying into $\nu_{e}/\overline{\nu_{e}}$. Any remaining particles are stopped by a concrete and steel absorber at the end of the 50 m decay region to prevent further weak decays that might contaminate the beam.

Each spill lasts for $1.6\,\mu s$, delivering nominally $\sim 4.5 \times 10^{12}$ protons per spill to the beryllium target. The beam structure consists of 81 bunches of protons, each approximately $\sim 2\,n s$ wide and spaced 19 ns apart, with an average spill delivery rate of 5 Hz. The neutrino fluxes observed at the three SBN detector locations are illustrated in Figure 2.5. These neutrinos, produced in the BNB, are peaked around $\sim 0.7\,\text{GeV}$ and range between 0 and 3 GeV across the spectrum.

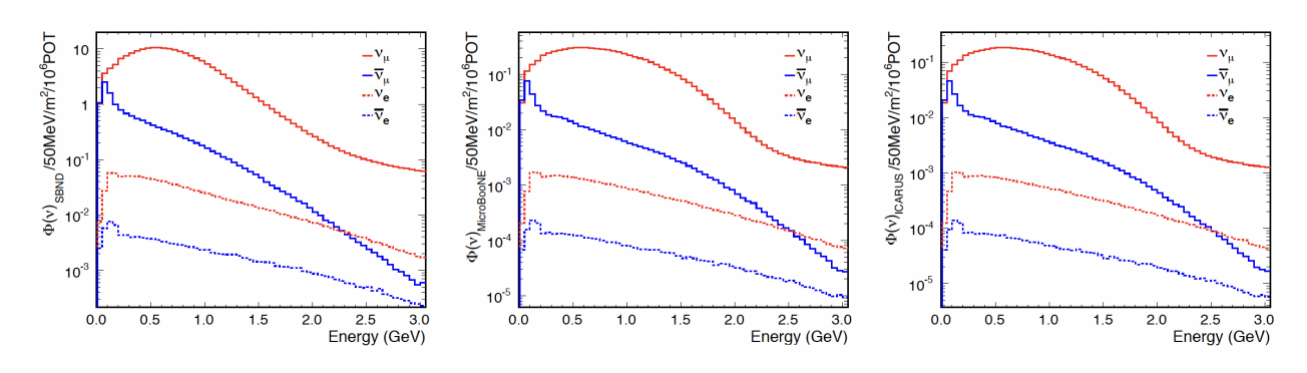


Figure 2.5: Neutrino components of the flux distribution for each SBN detector. The plot on the left corresponds to the nearest detector, SBND, while the distribution on the right illustrates the furthest detector, ICARUS. Solid lines represent the muonic contribution, with red indicating neutrino mode and blue indicating antineutrino mode, while dashed lines represent electronic contamination [72].

The composition of the flux in the neutrino mode varies with energy, but it is predominantly composed by $\sim 93.6\%$ of ν_{μ} , followed by $\sim 5.9\%$ of $\overline{\nu_{\mu}}$, with an intrinsic $\nu_e + \overline{\nu_e}$ contamination at the level of 0.5% below 1.5 GeV. A significant portion of the electron neutrino contamination originates from the pion to muon decay chain, with the remaining coming from decays of K^+ and K^0 . Note that BNB can operate in both neutrino and antineutrino modes, hinging on the polarization of the magnetic horns: a forward horn current focuses π^+ particles to generate a beam dominated by ν_{μ} , while a reversed horn current collimates the π^+ particles to yield a beam dominated by $\overline{\nu_{\mu}}$. However, there are currently no immediate plans to transition from the current forward mode to reversed mode.

Neutrinos at the Main Injector

The Neutrinos at the Main Injector (NuMI) beam is the world's most potent neutrino beam, generated from 120 GeV protons extracted from the Fermilab Main Injector. Protons are accelerated up to 8 GeV in the Booster, and once they reach the nominal energy they are transferred to the Main Injector, with a circumference seven times that of the Booster. This configuration enables the injection and storage of seven Booster batches, however only a maximum of six proton batches can be accelerated due to the last slot being allocated for the pulse kicker rise time. Through sophisticated techniques and hardware enhancements, proton intensity has been significantly increased over time, currently reaching up to 120 GeV with a power of 1 MW. Following acceleration, protons are directed towards the MINOS Far detector to a graphite target positioned at 350 m. Upon collision, hadrons are produced and focused by two magnetic horns before entering a 675 m long decay pipe, where they decay into neutrinos or antineutrinos [72].

Pions and kaons constitute a significant portion of the hadrons and predominantly decay via the modes $\pi^+ \to \mu^+ \nu_\mu$ and $K^+ \to \mu^+ \nu_\mu$, thus yielding a ν_μ beam. There is also a small percentage of $\overline{\nu_\mu}$ component originating from negative hadrons, along with a minor contamination of ν_e arising from subdominant electronic decay modes of K^+ and K^0 , as well as tertiary muons [72]. Similar to the BNB, the polarity of the NuMI horns can be reversed to generate either a neutrino

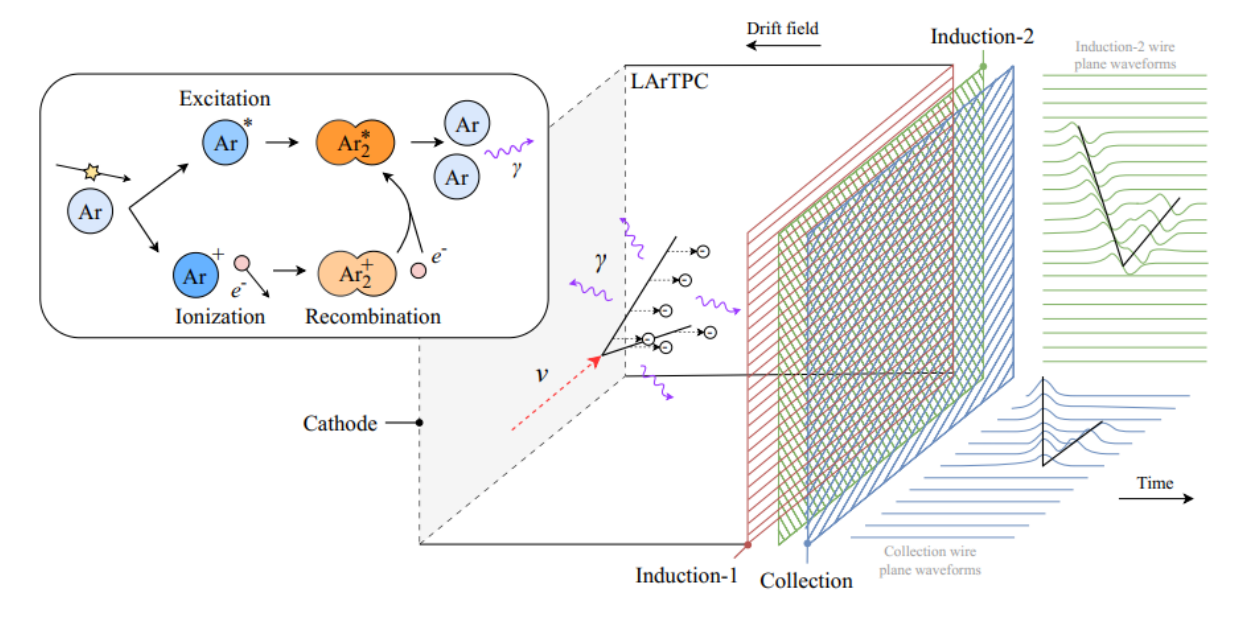


Figure 2.6: Working principle of the LArTPC technology. An incoming neutrino interacts with an Ar atom, producing charged ionizing particles: Ar^+ ions drift toward the cathode plane on the left and e^- drift towards the anode, represented by the three Induction-1, Induction-2, Collection wire planes. Scintillation light is produced and propagates inside the TPC. Taken from [41].

or antineutrino-dominant beam. A hadron monitor positioned at the end of the decay volume, just before the 5 m thick absorber, records the residual hadron profile. The subsequent 240 m of rock serves to halt any remaining muons in the beam while allowing neutrinos to pass through undisturbed. NuMI has the capacity to deliver up to 6.5×10^{13} protons per spill, with a beam pulse width of 9.6 µs. The ICARUS detector also utilizes this beam, primarily focusing on the interaction rates of neutrinos with argon nuclei. Positioned 795 m downstream from the NuMI beam at an off-axis angle of 5.7°, ICARUS receive an off-axis neutrino beam in the energy range of $0-3 \,\mathrm{GeV}$ [72] with an enriched component of electron neutrinos.

2.1.3 Liquid Argon TPC

The LArTPC technology was first proposed by Carlo Rubbia [69] to address the requirement for a device capable of combining extensive information on the topology of a neutrino event, typical of a bubble chamber, with the larger mass, the precise timing and the enhanced flexibility characteristic of electronic detectors. Historically the ICARUS collaboration was the first to successfully developed this technology, that has consistently been improved through experiments, while at the same time making groundbreaking physics measurements. The working principle of a LArTPC is pictured in Figure 2.6 [80].

When a neutrino interacts with liquid Argon, it generates charged ionizing particles. As these particles propagate through the medium, they ionize and excite Argon atoms: consequentially, pairs of electrons e^- and ions Ar^+ are generated, and the application of an electric field makes them drift towards the anode and the cathode of the TPC, respectively. The electric field is

established along the drift direction x by a potential difference between the cathode and the anode planes, which provides a projection on the yz plane of the particle trajectory. The anode consists of 3 planes of sensing wires called respectively Induction-1, Induction-2, and Collection. The drift time of electrons is used to reconstruct the missing coordinate, allowing a complete three-dimensional track reconstruction.

The position in the yz plane, perpendicular to the drift direction, is determined from the signals in the three wire planes. The drift coordinate x of the ionization electron is derived from timing information. Scintillation light produced by the event serves as a prompt signal and is utilized, alongside beam information, to assign a time t_0 to the interaction. Given the time t the electron arrived at the anode wires and knowing the drift velocity v_{drift} , it is possible to derive x as

$$x = v_{\text{drift}}(t - t_0) \tag{2.1}$$

When a charged ionizing particle crosses the liquid Argon, two different processes can lead to the production of scintillation light. The first

$$Ar^* + Ar \rightarrow Ar_2^* \rightarrow Ar + Ar + \gamma$$
 (2.2)

described an excitation of Argon atoms, leading to the formation of excited Ar_2^* molecules that then decay producing scintillation photons. The second

$$Ar^+ + Ar \rightarrow Ar_2^+ e^- \rightarrow Ar_2^* \rightarrow Ar + Ar + \gamma$$
 (2.3)

describes the recombination of ionized Argon atoms with electrons, whose light yield depends on the energy loss of the ionizing particle and on the electric field. This process requires an electron cloud surrounding the Ar_2^+ to occur, hence the scintillation yield will be dependend of the electric field: in LArTPCs where the ionization electrons are drifted towards the anode, this process is highly suppressed.

The production of scintillation photons is proportional to the energy deposited by the ionizing particle. In absence of a drift electric field, both processes result in the emission of $\sim 40,000$ monochromatic Vacuum-Ultra-Violet (VUV) photons per MeV, with a wavelength $\lambda \sim 128$ nm. The emitted light exhibits a fast $\tau \simeq 6$ ns and a slow $\tau \simeq 1.5$ µs decay component, with their relative intensity depending on the stopping power of the ionizing particle. LAr is transparent to such scintillation light, allowing it to propagate in the TPC volume with minimal attenuation. The detection of the scintillation photons is facilitated by a light detection system immersed in the liquid Argon behind the wire planes, facing into the detector volume, and this plays an important role in determining the absolute timing of events, positioning tracks along the drift coordinate for triggering purposes and potentially for calorimetry. In ICARUS, photomultiplier tubes (PMTs) are utilized for light detection: this will be the focus of section 2.2.2.

The use of liquid Argon

Argon was identified as the optimal target material due to its properties [69]. Being a noble gas, it does not readily bind with electrons, resulting in minimal energy absorption by atoms from charged particles passing through the detector. With a high density of $1.4 \,\mathrm{g\,cm^{-3}}$, liquid Argon offers a significant interaction probability for neutrinos and high electron mobility. Also, the radiation length of liquid Argon $X_0 = 14 \,\mathrm{cm}$, enables precise mm-scale calorimetry in a LArTPC, facilitating accurate discrimination between electron and photon-induced activities along the particle's path. The identification of a photon signature occurs when a gap between the interaction vertex and the initiation of an electromagnetic shower is observed. Furthermore, the conversion of a photon into a positron-electron pair manifests as an ionization pattern consistent with two Minimum Ionizing Particles (MIPs) developing an electromagnetic shower, distinguishing it from the single-MIP deposit of an electron.

This capability allows for the efficient identification of electron neutrino events, significantly reducing NC background in neutrino oscillation studies. Moreover, in highly purified liquid Argon, free electrons resulting from ionization can be efficiently transported over macroscopic distances of meters; this necessitates maintaining extremely low concentrations of electro-negative impurities on the order of 100 parts per trillion (ppt), to achieve a desired electron lifetime [81].

Moreover, Argon is quite economical and relatively easy to obtain, being the third most abundant element in Earth's atmosphere and can be liquefied by cooling it with Nitrogen, making it the ideal noble gas to use for this type of detector. The cryogenic temperatures at which Argon is found in its liquid phase introduce the additional need to consider a cryogenic cooling system to ensure safety and operational stability. In summary, liquid Argon is an excellent medium to use for a neutrino detector that exploits TPC technology, but it is important to consider the complicated structure of Argon nuclei that introduces additional nuclear effects [69].

2.2 The ICARUS-T600 detector

The ICARUS-T600 detector consists of a warm vessel housing two adjacent identical ICARUS-T300 modules, commonly designated as the West and the East module, each boasting a volume of $3.6 \times 3.9 \times 19.6 \,\mathrm{m}^3$ and containing a cryostat accommodating two LArTPCs separated by a shared central cathode. A set of heat exchangers filled with LN₂, positioned between the insulation warm vessel and the aluminum containers of the modules, acts as a cold shield, preventing external thermal insulation heat from reaching the LAr containers. Thermal insulation is kept by a 60 cm thick polyurethane foam panel, ensuring a uniform and stable temperature of 89 K (within a tenth of K) of the cryostats. Figure 2.7 illustrates a schematic of the ICARUS-T600 detector, highlighting its main components which will be detailed in subsequent sections.

Each TPC of the ICARUS-T600 detector have a maximum drift distance of 1.5 m; given that

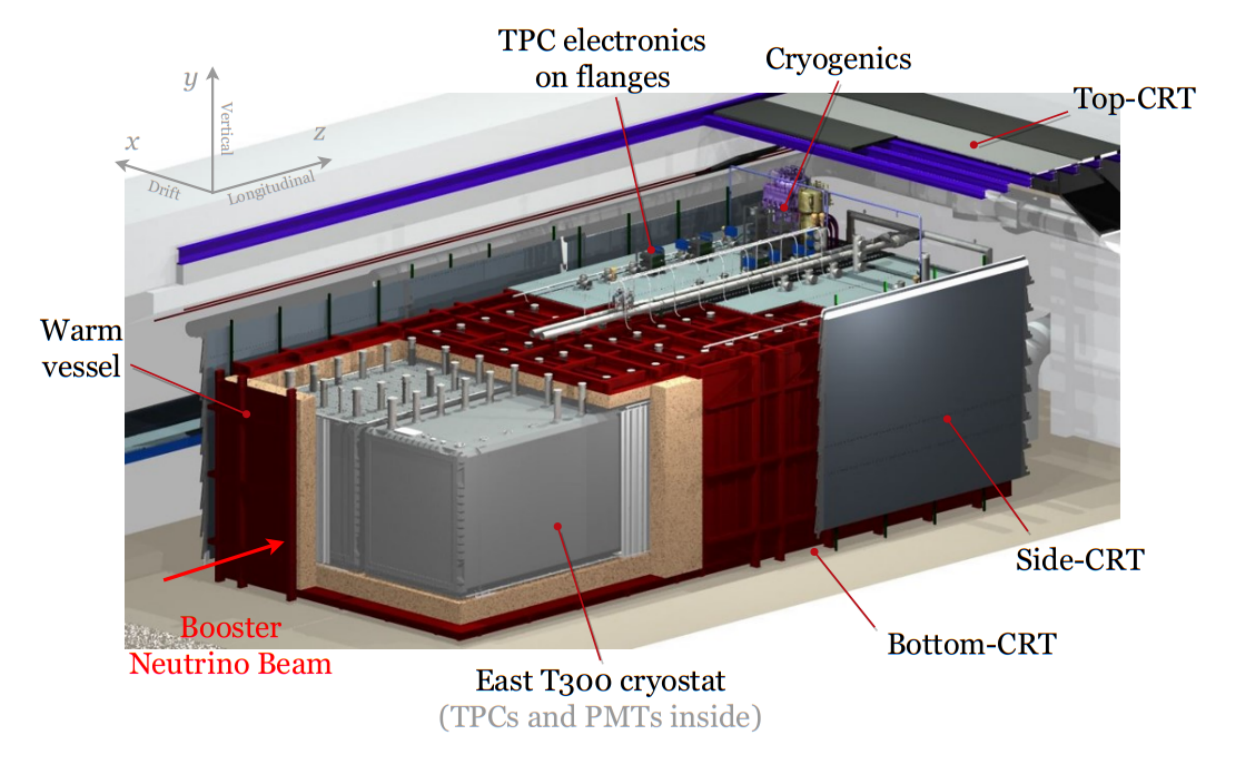


Figure 2.7: Schematic of the ICARUS-T600 detector at Fermilab, with its basics. The insulated warm vessel houses the two ICARUS-T300 modules and is surrounded by the CRT system. On top of the vessel, one can find the TPC electronics and the proximity cryogenics. Taken from [41].

the nominal value of the electric drift field in ICARUS is $E_{\rm drift} = 500 \, {\rm V \, cm^{-1}}$, this corresponds to an electron drift time of $\sim 1 \, {\rm ms}$. The cathode comprises an array of nine panels composed of pierced stainless steel, allowing for $\sim 58\%$ optical transparency between adjacent drift regions.

The anode consists of 3 parallel planes of sensing wires, spaced 3 mm apart from each other. Each TPC has a total of 13312 wires, so globally 53248 wires are installed in the detector. Each wire has a diameter of 150 µm and a variable length depending on its orientation: in ICARUS the Induction-1 plane features horizontal wires split into two 9 m long wires; the Induction-2 plane has wires oriented at 60° with respect to the horizontal direction; the Collection plane has wires oriented at -60° . This orientation was originally chosen due to the fact that ICARUS was conceived to be a cosmic ray detector, and cosmic particles mainly enter from the top and cross the detector exiting downwards: such configuration would therefore maximise the number crossed by a cosmic ray. The Induction planes provide bipolar signals in a non-destructive way, given that an appropriate voltage biasing is applied to the three wire planes. More specifically, for optimal transparency, the nominal drift field $E_{\rm drift} = 500\,{\rm V\,cm^{-1}}$ between the Induction-1 and the cathode satisfies the conditions $E_2 \geq FE_1$ and $E_1 \geq FE$, where E_1 and E_2 represent the field values in the gaps between Induction-1 to Induction-2 and Induction-2 to Collection, respectively [82]. The required field-scaling factor F typically ranges from 1.2 to 1.5, with the nominal values of potential at which the three wire planes are biased of $-250 \,\mathrm{V}$, $-30 \,\mathrm{V}$, $250 \,\mathrm{V}$, respectively. In this way, the Collection plane is able to fully collect the ionization charge and return it as a unipolar signal. This charge signal detected in the Collection view is proportional to the deposited energy allowing for the calorimetric measurement of the particle energy; each

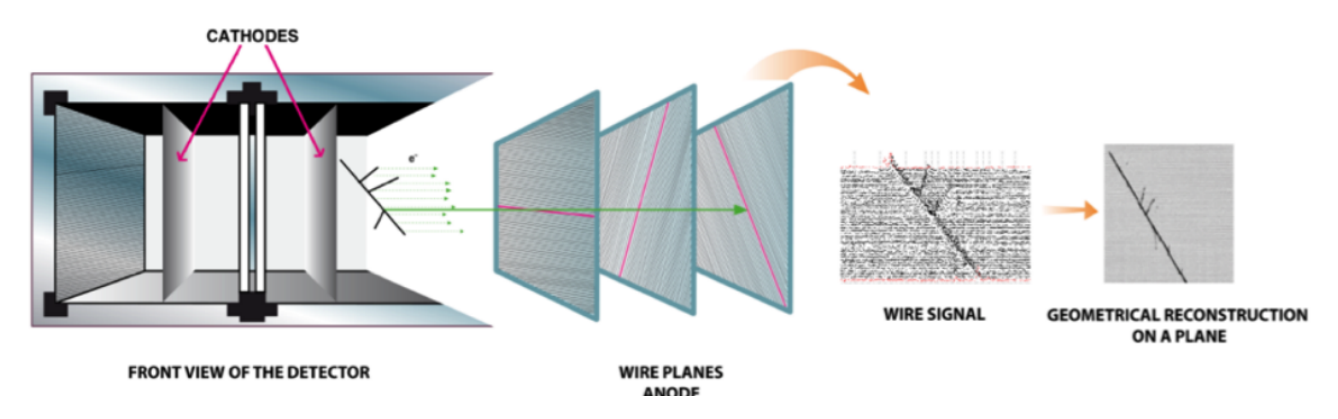


Figure 2.8: Sketch of detector layout showing the LArTPC working mechanism. Taken from [83].

wire is read out as a single channel, allowing for reconstruction of the ionization pattern from the recorded wire signals, and determining the 3D location where each ionization electron was produced. Figure 2.8 shows how a 3D image of a ionizing event is reconstructed. More on event reconstruction will be available in Chapter 3.

During the operation period at LNGS, thanks to the detector exposure of the CNGS neutrino beam and collection of cosmic rays, the event reconstruction proved the high-level performance and physical potential of the LArTPC technology. ICARUS confirmed a resolution of the order of mm³ on an overall active volume of $340 \,\mathrm{m}^3$, allowing the particle identification and the study of the event topology by the energy deposition per track length $\mathrm{d}E/\mathrm{d}x$ as a function of the particle range.

ICARUS claimed an efficient identification of electrons taking advantage of its characteristic electromagnetic showering (presents a behaviour well separated from π^0 reconstructed through its decay photons), the dE/dx comparison, a π^0 invariant mass measurement at the level of 10^{-3} and the identification of a photon conversion gap at the primary vertex. In addition the high density of sampling ($\sim 2\%$ of a radiation length) and the signal to noise ratio of $\sim 10/1$ on individual wires reported by ICARUS allowed to efficiently identify CC ν_e interactions, while rejecting NC to a negligible level. Moreover the good calorimetric response of the detector [84] allowed to claim an estimated electromagnetic energy resolution of $\sigma_E/E \simeq 3\%/\sqrt{E[\text{GeV}]}$, in agreement with the $\pi^0 \to \gamma\gamma$ invariant mass measurements in the sub-GeV energy range, and an estimated resolution for hadronic showers of $\sigma_E/E \simeq 30\%/\sqrt{E[\text{GeV}]}$.

The commissioning phase at FNAL, or "Run 0", was used to develop, test and tune the event reconstruction algorithms. The "Run 1" started on June 9th, 2022 and lasted until July 10th, 2022; the "Run 2" started on December 20th, 2022 and lasted until July 14th, 2023; the "Run 3" started on March 15th, 2024 and ended on July 11th, 2024; the "Run 4" started on December 10th, 2024 and is currently running. The collected-over-delivered proton on target (POT) efficiency is estimated to be about 98%. The delivered and collected event statistics for physics analyses is currently 1.40×10^{20} and 1.37×10^{20} POT, respectively, for "Run 4".

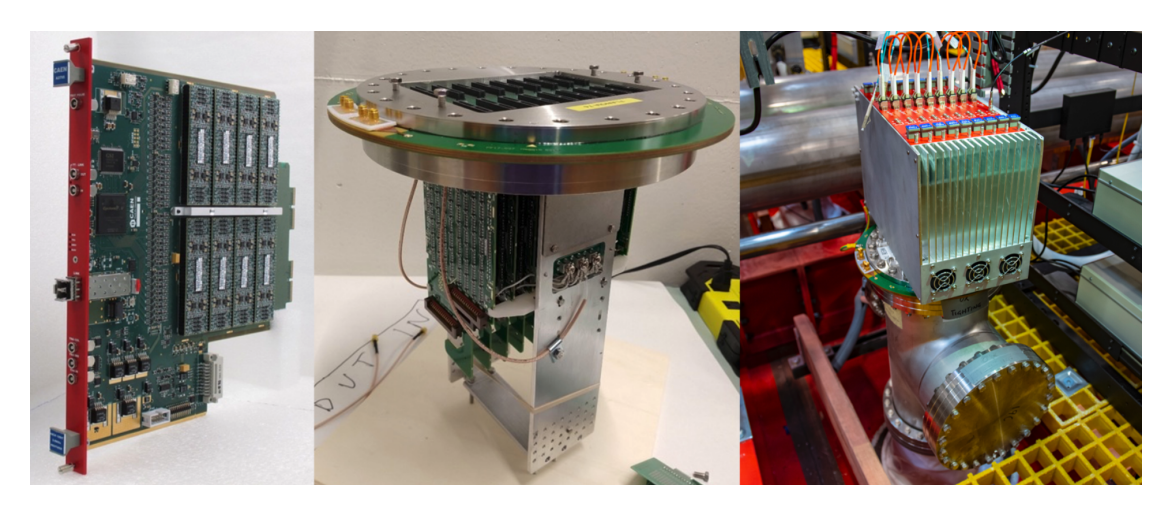


Figure 2.9: On the left, an A2795 custom board housing 64 amplifiers, analog-digital converter, digital control and optical link. In the middle, an assembled feed-through with nine DBBs and the biasing cables. On the right, a mini-crate populated by 9 A2795 boards installed on a feed-through flange and placed on top of the chimney. Taken from [85].

2.2.1 TPC read-out electronics

The high performance TPC read-out electronics equipping the T600 was designed to allow for continuous read-out, digitization and independent waveform recording of signals from each wire of the TPC for the drift time. It exploits an efficient performing and compact electronic devices, allowing for the processing of all three views and enabling calorimetry with appropriate signal-to-noise ratio S/N, and being thus able to handle crowded situations such as dense showers near the vertex [85]. The system allow a continuous triggerable multi-buffered waveform recorder for each wire of the detector. Each channel has a dedicated serial 12-bit ADC and the analog and digital parts are integrated in one electronic module that serves 64 channels. Moreover, the VME standard exploits a serial bus architecture with optical links allowing a Gb/s band-width data transmission.

The TPC wire signals are extracted from the cryostat through proprietary flanges on top of the chimneys and fed into the front-end amplifiers. These flanges accommodate electronic modules and Decoupling and Biasing Boards (DBBs) directly inserted on the external and internal sides of the flanges, respectively. The DBB boards have two main functions, first to bias each wire and secondly to convey the signal to the amplifiers by means of blocking capacitors.

The front-end electronics are housed in the CAEN A2795 motherboards, integrating both the analog and digital electronics for TPC signal processing. There are 8 pre-amplifiers, mounted on a small amplifier board, and 8 boards fit in each one of the 8 connectors of the A2795 board, for a total of 64 channels per board. A dedicated filter reduces the RMS serial noise and at the same time preserves the filtered signal area in the pass-band, linked to the charge information. The filter interfaces each pre-amplifier with its serial 12-bit, with a 400 ns sampling time ADC.

There are 9 A2795 boards, housed in a custom *mini-crate* mounted onto the feed-through flange on top of the chimney and designed for the transmission of the TPC wire signals. Each mini-

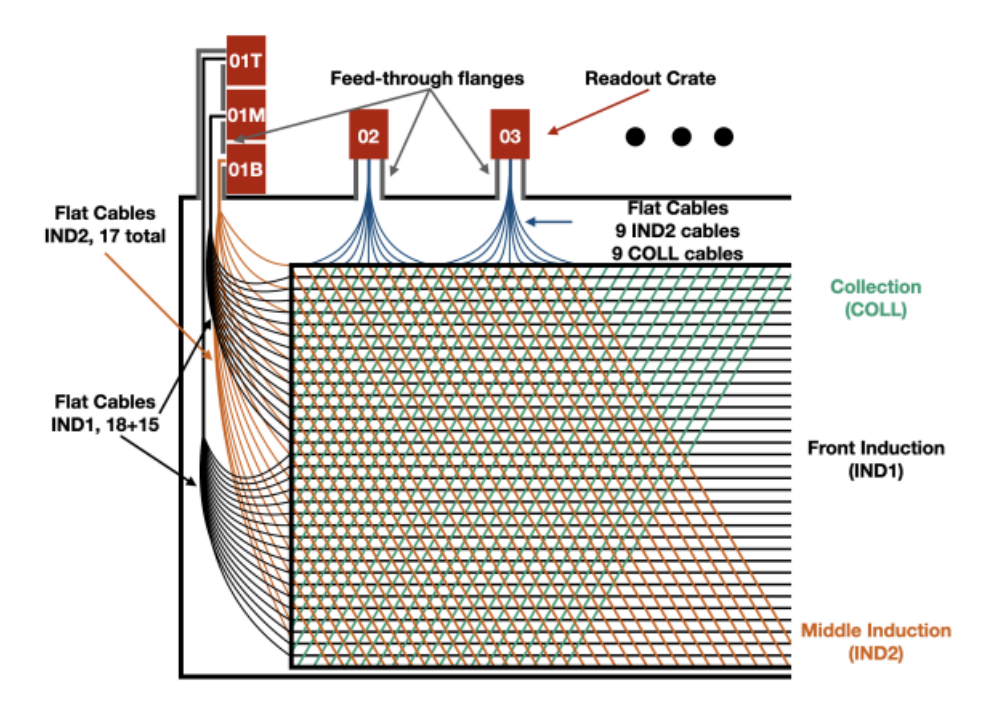


Figure 2.10: A diagram showing the geometry of the ICARUS TPC readout. The wires are connected in groups of 32 to cables and routed up to the feed-through flanges. A readout crate hosts 9 readout boards, each digitizing the signal from 2 cables for a total of 64 channels per board. Each of the lines denoting a wire represents 32 wires spaced by 3 mm.

crate is powered by a linear DC Low Voltage Power Supply (LVPS) module, designed with the requirement of extremely low noise: this was an important achievement, because it reduced the volume of the front-end electronics for each flange. Each set of 9 boards in a single crate are read out through two fibers. The full TPC electronics, composed of 96 mini-crates, is synchronized by a serial link cable which sends clock, trigger and commands information: these cables are distributed to all mini-crates by four fan-out modules with the same cable lengths, to guarantee equal time delay. More on electronics can be found in [83].

Noise measurement

The ICARUS TPC noise is characterized principally through measurements of the absolute noise scale, the frequency characteristics, and channel-to-channel correlations. A coherent noise, common to groups of 64 channels on the same readout board and generated on the readout board, was measured. An additional residual noise structure, generated by capacitive or inductive coupling between the cables, was detected. The geometry of the readout is important for understanding the noise observed in the detector, as schematized in Figure 2.10.

Due to the angle of each wire plane, there are necessarily some wires with no attachment point at the top edge of the detector. These wires are instead accessed through a single feed through flange on the corner of each TPC which hosts three readout crates. Two of these crates digitize signal from Induction-1, whereas the other digitizes signal from either Induction-2 or Collection depending on which plane on that end of the detector has wires inaccessible from the top. The

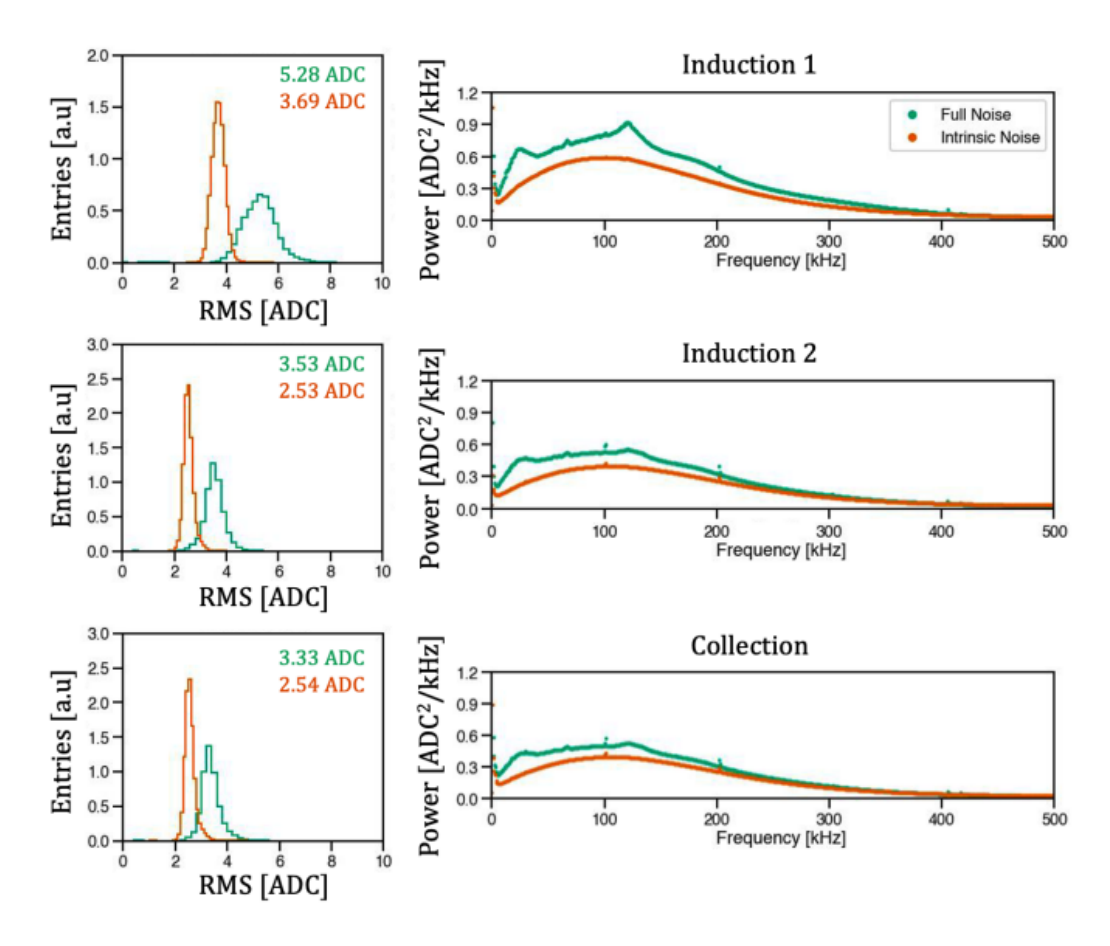


Figure 2.11: On the left: noise distributions per plane as characterized by the RMS of each waveform before and after coherent noise removal. Shown below each plot are the medians associated with each distribution. On the right: frequency characteristics of the noise per plane, as measured by the FFT spectra before and after coherent noise removal. Taken from [86].

additional wire and cable length for channels in Induction-1 results in higher overall noise, and the cables connecting the wires to the front-end are in significantly closer proximity due to the path down to the wires and the presence of three sets of cables in a signal feed-through flange.

A channel-to-channel correlation within a readout crate has been filtered out, depending on the waveforms of the channels. It can be calculated for each channel within a readout crate, and averaged across many events. Correlations between channels not in the same readout crate are not significant. The presence of significant correlations between channels in the same readout crate necessitates some degree of noise filtering. The portion of the waveform that remains after the removal of the coherent noise component is representative of the noise naturally present on the channel due to intrinsic noise sources. The separation between coherent noise and *intrinsic noise* allows for a more detailed characterization of the noise.

The noise distributions per plane are shown in Figure 2.11 (left). Induction-1 exhibits higher noise due to the longer flat cables and wires, while Induction-2 and Collection have similar noise levels, as they have similar wire and cable lengths. Variations in cable length for Induction-1 channels drive most of the additional width of Induction-1 noise distribution.

The frequency characteristics of each component of noise has been measured using the discrete Fast Fourier Transform. Figure 2.11 (right) shows the spectra per plane before and after the coherent noise removal. The intrinsic noise populates the expected distribution and is similar for all three planes. The coherent noise is present as as additional, less smooth spectrum on top of the intrinsic noise, and also exhibits two broad peaks at specific frequencies, not attributed to a specific source yet. At the lowest frequency bins there is a sharp increase due to oscillations in the waveforms: these oscillations are not coherent across groups of channels as evidenced by the full noise and intrinsic noise spectra exhibiting the same low-frequency trend.

Outside of hardware interventions, the detector noise has always been very stable. The biggest source of noise reduction was the disconnection of the Resistive Temperature Devices (RTDs) that read the temperature at various locations within the Argon, after which the noise was both significantly reduced and considerably less variable. Due to the locations of RTDs on the inner walls of the cryostat, the Collection plane was the most directly exposed plane, though the effect was highly localized and on average larger on Induction-1. A third reduction in the coherent noise due to the installation of Chebyshev low-pass filters on one of power supply lines of the readout boards, which reduces the coherent noise by a factor $\sim 20\%$.

As can be observed in Figure 2.11 the spectra for Induction-2 and Collection are nearly identical, but differ greatly from those of Induction-1, and this can be explained by the different readout geometry and total channel capacitance, the latter of which generally has the effect of scaling the noise. The general trend of Induction-2 presenting higher noise than Collection is observable in the history of the full noise. This appears to be related to the coherent noise component as the difference disappears after coherent noise removal. While the full noise shows noticeable changes at distinct points in time, the intrinsic noise is exceptionally stable, suggesting that it is only the coherent noise component which has evolved over time. The noise conditions within each physics run are expected to be relatively constant.

2.2.2 Light Collection System

As previously mentioned in section 2.1.3, when a charged particle traverses the LArTPC volume, VUV scintillation photons with $\lambda \sim 128\,\mathrm{nm}$ are emitted from the decay of $\mathrm{Ar_2^*}$ molecules, which are generated from the excitation of Argon atoms or the recombination of electron-ion pairs. The high scintillation light yield of liquid Argon ensures the production of ~ 24000 photons per MeV at the nominal drift field, corresponding to an expectation of 15 photo-electrons per MeV in each TPC. This light serves as a prompt signal characterizing an ionizing event, essential for absolute timing of events, triggering purposes and cosmic background rejection.

The Light Collection System of ICARUS [87] consists of 360 PhotoMultiplier Tubes or PMTs, arranged in groups of 90 PMTs per TPC, positioned ~ 5 mm behind the wire planes and facing towards the active volume of the LArTPCs, as can be seen in Figure 2.12. The PMTs feature Bialkali photocathodes on a Platinum undercoating, to ensure high performance at cryogenic



Figure 2.12: Internal view of an ICARUS-T300 module, during the refurbishing activities at CERN. The pierced cathode in the middle separates the two liquid Argon TPCs and the structures holding the 90 PMTs per TPC are visible. Taken from icarus.fnal.gov

temperatures and relatively high pressures as expected when they are immersed in liquid Argon. Additionally, a $200\,\mu\mathrm{g\,cm^{-2}}$ layer of TPB wavelength shifter was deposited by evaporation on the PMT windows to ensure sensitivity to VUV photons, resulting in a 12% quantum efficiency. PMTs can be calibrated in time using a laser system based on a laser diode, emitting laser pulses with a wavelength of $405\,\mathrm{nm}$ and a FWHM of $60\,\mathrm{ps}$, delivered to individual PMTs via optical fibers. More on PMTs can be found in [88].

The signal and power supply cables are organized in groups of 10 and routed through stainless steel chimneys mounted on the cryostat roof. All the cables are standardized at 44 m in length to ensure uniformity across different channels. 15 PMTs are connected to each digitizer board, which comprises a 16-channel 14-bit FLASH ADC sampling PMT signals at a rate of 500 MS/s and storing them in a 10 µs wide circular buffer to capture both the fast ($\tau_{\rm fast} \simeq 6 \, \rm ns$) and the slow ($\tau_{\rm slow} \simeq 1.6 \, \rm \mu s$) component of scintillation light. Each board combines two signals from adjacent PMTs using OR logic to generate LVDS 200 ns wide logic outputs for evaluation by the trigger electronics. Upon receiving a trigger request logic signal, active buffers on the digitizer boards are frozen, and stored data are made available for download, allowing data transfer rates of up to 80 MB/s. Overall, the signals from the 360 PMTs in the T600 detector are digitized by 24 digitizer boards, producing 192 LVDS lines in total as schematized in Figure 2.13.

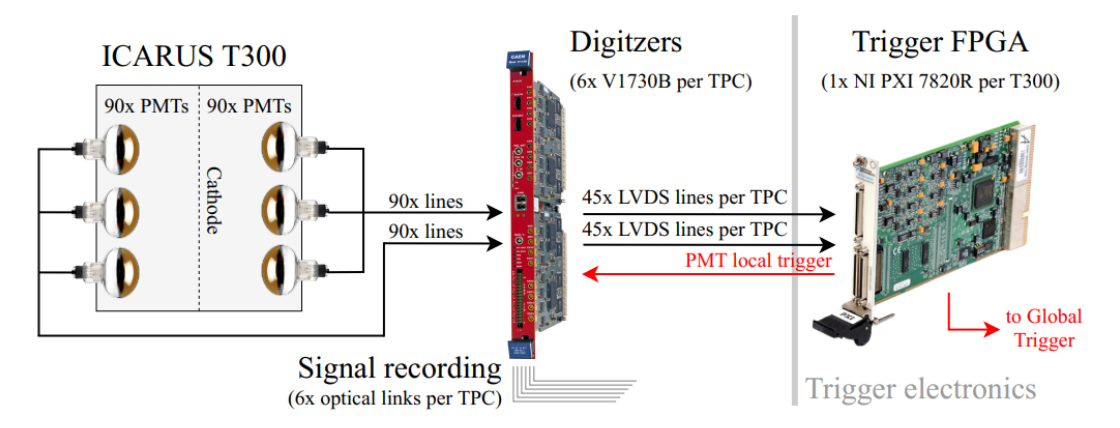


Figure 2.13: Deployment of the Light Collection System electronics, interfacing with the trigger electronics. For each module, 180 PMTs lines are digitized by 12 boards, which produce 96 LVDS output lines, later processed by a FPGA within the ICARUS Trigger System. Taken from [41].

The digitizer boards are housed in 8 crates, each equipped with a master unit facilitating the daisy chain distribution of trigger pulses and the 62.5 MHz frequency, both generated by the trigger electronics. These master units enable the acquisition of trigger pulses alongside the PMT signals, which is essential for timing purposes. To synchronize the reset of timestamps, a Pulse Per Second signal is transmitted to each board by the trigger electronics.

The primary $-2000\,\mathrm{V}$ high voltage required for the PMTs is generated by a power supply system, with one system allocated for each cryostat: this voltage is then precisely adjusted and distributed to the PMTs by 8 boards, each featuring 48 channels, and these boards are housed in a crate. This system ensures exceptionally low output ripple voltages, which are crucial for preventing PMT noise from being induced onto the wire planes.

2.2.3 Cosmic Ray Tagger

The ICARUS detector at Fermilab, situated on the surface, faces substantial cosmic ray activity. Consequently, the predominant background for various physics analyses comprises cosmic rays: on average, around 11 cosmic tracks are expected to cross the entire volume during each drift window, and this background — which may be mistaken for neutrino interactions — needs to be identified and suppressed. To address this issue, the Cosmic Ray Tagger system was developed to envelop the detector and identify cosmic muons definitively [72].

The CRT system comprises three subsystems covering the top, sides and bottom of the detector, employing plastic scintillator modules. The Top-CRT covers the top side and intercepts around 80% of the overall cosmic muon flux at ICARUS: it consists of 123 detector modules, including 84 horizontal and 39 vertical modules arranged along the cryostat's top surface, each containing two orthogonal layers of 8 plastic scintillator bars, with light collected by wavelength-shifting optical fibers and detected on both sides by Silicon PhotoMultipliers or SiPMs. The signals from SiPMs (32 in each module) are processed by a Front End Board to generate a trigger logic based on SiPM coincidence; additionally, a 2.85 m concrete overburden was added over the Top-CRT

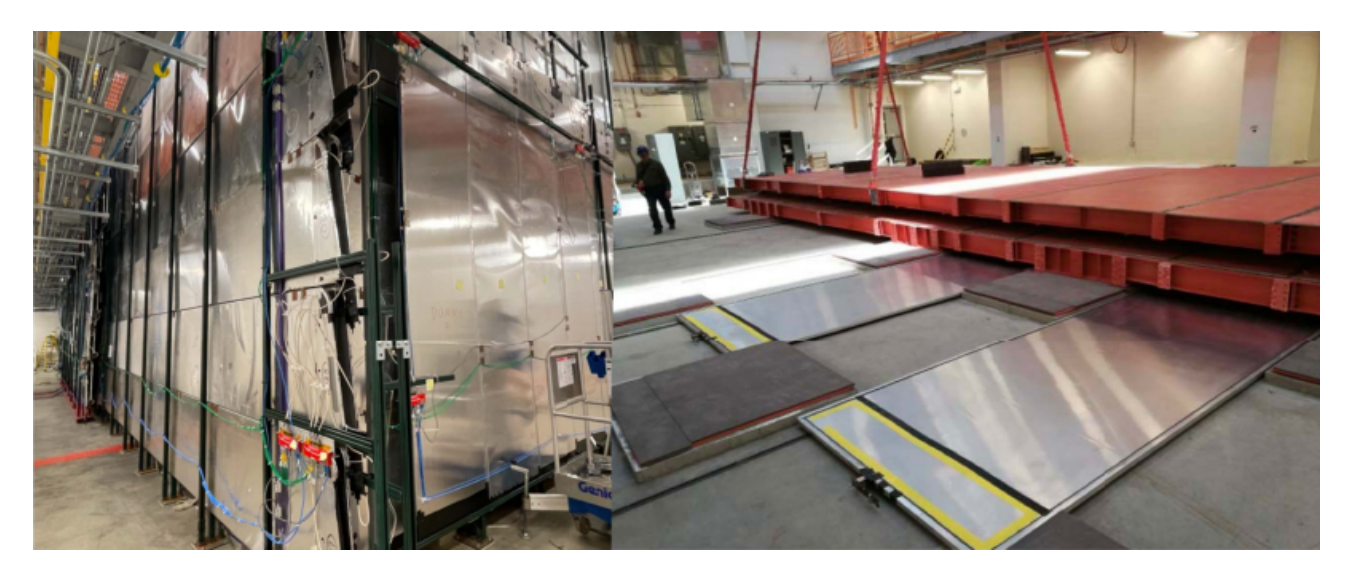


Figure 2.14: On the left, picture of the Side CRT south and west walls seen from the ICARUS building ground pit. On the right, the Bottom CRT module during the warm vessel deployment. From [89].

to shield the detector from cosmic radiation, absorbing a significant portion of cosmic photons and neutrons. In the horizontal Top-CRT, the rates decreased from approximately $0.6\,\mathrm{kHz}$ to $0.3\,\mathrm{kHz}$, while in the rim Top-CRT, they decreased from $0.3\,\mathrm{kHz}$ to $0.2\,\mathrm{kHz}$.

The Side-CRT subsystem covers instead the four vertical sides of the ICARUS T600 detector and comprises modules from the MINOS experiment, each including a metal sheath housing two layers of 20 Polystyrene scintillator strips with embedded wavelength-shifting fibers. Light signals are detected on both sides by arrays of SiPMs, totaling 2710 readout channels across 93 FEBs. Finally, the Bottom-CRT consists of 14 modules placed under the cryostats, organized into two chains, each with 7 modules from the Double Chooz experiment: each module comprises two layers of 32 Polystyrene strips with light, collected by wavelength-shifting fibers, detected on one end by multianode PMTs. More on the CRT system can be found in [89].

2.2.4 Trigger system and DAQ

The ICARUS-T600 detector is interested by an event rate of $\sim 0.29\,\mathrm{Hz}$ within the beam gates, equivalent to ~ 23000 events daily. Note that, in this context, by "event" we mean a neutrino interaction. This rate arises from the BNB events rate, with a spill duration of 1.6 µs and 5×10^{12} protons per spill at $\sim 4\,\mathrm{Hz}$ repetition rate; from the NuMI events rate, with a spill duration of 9.5 µs and 6×10^{13} protons per spill at $\sim 0.75\,\mathrm{Hz}$ repetition rate; and from background due to events such as cosmic muons crossing the detector in those few µs before proton extractions and random triggers. In order to handle this substantial volume of data, a multilevel trigger system is essential. This system is tasked with managing the data influx and selecting the relevant physical events. An additional offline step is then performed to further process the data and associate these events with genuine neutrino interactions.

The trigger system utilizes prompt scintillation light detected by PMT in coincidence with beam

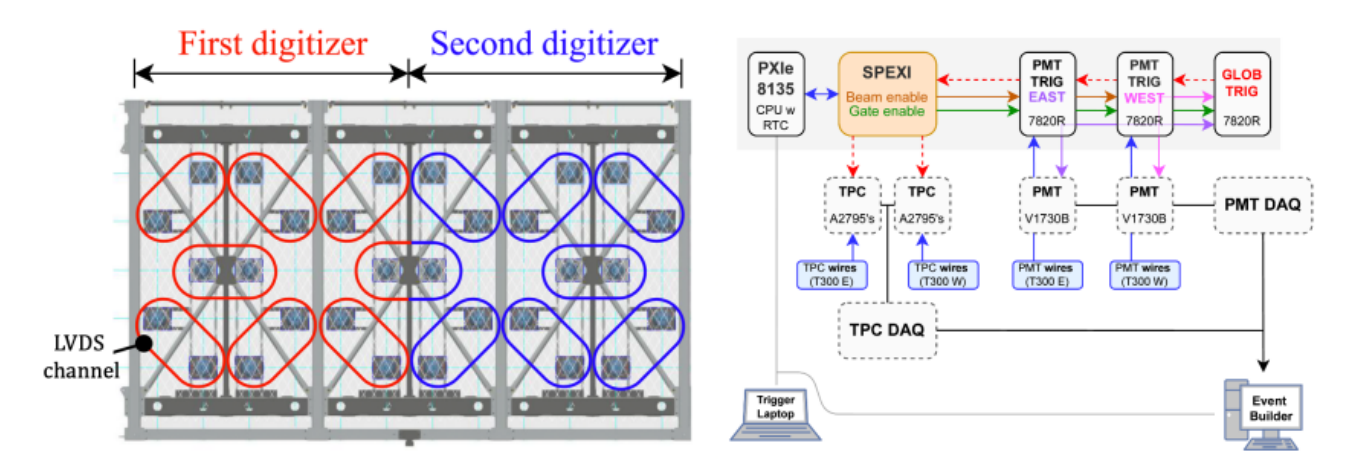


Figure 2.15: On the left, a 6-meters-long section of a TPC, where the position of the PMTs are shown together with the PMT pairs that provide the LVDS output and the portion of the detector that each digitizer is responsible for. On the right, representation of the trigger layout, including the PXIe Real Time Controller, the SPEXI board and the three FPGAs exploited for the trigger handling. From [41].

spill windows for neutrino beams, employing programmable logic boards. As briefly described in the subsection 2.2.2, the Light Collection System of ICARUS is composed of 90 PMTs per TPC, digitized through six V1730B boards per TPC with 16 channels each: 15 channels are used for the acquisition of PMT pulses, the last channel is used for the acquisition of auxiliary signals such as the beam gates and the trigger pulses, and for each channel an internal trigger-request logic signal is generated every time the sampled PMT pulse exceeds a programmable threshold. Using OR logic between two signals from adjacent PMTs, a Low-Voltage Differential Signaling (LVDS) logic signal is generated as output and activates subsystem read-outs. A schematic of the PMTs read by each digitizer and the PMT pairing geometry is shown in Fig. 2.15 left.

Beam spill gates are generated with precise timing using the White Rabbit network, synchronizing all subsystems with nanosecond accuracy. When a certain number of LVDS signals are present in the same TPC in temporal coincidence with the beam gate window, a *global trigger* is fired, and the data acquisition system (DAQ) activates the read-out of each detector subsystem: PMT waveforms and CRT signals are recorded around global triggers to tag cosmic rays during electron drift time. This is schematically illustrated in Fig. 2.15 right. Trigger logic is based on recognizing fired PMTs within limited longitudinal TPC regions, and each TPC wall is divided into consecutive 6 m slices, with the PMT LVDS signals processed accordingly. Then a multiplicity threshold of 5 LVDS channels, called *Majority-5*, was chosen as the best trade-off between an acceptable trigger rate to be sustained by the DAQ and a high trigger efficiency.

The described configuration was used during the commissioning phase, Run 1 and Run 2. Some upgrades were introduced in the trigger system during Run 3 to improve the event recognition for short tracks next to the detector corners or close to the PMT walls. In most of these cases, the PMT-majority requirement was not met due to a huge amount of light collected by a small number of PMTs. An additional trigger system, based on the scintillation light signal amplitude rather than the multiplicity of fired PMTs, was implemented. This relies on the adder boards,

which are custom-made boards to divide the PMT signal from 15 adjacent PMTs (corresponding to each group of PMT read by the same board), creating two lines to further evaluate trigger conditions. 24 adder boards summing up 5% of signal were installed within the entire ICARUS light collection system, leaving 95% of the signal amplitude as input to the digitizing boards.

The efficiency of trigger during the Run 3, as measured from *Minimum Bias triggers* – triggers for which the coincidence of light is not required – is estimated to be $\sim 85\%$ for energies between 70 and 200 MeV, $\sim 90\%$ for energies between 200 and 300 MeV, and reaches the plateau for energies greater than 300 MeV. More on trigger can be found in [41].

Data acquisition system

The DAQ employs the general artdaq data acquisition software development toolkit [90], which provides customizable applications for reading data from detector elements, called *BoardReaders*.

It allows to configure applications to perform event building, data logging and data dispatch to downstream online monitors for data quality processes, among many others. The BoardReaders acquire data fragments from the three detector subsystems readout electronics and from the trigger and White Rabbit timing systems. When an event is triggered, the corresponding trigger BoardReader sends its data fragment to the *EventBuilder*, which queries the other subsystems for data. Data is written to separate file streams depending on the trigger type: BNB on-beam, BNB off-beam, NuMI on-beam or NuMI off-beam, and corresponding Minimum Bias.

The BoardReader for the trigger systems sends a single fragment containing different kinds of information, such as the number of beam gates of each type in that specific DAQ run: this is then used offline for proper accounting of the total number of protons on target delivered and detector exposure within a run, essential information for oscillation analysis. Several tests were performed to evaluate the DAQ performance, successfully demonstrating that the system could stably handle trigger rates up to 5 Hz. However, given the neutrino interaction rate for the BNB and NuMI beams, it was considered more appropriate to use the PMT-based trigger system with the goal of maximizing the collection of physical events while minimizing the amount of non-physical data collected. Hence, in normal conditions the typical operational trigger rates, taking into account the different data streams, are $\sim 1\,\mathrm{Hz}$ or below [86].

Chapter 3

Event reconstruction in ICARUS

The study and reconstruction of collected events — neutrino interactions, but also cosmic rays and potentially signals of BSM physics — relies on data recorded by TPC, PMT, CRT subsystems. The TPC system identifies and creates 3D track (or shower) objects, using topological and calorimetric criteria to determine particle characteristics. The PMT system uses scintillation light for event triggering, precise event timing measurement and interaction position localization within the detector. Lastly, the CRT system filters out cosmic rays, vetoing those which are in coincidence with the neutrino spill, distinguishing between incoming and outgoing particles, and tagging any activity occurring outside the beam spill associated with the event.

3.1 Data processing chain

ICARUS design and acquisition parameters lead to a substantial data rate and volume. In order to deal with it, several strategies have been introduced in the ICARUS data processing chain. As already described in subsection 2.2.1, TPC wire signals are digitized by 12 bit ADC with 2 bytes/sample at a 2.5 MHz sampling frequency. This spans over a ~ 1.6 ms time window to record activity before and after the event of interest, corresponding to 4096 samples. Accounting for the 53248 wires of the TPC, it would correspond to $\sim 400\,\mathrm{MB/event}$ just from TPC raw data. The bulk of the data comes from the four TPCs, which represents the $\sim 90\%$ of the total event size. Each event in ICARUS, after a hardware and software data compression, is $\sim 70\,\mathrm{MB}$. The output data consists of digitized waveforms from each TPC readout channel, representing the charge induced by the motion of ionization electrons swept by the drift field from the TPC volume. Similarly, the output data from the PMTs consists of digitized waveforms giving the signals from detected scintillation photons.

LArSoft [91] is a toolkit that provides a software infrastructure and algorithms for the simulation, the reconstruction and the analysis of events, and it is common across different LArTPC experiments — which share the same physics in LAr — providing the architecture to interface to other packages to facilitate the evolution and improvement of the reconstruction algorithms.

All the collected raw data needs to undergo several software steps before it can be properly analysed: the reconstruction of these events is done in two stages. The first stage or "Stage0" translates from raw data format to LArSoft format for offline processing. It also performs signal processing for all three subsystems with the goal of identifying physical signals "Hits" to be fed to the pattern recognition and event reconstruction algorithms.

For example, the StageO processing for TPC includes the following information:

- decoding, which decompresses and unpacks raw data into a format that can be used in later steps, including electronic noise filtering to remove TPC coherent noise;
- deconvolution, which removes the effect of the electrostatic field around the wires and the electronic response;
- region of interest (ROI) finding, which reduces data volume by selection of ROI around candidate signal;
- hit finding, which builds Hit objects from the ROIs in the previous step. A Hit represents the identified signal induced by a charged particle on a wire and is the primary input to the pattern recognition algorithms.

The output of StageO is about ten times smaller than the input raw data, as full waveforms are dropped, and will be the input for the next stage. The "Stage1" processing is mainly focused on the reconstruction of TPC, CRT and PMT signals, and might include calibrations of each subsystem. For example, the Stage1 processing for TPC includes the following information:

- hit filter, which builds 3D points from combination of 2D Hits across different wire planes;
- pattern recognition algorithm, which arranges close hits into clusters that are then used to identify track or shower candidates and event topology information, including cosmic ray identification. Inside each defined interaction, the so-called *slices*, a hierarchy among all reconstructed objects is build to identify parent-daughter relationships;
- track fit, which applies detailed algorithms to reconstruct tracks and showers and obtain calorimetric measurements of each particle, and provides information to allow kinematical reconstruction and to analyze the event;
- information from the Multiple Coulomb Scattering algorithms, as explained in Chapter 4.

The output of Stage1 includes Calibration Ntuples for calibration and detector studies, and allows to produce "Common Analysis Framework" or CAF files for event selection and analysis. A brief outline on CRT and PMT reconstruction follows, while the TPC reconstruction will be examined in detail in the next subsection.

Optical reconstruction

The "optical reconstruction" [41] aims at identifying the scintillation light activity in simulated or recorded PMT waveforms and building clusters of fired PMTs to be matched in time and

spatially with events in the TPC and hits on the CRT. The information on the reconstructed signals or "optical hits" for each PMT is stored in OpHit objects, where the time is defined as the point at which the signal crosses the threshold. The optical reconstruction then looks for spatial and time coincidences within a 40 ns window between the event OpHit and clusters them into "optical flashes". The time of the optical flash is extrapolated from the distribution of OpHit times referring to the bin with the largest number of integrated PEs. After an optical flash is produced, there is a 1 µs dead time before another interaction can be detected. Ideally, all the light gathered by an optical flash should be produced by the same neutrino or cosmic ray interaction inside the TPC, localized in the longitudinal-vertical plane with the light barycenter and with a time given by the reconstructed flash, from which the drift coordinate of wire hits can be reconstructed.

CRT reconstruction

The CRT reconstruction [41] starts from CRT data fragments, formatting the raw data from each Front End Board (FEB) in terms of Hits. The CRT hits are reconstructed inside a single CRT module and later shifted to the coordinate system of the detector, by selecting channels with the highest PEs yield and using a coincidence logic specific to each CRT sub-system. The spatial resolution for the CRT hits depends on the sub-system and on the region of the CRT. Each CRT hit is associated with a timestamp, and timing calibrations and delay corrections are performed for example to account for the light propagation inside the plastic scintillator slabs from the hit position to the SiPM readout.

3.1.1 Calibration Ntuples

At the end of Stage1, events are ultimately reconstructed and output into ROOT TTree files suitable as input to analysis and two different formats of files are produced from the Stage1 output. The analysis performed in this thesis has been carried out using only one of this format, the so called Calibration Ntuples, which are ROOT files containing useful information from the detector reconstruction, for all the subsystems.

Calibration Ntuples were envisioned as the main input for all types of calibration studies and contain only certain tracks from the reconstruction, those tracks with a defined t_0 which are crossing-cathode tracks, as described in subsection 3.2.3. The TTree that deals with all the available information contains an entry for each reconstructed track with track-level and hit-level information — and for simulated Monte Carlo events with truth-level information as well. Hit-level variables are stored for each plane and contain information about all the Hits on each track, allowing an in-depth study of TPC events. Moreover, some information not originally included, such as the momentum calculated using the MCS algorithms described in Chapter 4 and the momentum calculated from range as described in Subsection 3.3.3, has been added.

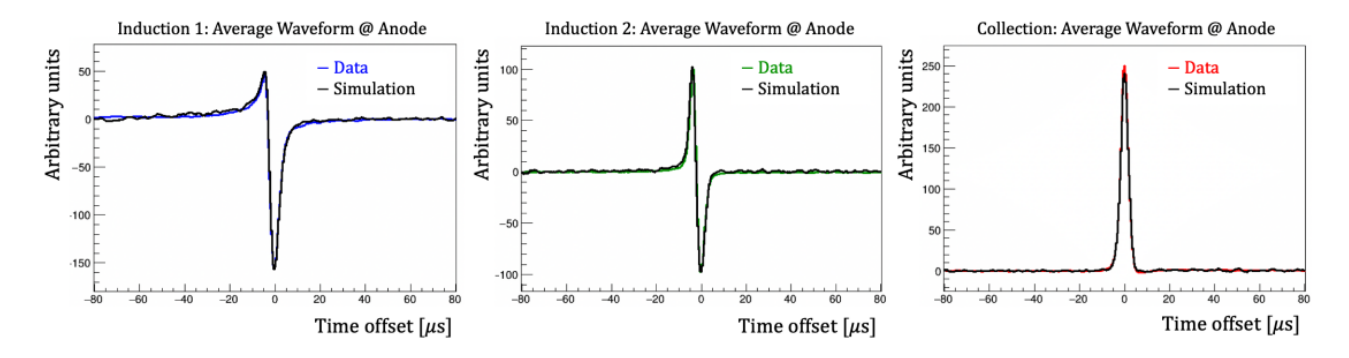


Figure 3.1: Measured signal shape at the anode plane averaged across one TPCs. Data and simulated responses are reported for the three wire planes, showing the characteristic unipolar and bipolar shape. Taken from [86].

3.2 TPC reconstruction

TPC reconstruction [86] begins as soon as the ionization electrons are detected and collected by the anode wire planes. Each wire in each plane of the detector records a waveform in ADC/tick units, where the amplitude of the signal is expressed in ADC while the tick corresponds to the t-sample of 0.4 µs in the ICARUS TPC sampling. As described in Section 2.2 the anode consists of 3 wire planes with specific bias voltages, so that ionization electrons pass between the Induction wires on their way to the Collection wires: while approaching the Induction planes, they generate a positive signal, whereas this change to a negative signal once they have crossed the plane and they move away from it. This bipolar signal is then converted into a unipolar signal at the end of the deconvolution process described in the next subsection, as shown in Figure 3.1.

3.2.1 Signal processing

The first step in the reconstruction consists in obtaining the distribution of ionization electrons arriving at the anode plane. The recorded signal depends not only on the ionization charge but also on a number of different factors: recombination, diffusion and attachment, field response, electronic response plus the additional contribution of the electronic noise. The resulting signal on the wires is therefore a convolution of these factors. These effects must be unfolded from the TPC waveforms to recover the desired information about the deposited charge per wire as a function of time. Specific noise filters are applied to remove the noise: for tracks travelling almost parallel to the wire planes, the noise filter can mistake the signal as part of the coherent noise and thus distort the waveforms from a group of channels. This effect is greatly reduced as the angle of the track increases with respect to the wire plane.

The ICARUS wire signal processing chain follows a logic similar to other LArTPC experiments, exploiting the deconvolution of the wire signal waveform. Ideally, after deconvolution, the signal pulse produced by a charged track on a wire would be gaussian-like (if no charge diffusion was present, the expected signal would be a delta function) with mean and integral determined by

the drift coordinate and ionization charge of the corresponding track segment. In that case, the area under the deconvolved waveform will be proportional to the number of deposited electrons.

The "deconvolution" is a technique applied to neutralize both the wire field and the electronic response: it is a mathematical procedure to extract the original signal S(t) from the measured signal M(t'). The measured signal M(t') is modeled as a convolution integral over the original ionization charge signal S(t) and the detector response function R(t,t') which gives the instantaneous portion of the measured signal at some time t' due to an element of the original signal at time t. This can be mathematically expressed as

$$M(t') = \int_{-\infty}^{+\infty} R(t, t') S(t) dt$$
(3.1)

The detector response function includes both the wire field and the electronics response: if it is time-invariant, then R(t,t') = R(t'-t) and we can solve Eq. (3.1) by performing a Fourier transformation, yielding $M(\omega) = R(\omega)S(\omega)$ where ω has units of rad s⁻¹.

The naive implementation of this approach suffers from high-frequency noise which is amplified by the deconvolution procedure (division of noise by the response function at high frequencies where the signal response is very small). Hence, the previous solution in the frequency space is extended through the introduction of a low-pass filter function $F(\omega)$ as

$$S(\omega) = \frac{M(\omega)}{R(\omega)F(\omega)} \tag{3.2}$$

which is essentially equivalent to replacing the real detector response function with an effective response function. The original signal can therefore be retrieved by applying the inverse Fourier transform to $S(\omega)$.

This deconvolution technique is known as "one dimensional deconvolution" or 1D deconvolution, in the sense that a Fast Fourier transform is carried out as a function of time only. Therefore, this procedure assumes the induced current on each sense wire is independent of the charge distribution in its vicinity. However, as described in [92, 93], the induced current on the sense wire receives contributions not only from ionization charge passing by the sense wire, but also from ionization charge drifting in nearby wire regions at roughly the same time. As long as these contributions are generally small they can produce destructive interference particularly on the Induction planes and for isochronous tracks. To take into account charge over nearby effects, a 2D deconvolution involving both the time and the wire direction is in preparation, as already introduced in MicroBooNE [92]. Currently ICARUS uses a 1D deconvolution technique, but it is finishing some validation tests to transition to 2D.

This difference between Induction and Collection planes makes the 1D deconvolution technique successful for the Collection plane but not quite optimal for Induction planes. Compared to the Collection plane, the Induction planes suffer from wire response suppression at low frequencies due to its bipolar signal nature, which is problematic for the deconvolution procedure. Without

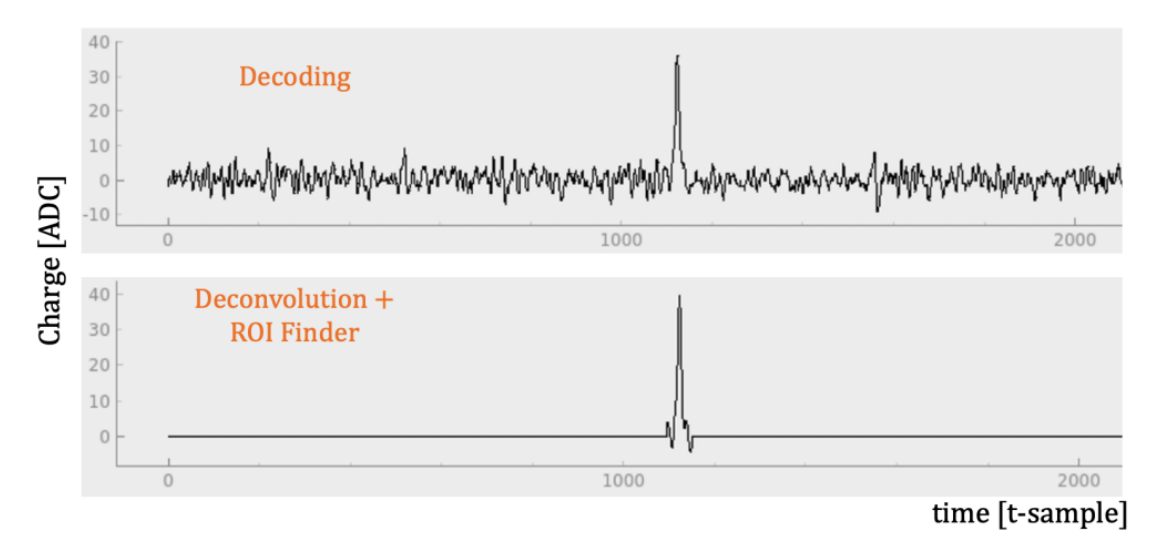


Figure 3.2: Collection plane waveform with signal processing. Top: example of measured waveform in collection plane. Bottom: Waveform after 1D deconvolution and selection of the region of interest (ROI). Note that a t-sample corresponds to 0.4 µs. Taken from [86].

mitigation, the amplification of the low frequency noise would lead to large uncertainties in the estimation of charge induced on the waveforms. This can be addressed considering only regions of interest (ROIs) in the time domain: the idea is to limit deconvolution to a small time window, slightly larger than the extent of the signal it contains, and reduce the event readout window to a set of ROIs, as shown in Figure 3.2, reducing the overall data size and speeding up the deconvolution process.

3.2.2 Hit finding procedure

The segments of waveforms left over after deconvolution are considered to have a high S/N ratio; however, they need to be further manipulated to provide meaningful physical information. A 2D Hit represents a cluster of electric charge arriving at a given wire at a given time and therefore is a point on the Reconstruction plane, defined by the drift direction and the normal to the wires on the wire plane. The reconstruction algorithms currently employed are based on finding Hits, over a certain threshold, on the deconvolved waveforms for each plane. Under the assumption that the output of the deconvolution process will be Gaussian-shaped charge deposits, the Hit Finder module is called Gaushit as it captures the waveform shape into a series of Gaussian distributions. Generally the module loops over the input ROIs from the deconvolved waveforms and handles each in two main steps: first it searches for candidate pulses with the idea that a ROI can contain more than one hit and secondly, it fits these candidates to a Gaussian shape. When the hit shape is not a simple Gaussian but multiple charge pulses are seen by the same wire in a short time, the pulse is divided into a certain number of hits under the assumption that the entire pulse can be described accurately with overlapping Gaussian peaks. The number of Gaussians used to fit the pulse is often called *multiplicity*. The extracted properties of the hits are then the parameters of the Gaussian fit: the area represents the total charge, with the

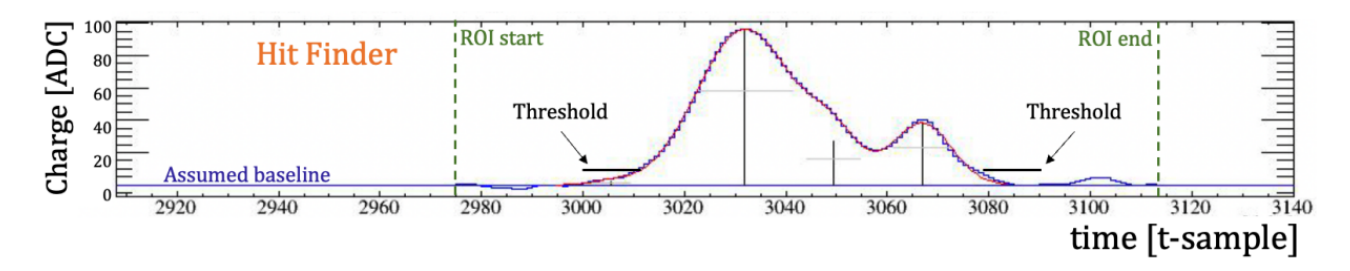


Figure 3.3: Collection plane waveform showing the Hit Finder algorithm performance. Gaussian fit is carried out each time a certain threshold is exceeded. In this example the Hit Finder chooses to fit the hit with three Gaussian shapes (red line), the crosses represent the center of the fit peaks, the pulse heights above the baseline and their fit widths. Taken from [86].

appropriate calibration constant to convert ADC×t-sample to coulomb; the mean gives the hit peak time; the amplitude represents the hit height; the width corresponds to the hit RMS.

Figure 3.3 shows an illustration of the Hit Finder algorithm. A collection of 2D hits for each wire plane has been created, representing a signal detected on a specific wire at a specific time. These three 2D views are used as the input to pattern recognition algorithms, in order to create all possible space points with the goal of maximizing efficiency at the possible expense of purity. The collection of 2D hits used to create space points is taken as input to the pattern recognition algorithm. Candidate 3D points are found by performing combinations of 2D hits in neighboring planes using an algorithm that combines compatible hits, which means that the difference in the peak times of the Gaussian pulses should be within a predefined interval and that their wires also need to intersect in the yz projection. Once a pair of compatible signals has been identified, a 3D candidate space point can be formed using both 2D hit information.

High levels of noise might cause the creation of hits due to non physical signals or the loss of real signal, and these will cause problems in the pattern recognition performance, yielding poorly reconstructed track and shower candidates or very long reconstruction times. In order to solve this problem, one can exploit the fact that physical hits are expected to have correlated matches across the three planes; conversely, pure noise hits will be mostly uncorrelated and will not have matches on the other planes. In addition, the horizontal wires on the first Induction plane are split into two 9 m long wires at z=0 m; this might produce ambiguous hit combinations and could also benefit from the triple coincidence.

Thus, taking advantage that the x coordinate is common to all three views for correlated hits, a search is done to the third plane to look for a compatible hit with the preliminary extracted 3D position. If a compatible hit is found, a 3D space point is formed and saved. It is clear that creating space points is critically dependent on the 2D hit finding efficiency and purity, which ultimately relies on the whole signal processing chain. The requirement of having a triple match will introduce inefficiencies if a set of hits is missing in one plane, and an alternative could be to rely on hits with matches on just two planes, to recover some signal. However, there might be a non negligible number of combinations satisfying the time overlap criteria and creating an abundant number of space-points if all of them are used.

3.2.3 Pandora Pattern Recognition

Pattern recognition refers to the identification of structures or regularities in data. The *Pandora* software development kit [94] aims to address the problem of identifying energy deposits from individual particles using a multi-algorithm approach. Each algorithm is designed to address a specific aspect of event reconstruction, and collectively provide robust and sophisticated patter recognition. The final goal is reconstruct each particle — and each shower — as a single object particle — or shower — that is both pure (containing only hits from that particle) and complete (containing all hits from that particle).

As previously mentioned, the input to Pandora is a list of unambiguously reconstructed 2D hits, alongside detector information (detector geometry and unresponsive or dead wire regions), to which the pattern recognition chain is applied. The Pandora output is a list of reconstructed 3D particles, named Particle Flow Particles or PFP. Each PFP corresponds to a distinct track or shower in the event, and has associated objects such as collections of 2D hits for each view (Clusters), 3D positions (SpacePoints) and a reconstructed vertex position, that defines its interaction point or its first energy deposit. PFPs are identified as track-like or as shower-like based on their topological features, and are then placed in a hierarchy which identifies parent-daughter relationships and describes the particle flow in the observed interactions. Track and Shower objects carry additional information, such as position and momentum values for tracks or principal-axis information for showers.

Reconstruction chain

The current chain of Pandora algorithms has largely been tuned for neutrino interactions from BNB, however the algorithms are designed to be generic and easily reusable for other experiments. Pandora has two main chain algorithms for event reconstruction in neutrino detectors, PandoraCosmic and PandoraNu, targeting the reconstruction of interactions under cosmic ray and neutrino hypothesis, respectively. The algorithm selection results in the following features:

- PandoraCosmic focus on strongly track-oriented reconstruction, producing primary particles that represent cosmic ray muons. Showers are assumed to be δ rays and are added as daughter particles of the most appropriate cosmic ray muon. The reconstructed start point for a cosmic muon is chosen to be the highest vertical coordinate of the muon track.
- PandoraNu focus instead on identification of a neutrino interaction vertex, which becomes the pivot to reconstruct all particles emerging from it. Vertex identification algorithms are PandoraNu specific and there is a more sophisticated treatment of track and electromagnetic showers. The chain concludes building a hierarchy, where a parent neutrino particle is created and the reconstructed visible particles are added as daughters of the neutrino.

Each chain works well on the type of interactions it was designed for. Surface detectors need to deal with events both containing neutrino and cosmic rays interactions. In order to optimize

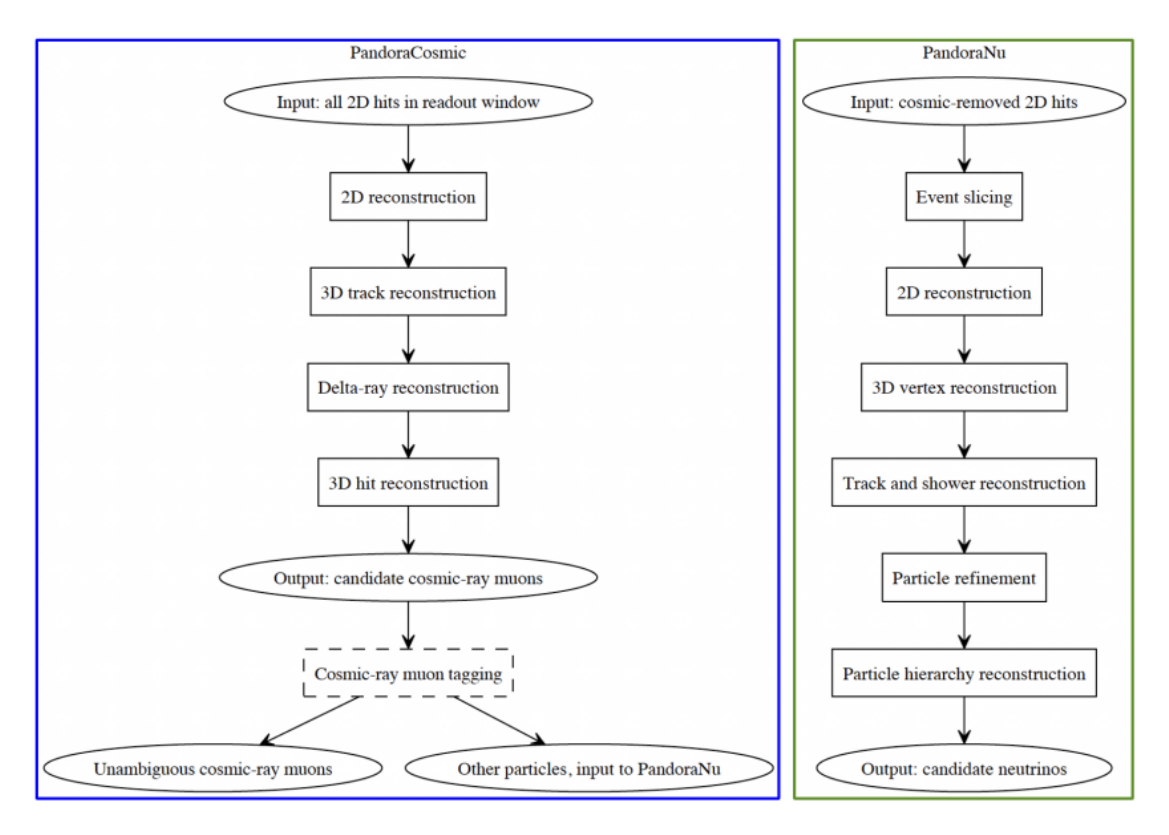


Figure 3.4: Outline of the Pandora consolidated reconstruction used in ICARUS. Particles output by the *PandoraCosmic* are examined by an external module to tag and reject clear cosmic interactions. 2D hits unambiguously associated to a cosmic ray muon are removed from the initial hit collection and generate the new input to the *PandoraNu* chain algorithm. Taken from [95].

the pattern recognition performance, a consolidated reconstruction approach is often adopted. A flow diagram illustrating this approach is shown in Figure 5.8. This starts by running the *PandoraCosmic* reconstruction on the collection of identified hits during the readout window.

PandoraCosmic

First a 2D clustering of hits is performed for each read-out plane independently, producing a list of clusters which represent continuous and unambiguous lines of hits. The aim of the 3D track reconstruction stage is to identify consistent groups of 2D clusters from the three readout planes that describe a single track-like particle. A dedicated algorithm considers the suitability of all combinations of clusters from the three readout planes and stores the results for further analysis. Following the 3D track reconstruction, the Delta-ray reconstruction step dissolves any 2D clusters that have not been included in a reconstructed object, under the assumption that these are likely to be fragments of delta-ray showers, which are used to seed and grow shower particles. At this point, 2D hits have been assigned to different particles containing clusters from one, two or usually three readout planes and new 3D hits, called space points, are created.

PandoraCosmic last task is finding the start position of the cosmic ray muon at their highest reconstructed vertical coordinate, as they are assumed to always be downward going. Secondary shower particles are joined to the parent muon track through a hierarchical parent-daughter dependency, representing Michel electrons and δ rays. Before applying the PandoraNu chain, a stitching algorithm is performed to fully reconstruct particles crossing neighbouring drift volumes. In addition, a cosmic ray tagging filter is applied to distinguish hits unambiguously associated with cosmic ray muons from the remaining ambiguous hits. Unambiguous cosmic-ray associated hits are removed from the input hit collection that was first given to PandoraCosmic, providing a new cosmic-removed hit collection that will serve as the initial point for PandoraNu.

Track timing

The drift coordinate is computed only from temporal information, as seen in Equation (2.1). Hence, a precise and robust assignation of the interaction time to each reconstructed object inside the TPC is crucial to correctly locate the interaction position along the drift coordinate. The time t at which the charge was collected on the wires is a function of the time t_0 at which the particle entered the detector, relative to the global trigger time, and the distance x in the drift coordinate from the anode plane where the energy was deposited:

$$t = t_0 + \frac{x}{v_{\text{drift}}} \tag{3.3}$$

It is straightforward to see that there is an ambiguity in this equation between t_0 and x for a given t unless t_0 is known. The track time can be accurately measured with the PMTs if an optical flash is matched to a reconstructed object in the TPC, exploiting the so-called "PMT-TPC matching". In spite of this, the high number of cosmic tracks crossing each TPC during the readout window makes it challenging to unambiguously assign a unique t_0 to each track. For in-time interactions $t_0 = 0$ by definition and no ambiguity arises. In all other cases, the t_0 is initially unknown and Pandora reconstruction assumes, by default, that the track arrived at the trigger time; hence assigning a preliminary value of $t_0 = 0$. For this reason, the exact position in the drift coordinate where the charge was physically deposited is only well determined for in-time interactions. For out-of-time particles, the intrinsic ambiguity in x makes it impossible to distinguish between the charge deposited by a particle arriving before the trigger time, but far from the anode plane, and the charge deposition happened after the trigger time, but much closer to the anode — the value of t would be the same in both cases.

Each cryostat of the T600 detector has two adjacent volumes separated by a central common cathode, which can be traversed by tracks. Light-independent methods can be implemented to measure the correct t_0 , taking advantage of the additional information provided by those tracks that have crossed the cathode plane. As previously seen, reconstruction initially processes each drift volume independently, resulting in separately reconstructed 3D objects in each volume. For tracks at $t_0 \neq 0$ and crossing the cathode, the reconstruction will, in general, produce two separate segments characterized by the same displacement from the cathode. However, these will be shifted in opposite directions as the drift field direction alternates between adjacent TPCs. This distance will be proportional to the real track time t_0 and inversely proportional to the

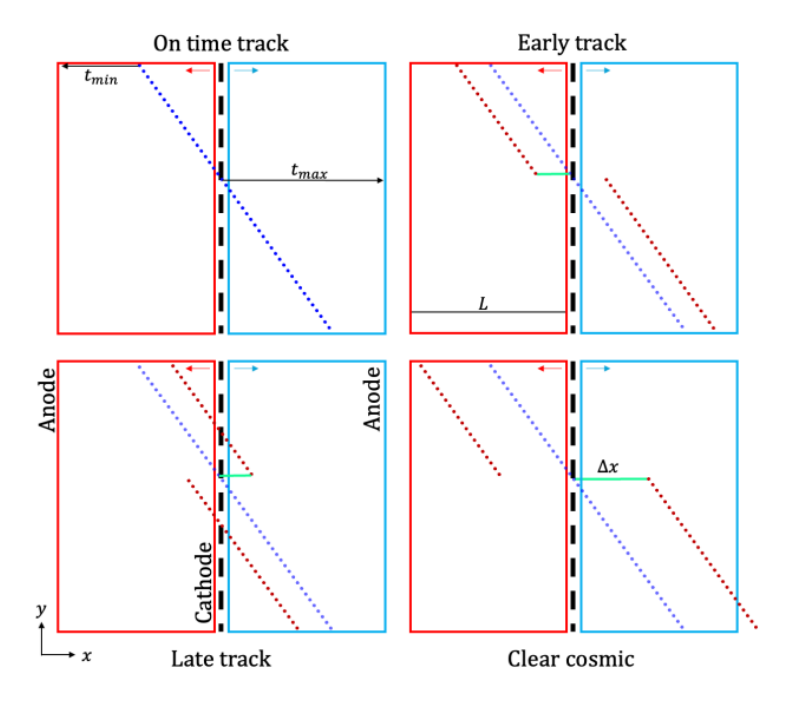


Figure 3.5: Example of possible situations for a cosmic ray crossing the detector from top to bottom and passing through the cathode. Blue dots represent the true trajectory of the cosmic, while red segments are the reconstructed Pandora tracks under the initial assumption of $t_0 = 0$. Some of the key variables for performing the stitching between the split tracks are also shown. Red and blue arrows indicate the drift field direction in each TPC. Taken from [86].

drift velocity $v_{\rm drift}$. The direction of the shift depends on weather the physical track occurred before or after the trigger time, called early tracks and late tracks respectively. In Fig. 3.5 there is a graphical representation of all the three possible situations. This characteristic geometry is exploited by Pandora to search for two 3D clusters that are reconstructed in two different drift volumes and are consistent with creating a single continuous trajectory both in its position and direction across the cathode boundary. If such a match is found, the separate components can be stitched together by shifting the two clusters to the x coordinate of the cathode plane. The t_0 corrections identified by this stitching process allow to estimate the track time as

$$t_0 = t_{\text{max}} - \frac{L - \Delta x}{v_{\text{drift}}} \tag{3.4}$$

with $t_{\rm max}$ the time of the closest hit to the cathode, L the maximum drift length and Δx the distance between the cathode and x position of the hit with $t_{\rm max}$ before any correction. ICARUS have $L=1.5\,\mathrm{m}$ and $v_{\rm drift}\simeq 1.6\,\mathrm{mm\,\mu s^{-1}}$ at the nominal electric drift field $E_{\rm drift}=500\,\mathrm{V\,cm^{-1}}$. During the stitching procedure, a tolerance factor in the shifts between the two tracks segments was introduced to account for possible asymmetries due to space charge effects or inefficiencies during the track reconstruction. Taking into account the TPC readout characteristics, a track would be fully visible only if both the time of the first and last hit are inside the delimited time window. A total of 4096 t-samples are recorded, with t-samples $=0.4\,\mathrm{\mu s}$, of which ~ 850 are recorded before the trigger. Therefore, the first hit should be recorded no earlier than $\sim 340\,\mathrm{\mu s}$ before the trigger time, and the last hit no later than $\sim 1300\,\mathrm{\mu s}$.

Once the stitching algorithm is done, a clear cosmic ray candidate is identified if it satisfies at least one of the following criteria:

- the reconstructed particle crosses the top and bottom boundaries of the detector;
- any hit in the reconstructed particle, assuming $t_0 = 0$, fall outside of the physical drift volume, clearly indicating that the object is not compatible with the beam spill gate (see the last diagram of Fig. 3.5);
- the t_0 correction found during the stitching algorithm is too large to be compatible with a particle coming from the beam.

The reconstructed particle hierarchies tagged as clear cosmic ray muons are the first output of consolidated reconstruction and their hits are removed from the record before the reconstruction chain continues to further process the data, easing neutrino-induced particle reconstruction.

PandoraNu

The PandoraNu reconstruction path runs the previously described algorithms up to the 3D hit creation, in order to avoid any possible inefficiencies during the *PandoraCosmic* chain. The 3D hits are divided into slices and each slice is processed through dedicated neutrino reconstruction algorithms, resulting in one neutrino candidate. The first step of PandoraNu utilizes the track oriented clustering and topological association, where now the algorithms need to handle more complex topologies. The list of 2D clusters for the different readout planes are used to produce a list of possible 3D vertex candidates, and once they are all identified, it is necessary to select one as the most likely neutrino interaction vertex. All the candidates must pass a quality cut before being accepted as a valid vertex: they are required to be located on or near a hit in all three views. Primary particles produced in the interaction should point back towards the true interaction vertex, hence candidates are disadvantaged if the sum of the transverse energy over all cluster is not compensated. Downstream secondary particles might cause some imbalance, however they are expected to be less energetic and thus of minor impact. Moreover, true vertex are expected to have a large asymmetry between the number of upstream and downstream hits, and symmetric candidates are severely penalized. The last input comes from the knowledge of the beam direction, benefiting candidates with low z positions (remind that the beam direction is along the positive z axis). When the candidate is chosen, any 2D cluster crossing the vertex is split into two pieces and a new cluster on either side of the projected vertex position is created.

Next step is 3D track reconstruction which proceeds almost exactly as in *PandoraCosmic*. The only difference is that now *PandoraNu* also attempts to reconstruct primary electromagnetic showers from electrons and photons, by adding branches to any long cluster that may represent the central structure of a shower. The obtained 2D shower-like clusters are matched between readout planes to form 3D shower particles, reusing the ideas from the 3D track reconstruction. The final output from the reconstruction chain is a single reconstructed neutrino particle for each slice with internal particle hierarchy, which provides the flow of the neutrino interaction.

3.3 Energy reconstruction

Precision calorimetry measurements are one of the key reasons LArTPC detectors were proposed for neutrino experiments. As already described in subsection 2.1.3, as charged particles traverse liquid Argon, they deposit energy through ionization and scintillation. Measuring this energy deposition is crucial because it not only provides information about the particle's energy but also helps identify its species.

Neutrinos themselves are not electrically charged and thus leave no ionization trace. However, their interaction products often do, enabling the identification of the original neutrino flavor. The energy loss of charged particles traveling through a material can be described as the sum of energy lost due to interactions with the material's electrons and energy dissipated through radiative processes. In the kinematic regime relevant to ICARUS, muons and protons primarily lose energy via ionization. The mean energy loss is accurately described by the Bethe equation, along with its corrections [96]:

$$\left\langle \frac{\mathrm{d}E}{\mathrm{d}x} \right\rangle = \zeta T_{\mathrm{max}} \left[\ln \frac{2m_e c^2 \beta^2 \gamma^2 T_{\mathrm{max}}}{I_0^2} - 2\beta^2 - \delta(\beta\gamma) \right]$$
(3.5)

where ζ encapsulates the scattering rate while T_{max} is the maximum energy transfer to a single electron, defined respectively as

$$\zeta = \frac{K}{2} z^2 \frac{Z}{A} \frac{1}{\beta^2 T_{\text{max}}} \qquad T_{\text{max}} = \frac{2m_e c^2 \beta^2 \gamma^2}{1 + 2\gamma m_e / M + (m_e / M)^2}$$
(3.6)

K is just a physical constant with units of MeV cm² mol⁻¹; z is the charge number of the incident particle in units of e (for muons and protons z=1) while Z is the charge number of the material (for Argon Z=18) and A is the mass number of the material, with units of $g \text{ mol}^{-1}$ (for Argon $A=39.948 \, \text{g mol}^{-1}$); m_e is the electron mass and M is the mass of the incident particle, both with units of MeV c^{-2} ; I_0 is the mean excitation energy with units of eV (for Argon $I_0=188 \, \text{eV}$); β and γ are given by the velocity of the incident particle; and finally $\delta(\beta\gamma)$ is a density effect correction to ionization energy loss.

Equation (3.5) is valid only in the region $0.1 \ll \beta \gamma \ll 1000$ with an accuracy of a few percent: at $\beta \gamma \sim 0.1$ the particle velocity is comparable to atomic electron velocity, and at $\beta \gamma \sim 1000$ radiative effects begin to become important. This equation describes the mass stopping power with units of MeV g⁻¹ cm²: defined in this way $\langle dE/dx \rangle$ is about the same for most materials, decreasing with Z. The linear stopping power is defined as $\rho \langle dE/dx \rangle$ with units of MeV cm⁻¹, where ρ is the density of the material – in this case liquid Argon – with units of g cm⁻³.

At $\beta\gamma \sim 3$ the stopping power function has a minimum known as minimum ionizing region, and a particle with an energy close to this region is said to be a minimum ionizing particle or MIP. As visible in Figure 3.6 the variation of the stopping power from $\beta\gamma \sim 3$ to $\beta\gamma \sim 100$ is rather small, allowing to assume a MIP-like behaviour between these two values: for these reasons, in

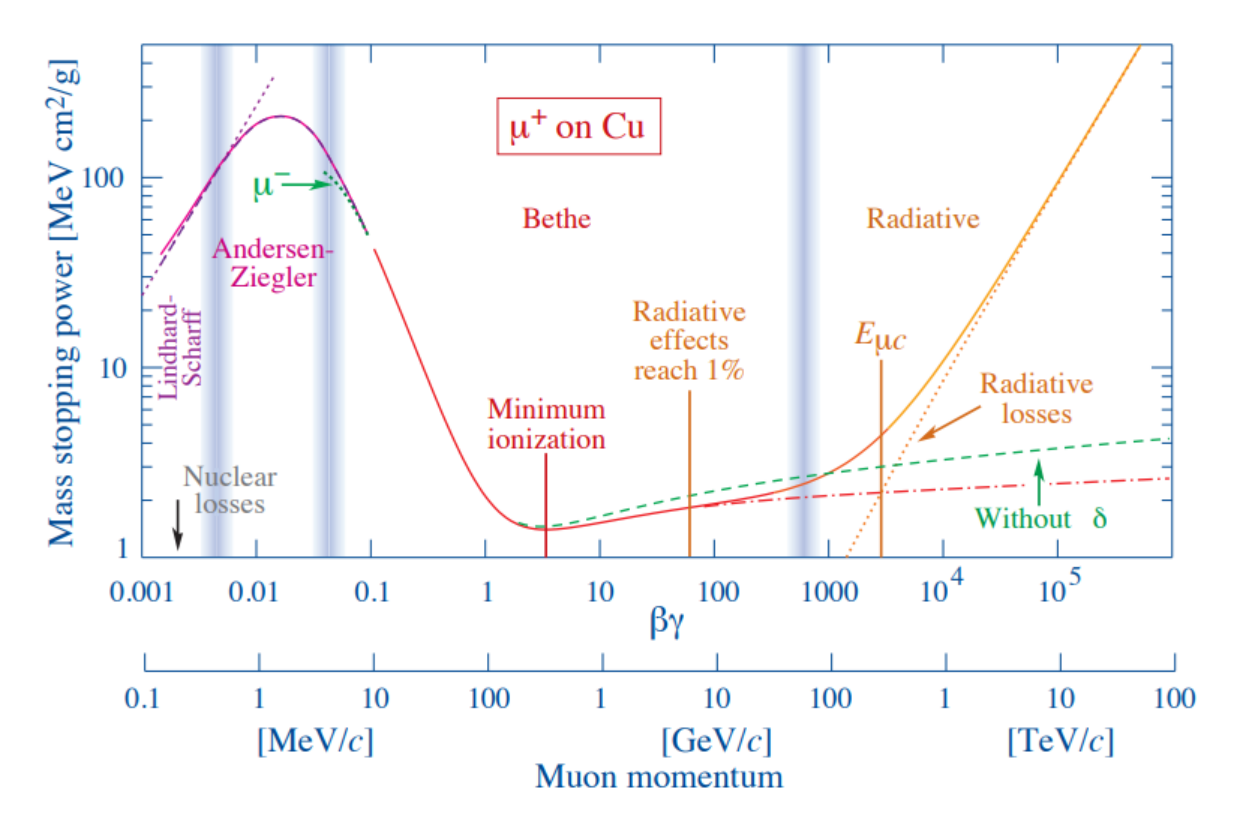


Figure 3.6: Mean rate of energy loss for μ^+ in copper as a function of $\beta\gamma$ and kinetic energy. The solid curves indicate the total stopping power. Although the figure describes the energy loss of muons in copper, it is qualitatively identical for other target materials such as liquid Argon. Taken from [96].

practical cases, we can consider most relativistic particles such as cosmic muons as MIPs.

Going from $\beta\gamma \sim 3$ towards lower kinetic energies, the $\langle dE/dx \rangle$ shape presents a sharp rise known as Bragg~peak, indicating an increase in energy deposition, i.e. ionization, towards the end of the track. This ionization rise is characteristic of each type of particle, providing thus a good method to discriminate between species.

The description of charged particle energy loss is complicated by the presence of δ rays. These are secondary electrons to which a significant amount of energy is transferred by the ionizing particle, allowing them to produce further ionization along the primary track trajectory, and this produces a long tail on the distribution of particle energy loss, significantly perturbing the measurement of the mean energy loss. To overcome this problem, the most probable value (MPV) of the energy loss distribution, rather than its mean, is used, as the MPV only depends on the peak of the distribution. Due to the typical deposited energy intervals and the precise sampling of calorimetric information in ICARUS, it is possible to achieve a good measurement of the energy loss distribution. In the *Landau limit*, which is applicable to energy depositions far from the stopping point of a particle, the corresponding MPV is given by

$$\frac{\mathrm{d}E}{\mathrm{d}x}\Big|_{\mathrm{MPV}} = \left\langle \frac{\mathrm{d}E}{\mathrm{d}x} \right\rangle + \zeta T_{\mathrm{max}} \left[\ln\left(\zeta x\right) + j + \beta^2 \right] \tag{3.7}$$

with j = 0.200 [97] and x the length of the track observed by a sense wire, with units of g cm⁻².

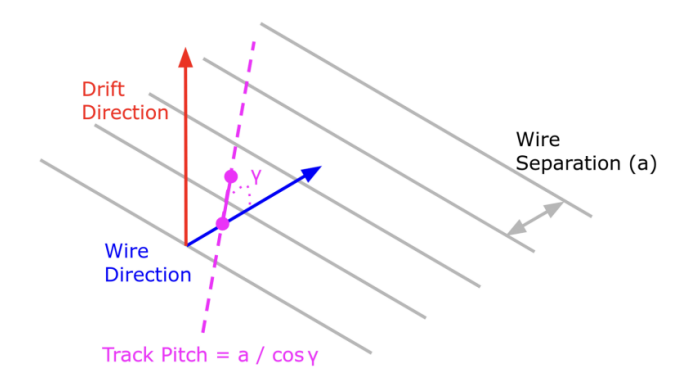


Figure 3.7: Sketch of the relevant directions and angle in the calorimetric reconstruction, showing the relation between the track orientation and the track pitch in a general LArTPC. Taken from [98].

3.3.1 Calorimetric reconstruction

The relevant quantities for the calorimetry are the Hit area, the Hit time coordinate and the track pitch length associated to the Hit wire, for all the Hits belonging to the track. The linear stopping power for track-like particles, that from now on will be indicated as dE/dx with units of MeV cm⁻¹, is calculated for each Hit separately from the dQ/dx with units of ADC cm⁻¹, which in turn is obtained as the ratio between the area under the hit dQ and the track pitch dx. The track pitch dx defines the 3D length of the track piece that generates signal on a single wire and is calculated from the direction of the track at the energy deposition as

$$dx = \frac{a}{\cos \gamma} \tag{3.8}$$

where $a=3\,\mathrm{mm}$ is the wire separation and γ is the 3D angle between the local direction of the track and the vector that connects adjacent wires, as shown in the sketch in Fig. 3.7; in general γ ranges from 0° to 90°. The track pitch dx in ICARUS is close to the 3 mm wire spacing for tracks parallel to the wire plane and increases for tracks at large angle from the wire plane.

Charge equalization

Calorimetry measurements require a good understanding of the charge response of the wires inside a LArTPC. The obtained dQ/dx might substantially differ from the original dQ/dx at the location where the ionization occurred: therefore, it needs to be corrected before the charge deposition is converted into the energy loss dE/dx for further studies. Several effects perturb the charge response in ICARUS, thus a charge equalization procedure with the goal of making the detector response to charge uniform in space and time was performed. The strategy adopted to equalize the charge response was separated in three steps: a first main equalization in the drift direction x, a second equalization in the wire plane directions yz, and a third TPC equalization.

Being at shallow depth, ICARUS has access to a huge number of cosmic muon tracks ideal to perform this type of detector calibrations. Cosmic muons are the standard candle for uniform

energy deposition throughout the detector, as they cross the detector as nearly MIPs; however, only the subset of muon tracks crossing the cathode was used, since cathode-crossing tracks are stitched by Pandora, enabling the identification of the track arrival time t_0 . This requirement comes from the need to know the proper time a particle crossed the detector, to apply a precise drift time correction. In ICARUS the dQ/dx is affected by:

• Argon impurities. When the ionization electrons drift towards the anode, they can be captured by electronegative impurities (primarily O₂ and H₂O) contained in the liquid Argon volume. The electron attachment is modeled as an exponential decay, hence the name of "electron lifetime"; this is inversely proportional to the concentration of impurities, and the measured dQ/dx can be corrected using the following formula

$$\frac{\mathrm{d}Q}{\mathrm{d}x}\Big|_{\mathrm{corrected}} = \frac{\mathrm{d}Q}{\mathrm{d}x}\Big|_{\mathrm{measured}} \exp\left(\frac{t_{\mathrm{hit}} - t_0}{\tau}\right)$$
 (3.9)

with $t_{\rm hit}$ the time at which the charge was collected and τ the measured drift electron lifetime. In ICARUS τ ranges from 3 ms to 8 ms which corresponds to a $\sim 5-15\%$ average charge signal attenuation across the full drift length;

- Drift field distortions. ICARUS experiences a large flux of cosmic rays, which means that a significant amount of ionization is produced in the detector per unit of time. Along with ionization electrons, Argon ions are also produced in the detector and slowly drift towards the cathode, remaining long enough to create significant electric field distortions [99]. In addition, the cathode plane is not perfectly flat. The last known distortion comes from the East TPC of the East cryostat, where a failure in the field cage induces a large but localized deflection to the drift field. Drift field distortions affect the charge scale in two ways, through the amount of charge recombining with Argon ions at the ionization point, and distorting the trajectory of the ionizing tracks;
- Induction plane transparency. As explained in section 2.2, each wire plane is biased at a different potential to guarantee transparency to the drift electrons in induction wires. It was found that the Induction planes, especially Induction-2, absorb charge in a position dependent way across the detector. The non full transparency affects all three planes; a reduced charge is seen by the Collection plane, while the signal shape in Induction planes are deformed, impacting the performance of signal processing and deconvolution;
- Gain variations. Charge signals are amplified and digitized by individual readout boards and gain variations across different readout boards create spatial variation in the amplitude of signals that need to be properly taken into account;
- Diffusion. Diffusion causes electrons to slightly spread apart, making the signal fuzzier as they travel, and the impact increases with the drift time. Diffusion can happen in both the longitudinal (drift) and the transverse direction, impacting the timing and transverse spatial resolution, respectively. Measurements have shown a percentage-level impact on dE/dx, leading to a bias in particle identification.

Drift direction equalization corrects the measured charge for effects that vary along drift path, with the largest impact coming from Argon impurities. Because the drift electron lifetime τ is not constant throughout the ICARUS data taking, this correction needs to be done on a run-by-run basis. Data acquisition runs in ICARUS last from a few hours to a few days, where this period is short enough to safely assume that the electron lifetime is constant.

To guarantee a uniform and non biased sample, this first step of the calibration was done using tracks crossing both the cathode and the anode planes. As known, cathode-crossing tracks are identified by asking a defined t_0 time of the track, while a cut on the drift direction length was imposed to ensure the track was also crossing the anode. The $\mathrm{d}Q/\mathrm{d}x$ distribution was fitted with a Landau convoluted with a Gaussian distribution to extract its most probable value. The Landau function models the physical $\mathrm{d}Q/\mathrm{d}x$ behaviour, while the Gaussian part accounts for all the smearing factors, such as electronic noise contribution to the signal, different inclination of the tracks or its wide range of energies. The collection of all MPVs as a function of the drift time is fit to an exponential to obtain an effective electron lifetime.

The second step is the wire plane equalization, which corrects charge reconstruction for detector effects that vary across the plane of the readout wires (vertical y and beam z directions). The procedure is similar to the drift direction equalization, but now the analysis is done in small area bins and the MPV obtained from the Landau \circledast Gaussian fit is used to compute a scale factor to keep the mean MPV fixed across the TPC. The scale factors need to be computed individually for each TPC in each wire plane, and also for each Run time period.

The third and final step is the equalization and measurement of the gains in the four TPCs. Instead of using through going muons as has been done until now, it is more appropriate to use stopping muons, since these will be used to measure the absolute gain equalization in ICARUS. In order to avoid non uniform distributions of energy loss, muons are only analyzed far from their stopping point. Distributions of broad dQ/dx after the first two equalizations are binned in terms of distance to the end point and as a function of drift time, and are once again fitted to a Landau \circledast Gaussian distribution. A single value is computed for each drift time averaging over distance, obtaining a final distribution of MPVs as a function of drift time for each TPC.

Energy calibration

The last step in the calorimetric reconstruction is energy calibration, which means calculating dE/dx from the previous corrected dQ/dx, which are related through [100]

$$\frac{\mathrm{d}E}{\mathrm{d}x} = \frac{W_{\mathrm{ion}}}{\mathcal{R} \cdot \mathcal{G}} \frac{\mathrm{d}Q}{\mathrm{d}x} \tag{3.10}$$

with $W_{\text{ion}} = 23.6 \,\text{eV}$ the amount of energy required to ionize an Argon atom, \mathcal{R} the fraction of electrons surviving the recombination, and \mathcal{G} the electronic gain that converts ADC in number of electrons and accounts for any perturbation induced by signal processing and charge corrections.

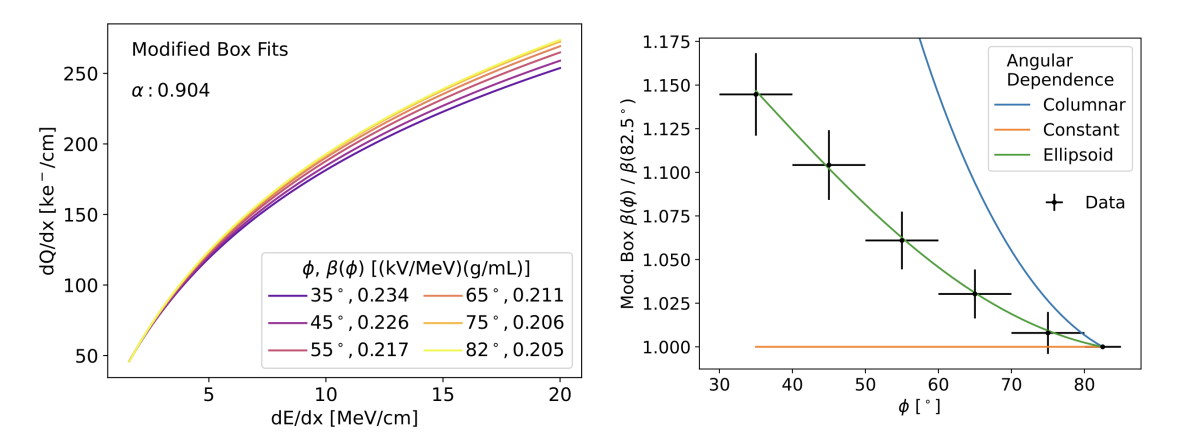


Figure 3.8: On the left, modified Box fits in each proton angle bin. On the right, the ratio of $\beta(\phi)$ measurements in the modified Box fit to the value in the $80^{\circ} < \phi < 85^{\circ}$ bin. This ratio is compared to three models of the angular dependence, as described in [102]. All three models are normalized to match the data in the $80^{\circ} < \phi < 85^{\circ}$ bin. Taken from [102].

Before reaching the anode plane, ionization electrons have the chance to recombine either with their parent atom or another ion in the ionization cloud. The fraction of electrons which recombine depends on the electric field strength and the amount of localized ionization. Therefore the recombination also depends on the dE/dx of the passing particle.

Several models exist to describe electron recombination, for instance the Birks law used at Gran Sasso [101] and the modified Box model proposed by ArgoNeuT [100]. After calibration studies in ICARUS, it was found that the ellipsoid modified Box (EMB) model has a good performance when fitting the data, with a parametrization that includes a dependence on the track angle ϕ to the drift electric field [102]:

$$\frac{\mathrm{d}Q}{\mathrm{d}x} = \frac{\mathcal{G}}{\mathcal{B}(\phi)W_{\mathrm{ion}}}\log\left(\alpha + \mathcal{B}(\phi)\frac{\mathrm{d}E}{\mathrm{d}x}\right) \quad \text{where } \mathcal{B}(\phi) = \frac{\beta_{90}}{\rho E_{\mathrm{drift}}}\left(\sqrt{\frac{\sin^2\phi + \cos^2\phi}{R^2}}\right)^{-1} \tag{3.11}$$

The ICARUS measurement of the EMB model is obtained by re-fitting the dQ/dx data and

$$\alpha = 0.904 \pm 0.008$$
 $\beta_{90} = 0.204 \pm 0.008 \text{kV MeV}^{-1} \,\text{g mL}^{-1}$ $R = 1.25 \pm 0.02$ (3.12)

The gain $\mathcal{G} = 75.0 \pm 1.1e^{-}\mathrm{ADC^{-1}}$ in the fit should be considered as an effective parameter, that encodes any perturbation induced by signal processing and charge corrections. A detailed review of these measurements can be found in [102]. Finally, the total energy deposition from a track-like particle is obtained by summing $\mathrm{d}E/\mathrm{d}x$ multiplied by the pitch at deposition point

$$E_{\text{total}} = \sum_{i}^{\text{all hits}} \frac{\mathrm{d}E}{\mathrm{d}x} \bigg|_{i} \mathrm{d}x_{i} \tag{3.13}$$

Besides this calorimetric approach, the energy of a track particle can also be computed from its range, as will be shown in subsection 3.3.2.

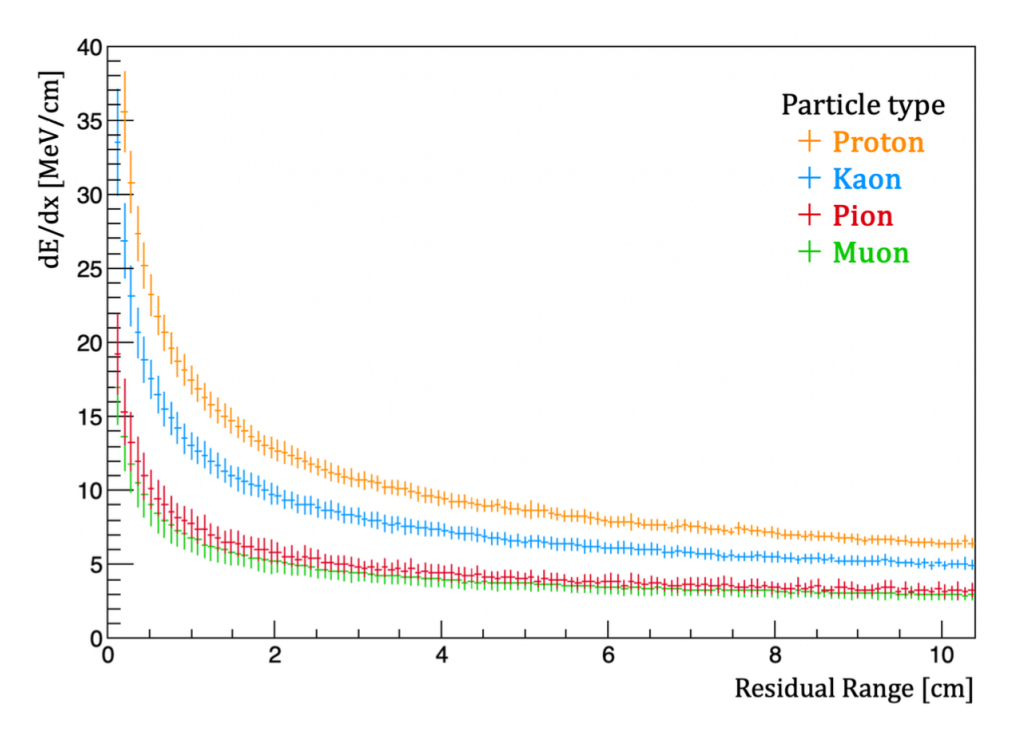


Figure 3.9: Theoretical distributions of the mean dE/dx values with respect to the residual ranges for different types of particles. The estimated resolution for each residual range bin is also shown as an error band. Taken from [86].

Particle identification

Typical particle identification methods condense both spatial and calorimetric information into a score used to distinguish different particle species. If the incident particle stops in the LArTPC active volume, the energy loss as a function of the residual range — defined as the distance of a given energy deposition, within the track it belongs to, from the endpoint of the track — is used as a powerful method for particle identification. All charged particles have an increasing stopping power at decreasing distance from the track end, and particles of different mass have different increasing stopping power: this separation is at most few centimeters before the end of the tracks between the typical particles involved (muons, protons, pions and kaons).

These theoretical profiles of dE/dx versus residual range, shown in Figure 3.9, are computed using the mean dE/dx from the Bethe formula, under the hypothesis of different particles. For each selected track, the reconstructed dE/dx per hit is computed and compared hit by hit to the theoretical mean of dE/dx. To extract a score between the measured response and a predicted particle hypothesis, the contribution of all hits on the selected track are summed, excluding the first and last hits of the track: this is due to the fact that residual range calculation for these two points might be wrong, since the exact position of the hit between the wires is unknown. ICARUS uses the last 25 cm to compute this score, or the full length if the track is shorter. It is important to notice that this procedure relies on the characteristic Bragg peak of each particle, thus if a particle scatters — instead of stopping — it does not produce the Bragg peak and the identification power is lost. This discrimination power is also reduced when the reconstruction fails to identify the entire track, losing some hits, especially at its end point.

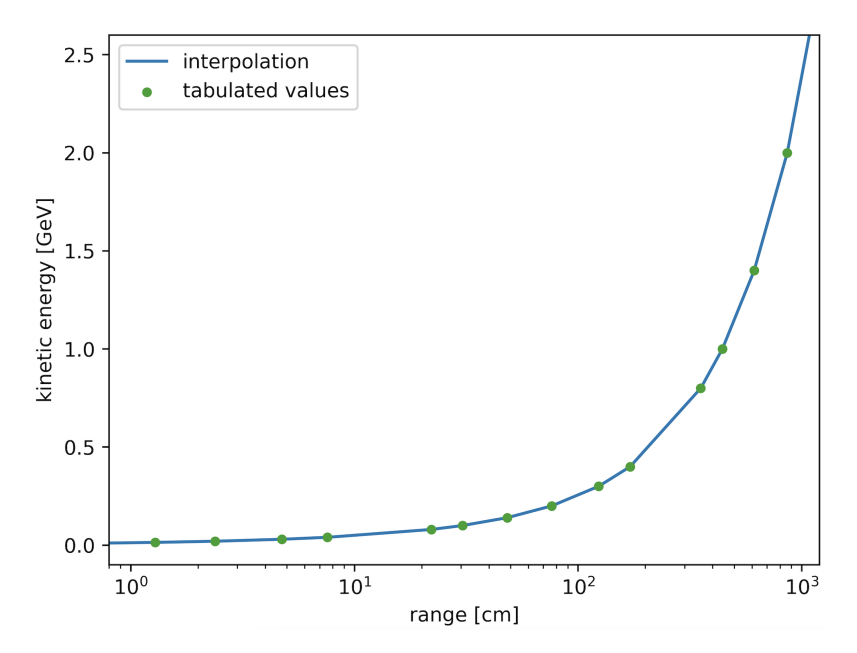


Figure 3.10: Plot of tabulated values of kinetic energy K and range R for a muon in liquid Argon, taken from [103]. The range has been converted from g cm⁻² to cm through the density $\rho_{\text{LAr}} = 1.396 \,\text{g cm}^{-3}$

3.3.2 Range-based reconstruction

Equation (3.5), which describes the mean energy loss, might be integrated to find the total - or partial - "continuous slowing-down approximation" (CSDA) range R for a particle that loses energy only through ionization and atomic excitation [103]

$$R(E) = \int_{E_0}^{E} \left(\frac{\mathrm{d}E'}{\mathrm{d}x}\right)^{-1} \mathrm{d}E' \tag{3.14}$$

where E_0 is small enough that the result is insensitive to its exact value. The CSDA range is a useful quantity since it relates the distance covered by a particle inside a material, such as liquid Argon, with its kinetic energy K or alternatively with its momentum p. Tables of stopping power contributions and CSDA ranges can be found in [103] for a selection of elements, for K ranging from 10 MeV to 100 TeV. Figure 3.10 shows the trend of K in function of the range R for a muon in liquid Argon: by knowing the range R, the kinetic energy K can be found with interpolation.

Since the range-based energy reconstruction is valid only if the muon stops inside the detector, it can be used only for contained muons. The kinetic energy can be converted into momentum as

$$p = \sqrt{E^2 - M^2} = \sqrt{(K+M)^2 - M^2} = \sqrt{K^2 + 2KM}$$
(3.15)

This range-based momentum or p_{range} will play a significant role in this thesis: the comparison between range-based momentum and momentum inferred from Multiple Coulomb Scattering for stopping particles such as cosmic muons, in fact, represents an excellent tool to estimate the goodness of the MCS algorithms, as will be widely described in Chapter 6.

3.4 Monte Carlo simulation

The event simulation in ICARUS is performed with LArSoft, a software suite for simulating, reconstructing, and analyzing events in LAr neutrino experiments: this is shared across all the SBN program, where each detector has a configurable geometry allowing detector-independent development at each stage of event processing. The simulation in LArSoft involves several steps.

First, particle fluxes are simulated to produce the expected distribution of desired species, such as cosmic rays, neutrinos, or individual particles like muons. These simulations are based on MC (Monte Carlo) generators, which use random numbers to sample from the expected interaction kinematics and the final state particles, according to cross-section models. Then, the generated particles are propagated to the detector, and their interactions with argon nuclei are simulated to predict the final state particles and their kinematics. The propagation of these particles and their secondaries through the different materials that make up the detector follows.

Note that neutrino simulation is different from the rest generated particles in terms of flux and cross section. External particles entering the detector and the products of a neutrino interaction share the same propagation and detection simulation phases. The final step, the one bringing the simulation to the same point as the collected raw data, is the detector simulation response in terms of the CRT, PMT and TPC signals. After this stage, the same reconstruction algorithms that were applied to the data, are used to process simulated events.

Cosmic Flux modelling

As a surface detector, accurately predicting the cosmic ray background in the detector volume is crucial. ICARUS uses CORSIKA to generate cosmogenic events, simulating air showers from high-energy cosmic particles based on magnetic field components for a given location. ICARUS uses the proton-only model, assuming only primary cosmic protons contribute to the Earth's cosmic ray flux. Cosmic primaries are sampled from a pregenerated CORSIKA library uniformly distributed over the cryostats, covering an extended surface of 12 m per side (total $\sim 1400 \,\mathrm{m}^2$). Only particles crossing the buffer box encapsulating the cryostats with some buffer around each side (3 m, 6 m and 5 m in the vertical, beam and drift directions) are considered. Each particle with kinetic energy $K \geq 50 \,\mathrm{MeV}$ is extrapolated back to a surface 20 m above the TPC center and fed into the MC simulation, propagating the particles and secondaries through the setup. More on the CORSIKA software can be found in [104].

Neutrino Flux modelling

SBN neutrino flux predictions are modeled using a data-driven MC, tuned to the BNB beam characteristics and external hadron-production measurements. The flux simulation starts with a detailed beam line geometry and a simulation of protons produced by the Linac. Interactions

between protons and the Beryllium target are modeled using GEANT4 [105] and tuned to external data to describe scattering processes. These interactions generate hadronic interactions in the target area, where the proton beam produces most secondary particles. All secondary particles, including scattered primary protons, are propagated using GEANT4 until they decay into neutrinos or are stopped, particularly at the beam dump. Neutrino trajectories are then extrapolated to the ICARUS detector to obtain the predicted neutrino fluxes and energy spectra.

Once the simulated neutrinos travel towards the detector, it is necessary to determine which of them will interact within the active volume of ICARUS to successively characterize the ν -Ar interactions. In ICARUS these are simulated using the GENIE10 event generator [106], which has been extensively used inside the neutrino experiment community. The result of this step of the simulation is a neutrino interaction in the ICARUS detector that produces a set of final state particles with their corresponding kinematics, creating a MCNeutrino object in LArSoft. These particles are input into the next step for particle propagation.

Particle Propagation simulation

This step relies on GEANT4 to fully simulate the chain of daughter particles resulting from the interaction with LAr, either of neutrino or cosmic origin. Each daughter particle is tracked when traversing the LAr and their energy deposits at each step recorded. The simulated geometry of detector is described by GDML files which include the full description of the detector and its surroundings such as the internal composition of the TPC, the cryostat, the field cage, the CRT and the experimental hall.

The energy deposition of each particle is then converted to ionization electrons and scintillation photons. Some electrons recombine, while the rest drift towards the wire planes. The ionization charge is further reduced by impurities in the LAr, parameterized as electron lifetime. Diffusion smearing can alter the arrival time or the detection location of electrons. A SimChannel object stores information about electrons deposited on a TPC readout channel, considering all detector effects, and connects them to the generated particle. A MIP loses about 2.12 MeV cm⁻¹ and creates electron-ion pairs with 23.6 eV and photons with 19.5 eV in LAr at $E_{\rm drift} = 500\,{\rm V\,cm^{-1}}$. Thousands of electrons and photons are tracked per cm of charged-particle track. Each photon undergoes Rayleigh scattering and reflections, eventually being absorbed by an optical detector or inactive surface. A full simulation with GEANT4 tracks every photon but is computationally expensive, thus a "fast" optical simulation uses a photon visibility library — which gives the probability of a scintillation photon to reach the optical detector, depending on its emission point — to maintain accuracy with reasonable computation time. Photons reaching the optical detector are reduced by a conversion efficiency, with ICARUS's PMT quantum efficiency measured at 12.1 \pm 1.0% [107]. The visibility decreases as position moves towards the cathode.

This photon library reads light from each energy deposition without tracking all photons and accounts for the scintillation light's time profile, dividing photons into a fast component with

 $\tau_{\rm fast} \simeq 6\,{\rm ns}$ and a slow component with $\tau_{\rm slow} \simeq 1.6\,{\rm \mu s}$, and also considers light propagation time. A SimPhoton object is then generated, containing information on photons reaching one optical detector channel. CRT panels are external to the TPC and require a special treatment, since simulated light and charge run only within the TPC volume. LArSoft supports auxiliary detectors included in the GDML geometry, extending GEANT4 simulation. GEANT4 determines positions and energy deposits in plastic scintillator stored in an AuxDetSimChannel object. The final output of particle propagation is a list of particles created by event generators (GENIE, Corsika) or detector simulation (GEANT4), with timing, trajectories, and energy deposits. SimChannel, SimPhotons, and AuxDetSimChannel objects are used to simulate the predicted detector signal.

Detector Response simulation

The simulation of the detector response must be properly addressed for each subsystem (TPC, PMTs and CRT), all interfaced with LArSoft. For the TPC, the ionization charge and arrival time at each wire (SimChannels) are used as input, and the charge arrival times are convoluted with the field response simulated via the GARFIELD program to obtain TPC wire waveforms [108]. The current field responses are calculated using a 1D simulation, but a 2D field response with a range of 10 wires on either side of a given wire is being implemented for better accuracy. The electronic response, modeling the shaping and amplification of the front-end electronics, and simulated noise follow. Finally, the waveform is quantized to mimic electronic digitization, producing an ADC waveform for event reconstruction.

For the Light Collection System, the number and timing of photons (SimPhotons) are used to build the simulated waveform at each PMT channel. The PMT simulation includes digitization of light signals, selecting photoelectrons arriving in a 2 ms window. Photoelectrons are binned in arrival time and the digitized single photoelectron response (SPR) is computed.

CRT detector simulation converts the deposited energy in scintillator strips (AuxDetSimChannel) into an analog SiPM signal. The light production in the scintillator follows an empirical model developed from measurements of the detector response, considering intrinsic light yield and attenuations. This signal is then injected into the readout simulation, reproducing the front-end electronics including gain, thresholds, charge resolution, time stamp generation, trigger logic. When a trigger occurs, the number of detected photoelectrons and a timestamp are output.

Finally, combining the outputs of the three subsystems allows running the same reconstruction algorithms as used for real data.

Chapter 4

MCS momentum reconstruction

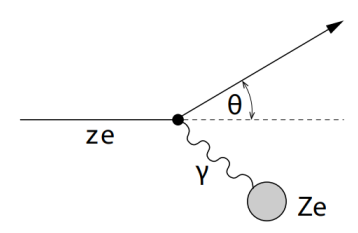


Figure 4.1: Schematic representation of a Rutherford scattering, between a particle with charge ze and the Coulomb field of a nucleus with charge Ze. Taken from [109].

A charged particles traveling through a medium is deflected by many small-angle scatterings because of the Coulomb scattering from nuclei [110]. We assume that nuclei are much more massive than incident particles, so that the energy transfer to the nuclei is negligible. Therefore the particle follows a random zigzag path as it crosses the material and the cumulative effect of these small-angle scatterings is a net deflection from the original particle direction. In general, the treatment of Coulomb scattering in matter can be schematically categorized into three cases:

• Single scattering. If the absorber is very thin, such that the probability of more than one Coulomb scattering is small, the angular distribution is given by the Rutherford formula

$$\frac{\mathrm{d}\sigma}{\mathrm{d}\Omega}\Big|_{\text{Rutherford}} = \frac{z^2 Z^2 \alpha^2}{\beta^2 p^2} \frac{1}{4 \sin^4(\theta/2)} \tag{4.1}$$

with z and Z the charge of the scattered particle and the nucleus, respectively; $\beta = v/c$ and p the velocity and the momentum of the scattered particle; and θ the scattering angle. A schematic of Rutherford scattering is given in Figure 4.1.

- Plural scattering. If the average number of scatterings is more than one but still very small (N < 20) then neither the Rutherford formula nor statistical methods can be applied and this is the most complicated case to treat [111].
- Multiple scattering. If the average number of scatterings is greater than 20 and the energy loss is small or negligible, the problem can be treated statistically to obtain a probability distribution for the net deflection angle; this is the most common case encountered.

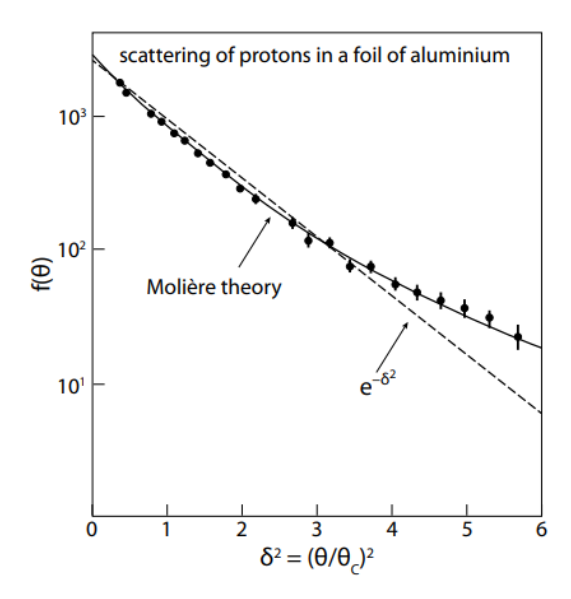


Figure 4.2: Distribution of the scattering angle of protons with kinetic energy $E_{\rm kin}=2.18\,{\rm MeV}$ having traversed an aluminium foil with area mass density of $x=3.42\times 10^{-3}\,{\rm g\,cm^{-2}}$. The measurements are compared with the exact Molière theory and also with a Gaussian. In this logarithmic representation plotted against the squared scattering angle the Gauss distribution is a straight line. The scattering angle is normalised here to the characteristic angle θ_C appearing in the Molière theory ($\theta_C=\chi_C\sqrt{B}$) with parameters χ_C and B as given in [112]. Therefore with $\delta=\theta/\theta_C$ the leading dependence of the Molière distribution at small angles is proportional to $\exp\left(-\delta^2\right)$. Taken from [109].

4.1 Multiple Coulomb scattering

Given the predominantly small momentum transfer, Coulomb scattering is a coherent scattering process off the total charge of the nucleus resulting in a quadratic Z-dependence. For a not too thin layer of scattering medium, in such a way that the average number of scatterings exceeds 20, we speak of multiple Coulomb scattering or *Molière scattering*.

In general, rigorous calculations of multiple scattering are extremely complicated and several formulations and formulae with different level of sophistication exist. The first development of a theory about multiple Coulomb scattering is attributed to Gert Molière [112]. A description of Molière theory can be found in [110].

For most practical cases, the distribution obtained by the Molière theory can be approximated well by a Gaussian distribution. However, the Molière distribution predicts larger probabilities for large multiple scattering angles, which results from the nature of the underlying Rutherford scattering processes. Figure 4.2 shows a measured scattering angle distribution of protons [109] compared with the Molière theory and with the approximation of a Gaussian distribution. In this logarithmic representation, it is evident that the tails of this distribution at large scattering angles cannot be described by a Gaussian.

According to the central limit theorem, for an infinite number of scatters, the distribution of the scattering angle is expected to be Gaussian. In the small-angle Gaussian approximation, the multiple scattering angular distribution is characterized by a single parameter, the standard

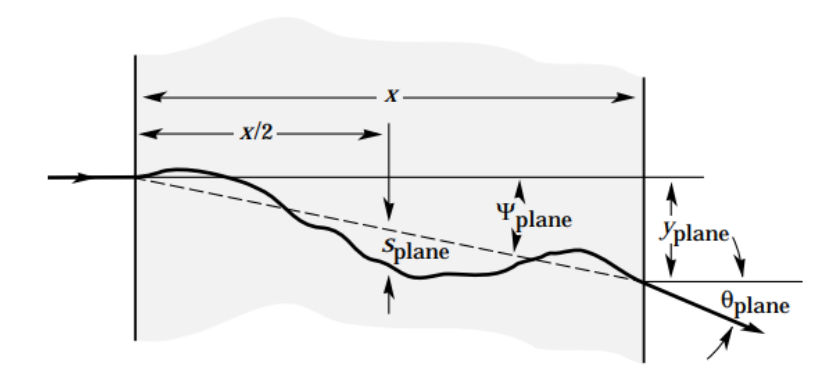


Figure 4.3: Sketch illustrating multiple scattering of a charged particle in a scattering layer projected onto a plane perpendicular to the incoming particle direction, as well as characteristic quantities used to describe this multiple Coulomb scattering process. Taken from [96].

deviation θ_{MCS} (often denoted θ_0 in the literature) of the angle θ_{plane} projected onto a plane perpendicular to the direction of motion of the incoming particle:

$$f(\theta_{\text{plane}})d\theta_{\text{plane}} = \frac{1}{\sqrt{2\pi}\theta_{\text{MCS}}} \exp\left(-\frac{\theta_{\text{plane}}^2}{2\theta_{\text{MCS}}^2}\right)d\theta_{\text{plane}}$$
 (4.2)

The spatial scattering angle θ_{space} , or θ for simplicity, is the angle between the particle direction before and after scattering, and is composed of two projected angles θ_x and θ_y as

$$\theta \approx \sqrt{\theta_{\text{plane,x}}^2 + \theta_{\text{plane,y}}^2}$$
 (4.3)

where x and y are orthogonal to the direction of motion. Note that θ can only assume positive values, in contrast to the projection of this angle onto a plane. The θ distribution is obtained as the product of the statistically independent distributions for θ_x and θ_y and is approximately

$$g(\theta)d\Omega = \frac{1}{2\pi\theta_{MCS}^2} \exp\left(-\frac{\theta^2}{2\theta_{MCS}^2}\right) d\Omega$$
 (4.4)

with $d\Omega \approx d\theta_{\text{plane,x}} d\theta_{\text{plane,y}}$. The maximum of the (4.4) is at $\theta = 0$ and corresponds to the most probable scattering angle in a solid angle interval $d\Omega$, while the standard deviation of θ is given by $\sqrt{2}\theta_{\text{MCS}}$ and approximately corresponds to the characteristic Molière angle θ_C in Figure 4.2. However, because the Molière distribution has longer tails, the true value is greater than θ_C .

Figure 4.3 shows θ_{plane} and other quantities used sometimes to describe multiple scattering, i.e. the deflection angle ψ_{plane} , the offset from the original entrance point y_{plane} and the central offset s_{plane} . The relation to the scattering angle parameter θ_{MCS} is given by [96]

$$\psi_{\text{plane}} = \frac{1}{\sqrt{3}} \theta_{\text{MCS}} \qquad y_{\text{plane}} = \frac{1}{\sqrt{3}} x \theta_{\text{MCS}} \qquad s_{\text{plane}} = \frac{1}{4\sqrt{3}} x \theta_{\text{MCS}} \qquad (4.5)$$

where x here is the thickness of the scattering medium.

4.1.1 The Highland formula

For many applications, the Gaussian approximation for the central 98% of the projection angle distribution described in (4.2) is sufficient. The standard deviation θ_{MCS} can be well described by the *Highland formula* [113]

$$\theta_{\text{MCS}} = \frac{S_2}{pc\beta} \sqrt{\frac{X}{X_0}} \left[1 + \varepsilon \ln \left(\frac{X}{X_0} \right) \right]$$
(4.6)

where p and β are respectively the momentum and the speed of the incident particle, X is the distance travelled by the incident particle in the scattering medium (which, for exiting particles, corresponds to the thickness of the medium), X_0 is the radiation length of the medium – and therefore X/X_0 can be considered as the number of radiation lengths travelled in the scattering medium – while S_2 and ε are two coefficients determined to be $S_2 = 13.6 \,\text{MeV}$ and $\varepsilon = 0.038$. Scattering angles due to multiple Coulomb scattering are at the order of mrad.

4.1.2 MCS as a tool to measure muon momentum

The underlying idea of this thesis is that multiple Coulomb scattering serves as a good tool for measuring particle momentum, given that (4.6) relates the standard deviation θ_{MCS} of the angular distribution with the momentum p of the incident particle, in a relationship that is inversely proportional — and this makes MCS ideal for an indirect measurement of momentum. In principle, this tool can be used for any charged particle; however, for particles such as protons, pions and kaons, nuclear interactions must also be considered.

Referring now to the specific case of muons in liquid Argon, which is the primary focus of this thesis, the main reasons supporting the choice of using MCS are detailed below:

- the approximation $m_{\text{nuclei}} \gg m_{\text{particle}}$, which allows to neglect the energy transferred from the muons to the Argon nuclei, is very well satisfied;
- nuclear interactions of muons are essentially negligible;
- in the absence of a magnetic field as is the case for all currently operating LArTPCs MCS represents the only method for measuring the momentum of a non-contained muon.

As described in Section 3.3, the energy of fully contained charged particles can be reconstructed using calorimetric or range-based techniques, but it is not possible to reconstruct the energy of non-contained particles using the same techniques. Indeed, the energy of hadrons, electrons and photons can be reconstructed through accurate calorimetric measurements of the associated showers; this is not possible for muons, which have a much greater mass than electrons — and thus are much less prone to generating electromagnetic showers — and do not participate in strong interactions like hadrons — and thus do not generate hadronic showers. Moreover, muons lose energy along their path through ionization and might generate delta rays, i.e. electrons of

Argon atoms to which a significant amount of energy is transferred. The energy of delta rays is large enough to expel an electron from the atom and create thus a secondary ionization.

Two different algorithms represent the state of the art for measuring muon momentum in a LArTPC using MCS-based techniques. The general idea of these algorithms is to extract a statistical measure of the average deflection taking into account both measurement errors, due to the finite resolution on the spatial reconstruction of tracks, and systematic errors, due to detector effects that might distort the field and create fake deflections. The procedure involves segmenting the muon track and measuring the averaged deflection over each segment, and this is applied in different ways in the two algorithms, as detailed in the following subsections.

We renamed these two algorithms as "Gran Sasso" algorithm and "MicroBooNE" algorithm. By "Gran Sasso" algorithm we refer to the momentum measurement algorithm developed for the ICARUS experiment when it was still at the INFN Laboratori Nazionali del Gran Sasso underground laboratory [114] [115]. By "MicroBooNE" algorithm we refer to the momentum measurement algorithm originally developed for the MicroBooNE detector [116], which employs the same LArTPC technology of ICARUS. The name chosen for this algorithm only denotes its historical origin; however, it must be clear that in the context of this thesis, the "MicroBooNE" algorithm is applied to the ICARUS detector at FNAL.

The main difference between these algorithms is the input data format. The "Gran Sasso" algorithm was originally designed to use the 2D hit points in the *Collection view* — see Subsection 3.2.2. I have developed an innovative version of "Gran Sasso" algorithm that still uses the 2D points but in any of the three *reconstruction views* (Induction-1, Induction-2 and Collection). The "MicroBooNE" algorithm uses the Pandora-reconstructed 3D hit points — see Subsection 3.2.3. I have developed also an innovative version of "Gran Sasso" algorithm that, similarly to the "MicroBooNE" algorithm, uses the 3D hit points.

4.2 "Gran Sasso" algorithm

As explained in the previous section, there are two versions of the "Gran Sasso" algorithm. The 2D version uses the hit points on any of the reconstruction planes (Induction-1, Induction-2 and Collection): these planes are defined by the drift direction and the normal to the wire on that wire plane. The 3D version uses instead the hit points reconstructed by Pandora on the x, y, z reference frame. In any case, the first step of the "Gran Sasso" algorithm consists in dividing the muon track, which has initial length X, into a number n_{seg} segments with length L_{seg} . The segmentation chosen represents a compromise between different requirements: longer segments allow enhancing the physical MCS deflections, which grow as $\sqrt{L_{\text{seg}}}$, while reducing the impact of measurement errors on single wires; but on the other hand, an adequate segment statistics (≥ 8) is required to correctly estimate average deflections, even for the shortest lengths. Both the 2D and the 3D versions segment the track into segments of length $L_{\text{seg}} = X_0 = 14 \, \text{cm}$, that

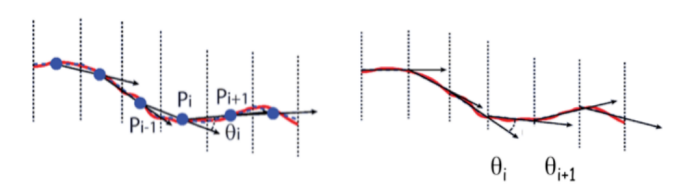


Figure 4.4: Scheme of the two different approaches to define deflection angle: the polygonal (on the left) and the linear-fit (on the right). Taken from [115].

was chosen to ensure a fair comparison with the "MicroBooNE" algorithm, which uses a fixed segment length L_{seg} .

The muon trajectory within a segment is given by its slope and the position of the barycenter of the associated hits. With this two parameters, two definitions of the deflection angle between consecutive segments can be considered. In the polygonal approach, the deflection angle θ_{pol} is defined as the angle between two consecutive pieces of the polygonal line connecting the corresponding barycenter points, as shown in Figure 4.4 (left). In the linear-fit approach, each segment is fitted independently with a straight line, and the deflection angle θ_{lin} is defined as the difference between the fitted slopes of two consecutive segments, as shown in Figure 4.4 (right). The second approach in 3D is the one used by the "MicroBooNE" algorithm to find the observed deflection; the "Gran Sasso" algorithm uses both the approaches, both in its 3D and in its 2D version, in order to maximize the information from the muon track.

Note that the algorithm operates under the Gaussian approximation of MCS – see Subsection 4.1.1 – and applies a single-scattering-based cut that removes non-Gaussian tails beyond 3σ .

In the 3D version of the algorithm, the standard deviation of the deflection angle between two consecutive segments due to MCS is given by the Highland formula as defined in (4.6), where the logarithm term is null if $L_{\text{seg}} = X_0$ is chosen, which means

$$\theta_{\text{MCS}}^{(3D)}(p_i) = \frac{S_2}{p_i c \beta} \sqrt{\frac{L_{\text{seg}}}{X_0}} = \frac{S_2}{p_i c \beta}$$

$$(4.7)$$

The momentum p_i refers to the *i*-th segment of the track and it is calculated from the initial momentum p_0 assigned to the track, accounting for the energy losses along the muon path as measured by the calorimetry.

In the 2D version of the algorithm, there is a reduction of the MCS effect due to the fact that the deflection is projected on a plane, which means

$$\theta_{\text{MCS}}^{(2D)}(p_i) = \frac{S_2}{p_i c \beta} \sqrt{\frac{L_{\text{seg}}}{X_0}} \frac{w_0}{L_{\text{2D}}/L_{\text{3D}}}$$
(4.8)

The w_0 factor depends on the segment length and for $L_{\rm seg} \sim X_0$ it was estimated to be $w_0 \sim 0.74$ for the polygonal approach and $w_0 \sim 0.86$ for the linear-fit approach, with a numerical model simulating individual Coulomb scattering on a large number ($\sim 10^6$) of tracks. The length $L_{\rm 2D} = \sqrt{L_{\rm drift}^2 + L_{\rm wire}^2}$ is the projection of the track length on the reconstruction plane, given

by drift and wire coordinates, while the length $L_{3D} = \sqrt{L_x^2 + L_y^2 + L_z^2}$ is the 3D track length; the ratio L_{2D}/L_{3D} accounts for the projection on the reconstruction plane of the MCS angle.

4.2.1 Measurement error contributions

Measurement errors in reconstructing the position of hits result in apparent track deflections, which can mimic the physical effect of multiple scattering: a correct estimate of the resolution on all spatial coordinates is therefore crucial. The precision on wire positioning is better than $0.01\,\mathrm{mm}$ and its contribution to the uncertainty on the hit position measurement has been neglected. A more significant contribution comes from the x drift coordinate as obtained from a fit of the wire signal shape, which is affected by the response of readout electronics and associated noise — note that the fit occurs downstream of the deconvolution, as explained in subsection 3.2.1.

The single hit uncertainty can be then disentangled from the MCS contribution by measuring the dispersion in the x drift coordinate with respect to a straight line on a short part of the muon track, where the effect of multiple Coulomb scattering can be neglected. The minimum length required to disentangle the measurement effect from that of MCS is the one formed by three consecutive hits, and in fact sets of three consecutive hits have been considered; for each of them, the algorithm computes the distance δ_{3P} from the middle point to the average position of the two adjacent points, and assigns every single point a resolution σ_{3P} which is proportional to the RMS of the δ_{3P} distribution. The obtained δ_{3P} distance results very stable along each muon track – stable within ~ 1% between the first and second half of each track – allowing the use of a single value for all hits in a single event [115]. In this way, it is possible to provide a track-dependent measurement of this error instead of assigning the same value to all tracks. Computation of δ_{3P} occurs independently for all of three reconstruction planes; the 3D version of the algorithm takes an average of the three values of δ_{3P} . The obtained single point resolution σ_{3P} is then used to compute the error contribution θ_{3P} . Note that θ_{3P} is not constant but is calculated for each muon track.

In the 3D version of the algorithm, the error contribution θ_{3P} can be expressed as

$$\theta_{3P}^{(3D)} \propto \frac{\sigma_{3P}}{L_{\text{seg}}\sqrt{n_h}} \sqrt{1 - \frac{L_{\text{drift}}^2}{L_{3D}^2}}$$
 (4.9)

 L_{drift} is the track length along the drift coordinate. If the track is parallel to drift direction, then $L_{3D} \to L_{\text{drift}}$ and $\theta_{3P}^{(3D)} \to 0$; if it is normal to drift direction, $L_{\text{drift}} \to 0$ and $\theta_{3P}^{(3D)}$ is maximized. In the 2D version of the algorithm, the error contribution θ_{3P} can be expressed as

$$\theta_{3P}^{(2D)} \propto \frac{\sigma_{3P}}{L_{\text{seg}}\sqrt{n_h}} \sqrt{1 - \frac{L_{\text{drift}}^2}{L_{2D}^2}}$$
 (4.10)

If the projected track is parallel to drift direction, then $L_{\rm 2D} \to L_{\rm drift}$ and $\theta_{3P}^{\rm (2D)} \to 0$; otherwise, if it is normal to drift direction, $L_{\rm drift} \to 0$ and $\theta_{3P}^{\rm (2D)}$ is maximized.

In both the versions, L_{seg} is the segment length and n_h is the number of hits per segment. The proportionality coefficient depends on the approach used and is obtained directly from the error propagation: for the polygonal approach is $\sqrt{6}$, for the linear-fit approach is $\sqrt{24}$. The observed deflection contains thus an independent measurement error contribution θ_{3P} , in addition to the genuine MCS term θ_{MCS} : while the former does not depend on muon momentum, the latter obviously depends on p_i and for a muon with $p \sim 2 \,\text{GeV}\,\text{c}^{-1}$ the MCS term is comparable with θ_{3P} [115]; in any case, the range considered for this analysis does not reach such momenta.

4.2.2 Estimate of muon momentum

The two different approaches used to determine the deflection angles $\theta_{\rm pol}$ and $\theta_{\rm lin}$ imply that, if $n_{\rm seg}$ is the number of segments, there are $n_{\rm seg}-2$ deflections computed with the polygonal definition and $n_{\rm seg}-1$ deflections computed with the linear-fit definition, which means $2n_{\rm seg}-3$ observed scattering angles in total. In order to compare these observed deflections on a muon track with the expectation for a given momentum p, the "Gran Sasso" algorithm uses a χ^2 -like function called C_2 function and constructed as

$$C_2(p) = V^T C^{-1}(p)V (4.11)$$

where V is a $2n_{\text{seg}} - 3$ vector that contains all the observed scattering angles, both the $n_{\text{seg}} - 2$ computed with the polygonal approach and the $n_{\text{seg}} - 1$ computed with the linear-fit approach, and C(p) is a matrix that expresses the expected scattering angles and their mutual correlations

$$V = \begin{pmatrix} V_{\text{poly}} \\ V_{\text{lin}} \end{pmatrix} \qquad C(p) = \begin{pmatrix} C_{\text{poly}}(p) & C_{\text{mix}}(p) \\ {}^{T}C_{\text{mix}}(p) & C_{\text{lin}}(p) \end{pmatrix}$$
(4.12)

The detailed expressions for all these sub-matrices can be found in Appendix A.

The determination of the muon momentum is based on the fit of the C_2 function with respect to the unknown initial track momentum p. The best estimate p_{MCS} , given the observed deflections, is obtained assuming $C_2(p_{\text{MCS}}) = 2n_{\text{seg}} - 3$ which means the RMS of the observed deflection angles matches on average the value expected from the instrumental and MCS contributions. Around its best value p_{MCS} , the C_2 function follows the condition

$$\frac{C_2(p)}{2n_{\text{seg}} - 3} = \frac{1}{\alpha + \beta/p^2} \tag{4.13}$$

where α and β/p^2 refer respectively to the instrumental and MCS contributions to the observed deflection. In an ideal world where both θ_{MCS} and $\theta_{3\text{P}}$ are perfectly estimated and there are no statistical fluctuations, p_{MCS} is the momentum that makes $C_2 = 2n_{\text{seg}} - 3$. Obviously, in reality,

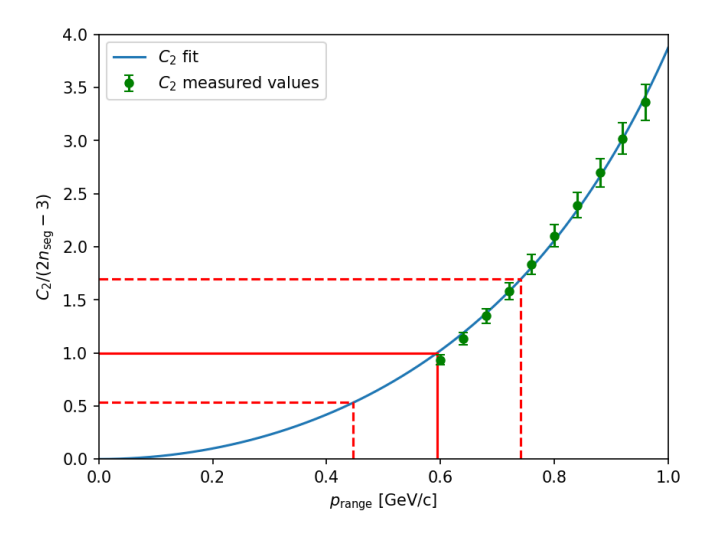


Figure 4.5: Fit to the $C_2(p)$ function, for a stopping muon. The value of momentum p from range is $0.73\,\mathrm{GeV}\,\mathrm{c}^{-1}$. The fitted values of α and β are approximately -0.15 and $0.40\left(\mathrm{GeV}\,\mathrm{c}^{-1}\right)^2$ respectively. The resulting momentum is $p_{\mathrm{MCS}} \simeq 0.59\,\mathrm{GeV}\,\mathrm{c}^{-1}$. The dashed red lines refer to the error associated to reconstructed momentum.

this holds only on average and to the extent that we correctly estimate all the contributions in an unbiased way. The relative statistical uncertainty for the C_2 function is given by

$$\frac{\Delta C_2}{C_2} = \sqrt{\frac{2}{2n_{\text{seg}} - 3}} \tag{4.14}$$

since for the true momentum C_2 function is distributed as a χ^2 with $2n_{\rm seg}-3$ degrees of freedom. Therefore, the associated relative resolution on the momentum estimation is

$$\frac{\sigma_p}{p} = \frac{1}{\sqrt{2(2n_{\text{seg}} - 3)}} \left(1 + \frac{\alpha p^2}{\beta} \right) \tag{4.15}$$

where the n_{seg} dependent factor accounts for the statistical uncertainty on the C_2 distribution and corresponds to the lower limit of the resolution as obtained at very low p values.

4.3 "MicroBooNE" algorithm

The first step of the algorithm is the track segmentation, which begins at the start of the track and iterates through the trajectory points in order, defining segment start and stop points based on the straight-line distance between them. There is no overlap between segments. A fixed segment length of $L_{\text{seg}} = X_0 = 14 \,\text{cm}$ is used.

Given the subset of the three-dimensional trajectory points that corresponds to one segment of the track, a three-dimensional linear fit is applied to the data points, weighting all trajectory points equally in the fit. The position of the particle at each segment break point was obtained

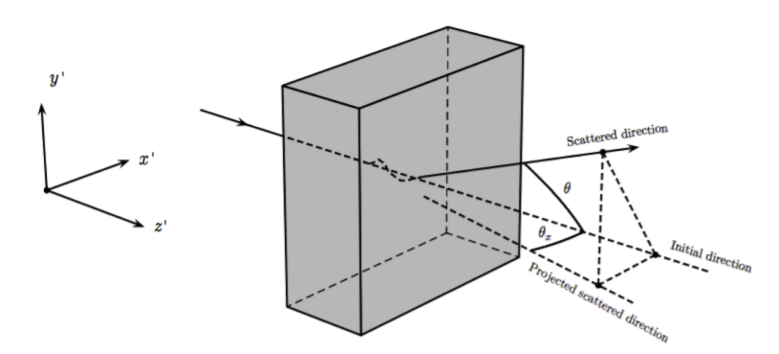


Figure 4.6: Schematics of the trajectory deflection as the incident particle crosses the material. Only the angular scatter with respect to the x' direction, shown as θ_x , is drawn. Taken from [116].

by linear interpolation between the nearest recorded particle trajectory points. The direction of each segment was calculated as the main component of all points within the segment, and the angle between two segments was calculated from the direction of those two segments.

With the segments defined, the scattering angles between the linear fits from adjacent segments are computed. A coordinate transformation is performed such that the z' direction is oriented along the direction of the linear fit to the first of the segment pair, while the x' and y' coordinates are chosen such that x', y', z' are mutually orthogonal and right-handed, as shown in Fig. 4.6. The scattering angles with respect to the x' direction and the y' direction are then computed and used as the input to the MCS algorithm.

4.3.1 Tuning of the Highland formula

The Highland coefficients $S_2 = 13.6 \,\mathrm{MeV}$ and $\varepsilon = 0.088$ [113] were determined from a global fit to MCS simulated data, using a modified GEANT simulation package of 14 different elements and 7 thickness ranges. All the simulated particles were relativistic, with $\beta = 1$, and the materials studied ranged from Hydrogen (Z = 1) to Uranium (Z = 92). The "MicroBooNE" algorithm was then developed starting from the idea that the coefficients S_2 and ε could differ for scattering specifically in liquid Argon and might be momentum-dependent for muons with $\beta < 1$, which is the case for some of the contained muons analyzed.

A large sample of muons were simulated in the MicroBooNE TPC to re-tune S_2 and ε for liquid Argon, and their true angular scatters were used in a fit, with $X = X_0$ to simplify (4.6) as

$$\theta_{\text{MCS}}(p) \bigg|_{X=X_0} = \frac{S_2}{pc\beta}$$
 (4.16)

Note that using a segment length different from X_0 requires a simultaneous fit both for S_2 and ε , while imposing $X = X_0$ allows to remove the dependence of ε and focus only on S_2 . This coefficient has been fitted for as a function of true momentum p_{true} at each scatter in order to explore its β dependence, as shown in Figure 4.7. The fitted value of S_2 is always less than the nominal 13.6 MeV quoted in literature, for momenta $p_{\text{true}} > 0.25 \,\text{GeV}\,\text{c}^{-1}$, and

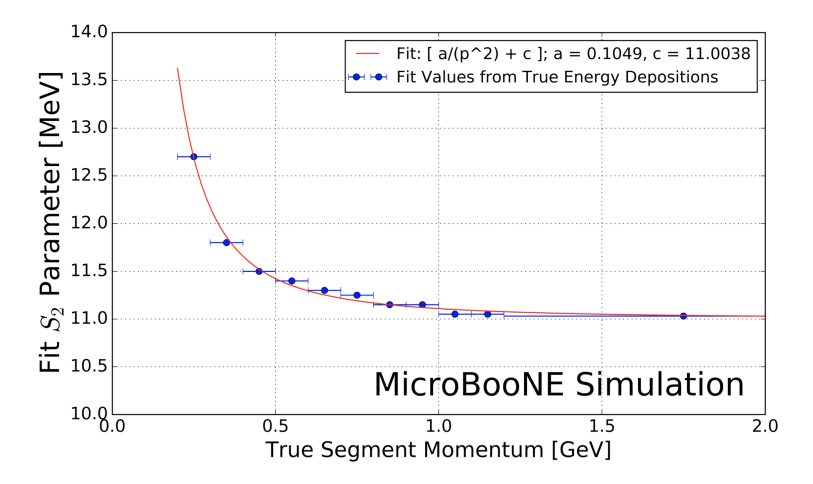


Figure 4.7: Fitted coefficient S_2 as a function of true segment momentum for $X = X_0$ simulated muons in the MicroBooNE LArTPC. Blue error bars indicate the true momentum bin width with data points at the center of each bin. In red a fit to these data points with a functional form. Taken from [116].

asymptotically approaches a constant at higher momenta (for $\beta \to 1$) of about 11 MeV. The functional form used has been chosen because it captures the trend in the fit value of S_2 with respect to momentum and will henceforth be referred to as $\kappa(p)$ [116].

In this way the tuned Highland formula for MCS angle becomes

$$\theta_{\text{MCS}}(p)\Big|_{X=X_0} = \frac{\kappa(p)}{pc\beta} \quad \text{where } \kappa(p) = \kappa_1 + \frac{\kappa_2}{|p|^2}$$
 (4.17)

Note that, from a dimensional point of view, θ_{MCS} is an angle with units of rad, while S_2 is an energy with units of MeV (and then p is a momentum with units of MeV c^{-1}), thus $\kappa(p)$ must be an energy with units of MeV. Since the coefficients κ_1 and κ_2 are quoted in literature with units of MeV [116], the dependence on p^{-2} must be followed by the clarification that this "p" is taken as a momentum with units of GeV c^{-1} and is divided by $1 \text{ GeV } c^{-1}$, so that it turns out to be adimensional — and this is the reason why in Eq. (4.17) there is |p| and not just p.

This modified version of the Highland formula used by the "MicroBooNE" algorithm directly includes the detector-inherent angular resolution term $\theta_{\rm res}$, which is given a fixed value of 3 mrad, determined to be an acceptable value based on the MicroBooNE simulation studies of muons at high momenta. Eq. (4.6) predicts a RMS angular scatter of $\theta_{\rm res} = 3 \,\mathrm{mrad}$ at $4.5 \,\mathrm{GeV}\,\mathrm{c}^{-1}$ muon momentum and $X = X_0$, comparable to the detector resolution, and since the fully contained muons addressed in our analysis have momenta much less than $4.5 \,\mathrm{GeV}\,\mathrm{c}^{-1}$, the impact of this detector resolution will be minimal for our sample.

Finally, the formula used to compute the expected deflection for $X=X_0$ can be summarized as

$$\theta(p)\Big|_{X=X_0} = \sqrt{\theta_{\text{MCS}}(p)^2 + \theta_{\text{res}}^2} = \sqrt{\left[\frac{\kappa(p)}{pc\beta}\right]^2 + \theta_{\text{res}}^2}$$
 (4.18)

where $\kappa(p)$ uses the parameters values of κ_1 and κ_2 tuned for ICARUS, as well as $\theta_{\rm res}$.

4.3.2 Estimate of muon momentum

As described in Section 4.1, the probability distribution for an observed deflection θ_{obs} in one of the two directions orthogonal to the direction of motion x', y' is given by (4.2), while the expected deflection θ_{exp} is given by the tuned formula in (4.18). Since energy is lost between segments along the track, θ_{exp} increases for each angular measurement along the track: θ_{exp} is then replaced by $\theta_{\text{exp},j}$ where j is an index representative of the segment.

The likelihood is obtained as the product of all the $f(\theta_{\text{obs},j})$ given by (4.2) over all $n_{\text{seg}} - 1$ of the $\theta_{\text{obs},j}$ segment-to-segment scatters along the track, and can be written as

$$L(\theta_{\exp,j}, \theta_{\text{obs},j}) = \frac{1}{\sqrt{(2\pi)^{n_{\text{seg}}-1}}} \left[\prod_{j=1}^{n_{\text{seg}}-1} \frac{1}{\theta_{\exp,j}} \right] \exp\left[-\frac{1}{2} \sum_{j=1}^{n_{\text{seg}}-1} \left(\frac{\theta_{\text{obs},j}}{\theta_{\exp,j}} \right)^2 \right]$$
(4.19)

Rather than maximizing the likelihood, it is more computationally convenient to minimize the negative log likelihood. Given a set of angular deflections in the x' and y' directions, for each segment a scan is done over the postulated initial energy E_0 in steps of 1 MeV up to 15 GeV. The step with the smallest negative log likelihood is chosen as the best value of energy E_{MCS} , and therefore this energy is converted to a best value of momentum p_{MCS} through (3.15). The energy E_j of the j-th segment is related to the initial energy E_0 by

$$E_j = E_0 - \Delta E_j \tag{4.20}$$

where ΔE_j is the energy loss upstream of the j-th segment, computed by integrating the muon stopping power curve given by the Bethe-Bloch equation — as described in Section 3.3 — along the length of track upstream of this segment. To overcome the problem of delta rays, the most probable value of the energy loss distribution is used, rather than its mean, according to the Landau limit described in Equation (3.7). This value of segment energy E_j is then converted to a momentum p through (3.15) and used to predict the RMS angular scatter for that segment by way of Equation (4.18).

4.4 Comparison of the two algorithms

The main common features between the "Gran Sasso" and the "MicroBooNE" algorithms are the segmentation of the muon track into smaller pieces and the consideration of energy loss along track direction when calculating the expected angles, in agreement with the Highland formula. The Landau limit, used to estimate the energy loss for each segment, is only applicable to energy depositions far from the stopping point of a particle. For contained muons near the Bragg peak (i.e. near to their stopping point) the MCS scattering angles get extremely large, before the track fully ranges out and the computed scattering angles become unphysical.

Any algorithm that derives the muon momentum via MCS-based techniques must account for these effects, because the C_2 function fit – or the likelihood minimization – would be strongly biased towards a p_{MCS} value very close to the range momentum p_{range} . In order to avoid this case and provide a validation of the p_{MCS} computation that realistically mimics the case of uncontained muons, the last three angles are excluded from the C_2 function calculation and from the likelihood calculation, respectively for the two algorithms. This results in effectively having a physically acceptable lowest momentum p_{low} , which corresponds to the range of the fraction of muon track that is considered for the measurement: the computed p_{MCS} cannot be lower than the integrated energy loss along this fraction of the track. In other words, Equation (4.20) introduces a minimum allowable track energy determined by the range of the track, as the energy E_j of the j-th segment must remain positive.

The main differences between the two algorithms are:

- the input data format. As already explained in Subsection 4.1.2 there is a 2D version of "Gran Sasso" algorithm which uses the 2D hit points on the reconstruction planes and a 3D version which uses the 3D hit points as reconstructed by Pandora. The "MicroBooNE" algorithm is intrinsically only 3D and only uses Pandora-reconstructed 3D hit points.
- the use of the Highland formula. The "Gran Sasso" algorithm uses the (4.6) version of the Highland formula while the "MicroBooNE" algorithm performs a tuning of the formula, as described in Subsection 4.3.1;
- the measured deflections. The "Gran Sasso" algorithm measures the physical deflection both in the polygonal approach and in the linear-fit approach, as explained in Section 4.2, to maximise the information from the track. The "MicroBooNE" algorithm only measures the linear-fit deflection.
- the angular resolution. The "MicroBooNE" algorithm includes a fixed angular resolution term in the formula, while the "Gran Sasso" algorithm includes a variable resolution term which derives directly from the measurement errors on the drift coordinate, which can differ among tracks, as will be described in subsection 4.2.1;
- the segment length. Both algorithms employs a segmentation of the muon track, but the "MicroBooNE" algorithm must use a fixed segment length $L_{\text{seg}} = X_0$ while in principle the "Gran Sasso" algorithm can use an arbitrary segment length. Note that, for a fair comparison, during the analysis performed in this thesis, the segment length used in the "Gran Sasso" algorithm was always the Argon radiation length $L_{\text{seg}} = X_0 = 14 \,\text{cm}$;
- the statistical method. The "Gran Sasso" algorithm constructs a χ^2 -like function, while the "MicroBooNE" algorithm performs a maximisation of the function that parametrizes the likelihood that the observed scattering angles match expectations for a given momentum;

Chapter 5

MCS analysis on MC muon tracks

Both the "Gran Sasso" and the "MicroBooNE" MCS algorithms have been developed under experimental conditions that were similar, but not identical, to the ICARUS detector at FNAL. For the analysis reported in this chapter I used a Monte Carlo sample of cosmic muons — an explanation on how cosmic muon tracks are simulated can be found in Subsection 3.4.

We need to compare MCS momentum with another independent measurement of momentum, to evaluate the performance of the MCS-based momentum estimation method on muon tracks. The MC simulation provides access to the true generated muon momentum, referred to as p_{true} in the following. Stopping muons provide also the momentum obtained from the range-based method, referred to as p_{range} in the following, as explained in Subsection 3.3.2. Since the truth-level quantities are available only in the simulation, in order to compare the results between MC and real data, we decided to report our results as a function of p_{range} also for the simulated data, and then we required the tracks to be stopping muons. For this reasons, we applied a set of quality cuts on the tracks which include:

- a defined time t_0 as stated in Subsection 3.2.3, in order to correctly locate the hits along the drift coordinate so that a fiducial volume can be defined, and to correct the charge for attenuation due to Argon impurities see Subsection 3.3.1;
- a length $L > 40 \,\mathrm{cm}$ and a median $\mathrm{d}Q/\mathrm{d}x > 1000 \,\mathrm{ADC/cm}$ in the last 5 cm of track, the latter being the threshold of a large energy deposition due to the Bragg peak [102] see Section 3.3 in order to identify the track as a muon track;
- the vertical coordinate of their starting point greater than that of their ending point, in order to be sure that cosmic muons (which come from above) are well reconstructed.

The last requirement has been applied because we identified a subsample of muon tracks reconstructed with inverted starting and ending points. If starting and ending points are reversed, the computation of expected scattering angle (that takes into account energy loss) would return wrong values. In order to prevent this effect from influencing the performance of the algorithm, we removed such tracks — about 14% of the original sample — using the MC truth information of starting and ending points of the muon tracks.

In both the "Gran Sasso" and the "MicroBooNE" algorithms, the track segmentation implies a computation of segment momentum by subtracting energy loss from the particle momentum hypothesis. To prevent this effect from overestimating the performance of the algorithms, and to effectively simulate the application of this method to non-stopping tracks (i.e. avoid using the information of the large energy deposition due to Bragg peak), the last three angles — i.e. the last four segments — were excluded from the C_2 function calculation and the likelihood calculation, respectively: this corresponds roughly to discarding the last $\sim 50\,\mathrm{cm}$ of the track. This implies that, if a track segment is 14 cm long and the number of angles is $n_{\mathrm{seg}}-1$, for a track of length $L\sim 1.5\,\mathrm{m}$ there are $n_{\mathrm{seg}}\sim 11$ segments and 10 linear-fit angles, which means 7 angles used in the fit functions. Therefore I require a muon track length above 1.5 m, that corresponds roughly to a momentum of $\sim 0.45\,\mathrm{GeV}\,\mathrm{c}^{-1}$. Below this value, the segment statistics would be too low to provide a reliable measurement of momentum via MCS.

5.1 Characterization of the muon sample

The sample of MC stopping muon tracks we are using includes 2072 tracks with momentum between $0.45 \,\mathrm{GeV}\,\mathrm{c}^{-1}$ and $1 \,\mathrm{GeV}\,\mathrm{c}^{-1}$. As stated at the beginning of this chapter, we are reporting the results as a function of p_{range} . For MC tracks, we also know the true momentum p_{true} . The distribution of $p_{\mathrm{range}}/p_{\mathrm{true}} - 1$ and the p_{range} distribution in function of a p_{true} distribution are reported below and shown in Figure 5.1.

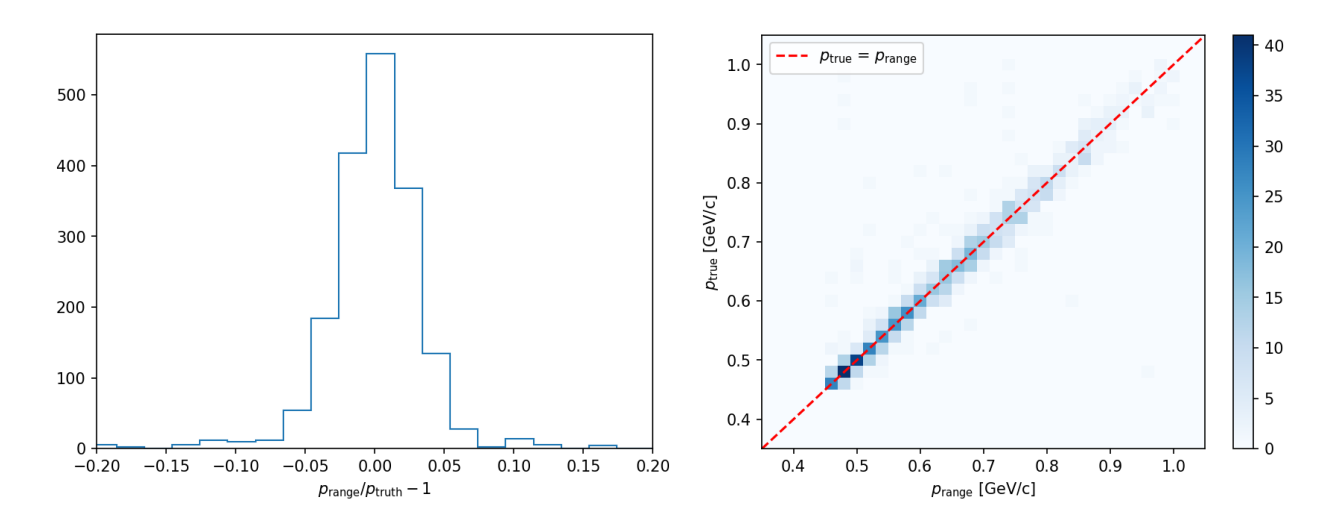


Figure 5.1: (Left) distribution of $p_{\text{range}}/p_{\text{true}} - 1$, in bins of 0.02. (Right) p_{range} in function of p_{true} , in bins of 0.02 GeV c⁻¹ × 0.02 GeV c⁻¹; the red line represents $p_{\text{true}} = p_{\text{range}}$.

The distribution is peaked at zero and has a resolution of about 2% as obtained from a Gaussian fit, in agreement with what is shown in Figure 5.1 (right), where the points lie mainly on the line $p_{\text{true}} = p_{\text{range}}$. This provides an estimate of the accuracy of the p_{range} measurement, for a sample of stopping muons. Once this is established, we can proceed with the characterization of our sample. Figure 5.2 shows the distributions of track length L, range momentum p_{range} and

cosine of the angles θ_x , θ_y , θ_z between the track direction and the three main directions x, y, z – respectively, the drift direction, the vertical direction, and the beam direction. Consistently with what will be shown later, it was decided to show also the distribution of p_{range} in bins of $100 \,\text{MeV}\,\text{c}^{-1}$, grouping tracks with momentum between 0.8 and $1.0 \,\text{GeV}\,\text{c}^{-1}$ into a single bin, given the lower statistics at higher momenta.

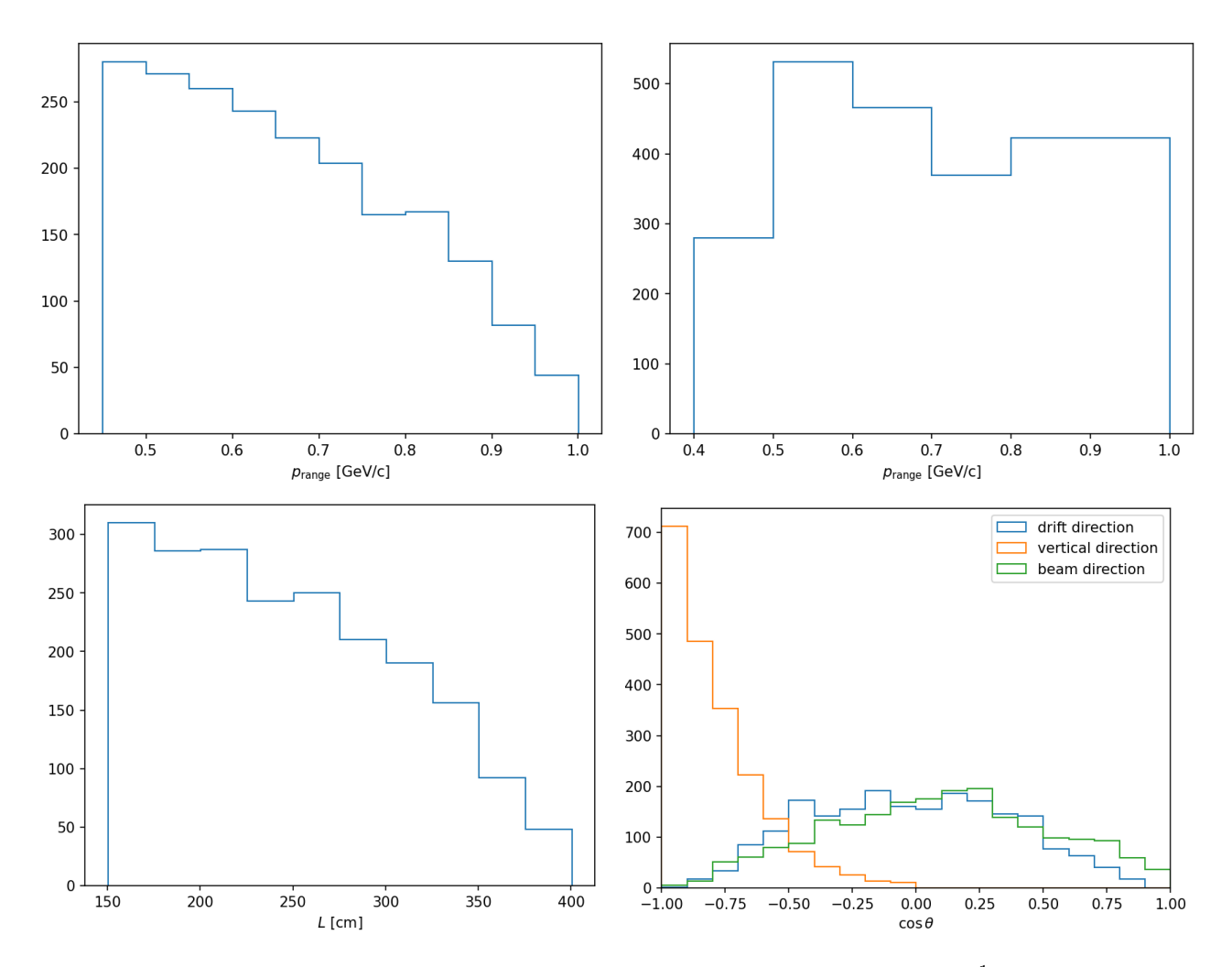


Figure 5.2: (Top left) distribution of range momentum p_{range} in bins of 50 MeV c⁻¹. (Top right) same distribution in bins of 100 MeV c⁻¹, except for the last bin which has a width of 200 MeV c⁻¹. (Bottom left) distribution of length L in bins of 25 cm. (Bottom right) distribution of $\cos \theta$ with respect to the main directions – the drift direction x, the vertical direction y, the beam direction z – in bins of 0.1.

The angular distribution in Figure 5.2 (bottom right) shows that, while along the drift and the beam direction there is no preferred direction, along the vertical direction there is a peak in $\cos \theta_y = -1$ as expected by selecting downgoing cosmic muons.

Apart from angular distributions with respect to the three directions, since the "Gran Sasso" algorithm in its original version works only on the Collection plane and considers the muon track projected on the plane, three different angular distributions can be shown (L_x and L_{drift}) here refer to the track length along the drift direction x, with $L_x = L_{\text{drift}}$):

• distribution of $\cos \theta_{13} - \theta_{13}$ is the angle between the 1D track direction along the drift direction x and the 3D track direction in space – that can be viewed as $\cos \theta_{13} = L_{1D}/L_{3D}$ where L_{1D} is the track length along the drift direction and L_{3D} is the track length in space

$$\cos \theta_{13} = \frac{L_{1D}}{L_{3D}} = \frac{L_x}{\sqrt{L_x^2 + L_y^2 + L_z^2}}$$
 (5.1)

If the track is orthogonal to the drift direction (i.e. isochronous track) then $L_x \to 0$ and $\cos \theta_{13} \to 0$, while if the track is parallel to drift direction then $L_{3D} \to L_x$ and $\cos \theta_{13} \to 1$;

• distribution of $\cos \theta_{12} - \theta_{12}$ is the angle between the 1D track direction along the drift direction x and the 2D track direction on the reconstruction plane – that can be viewed as $\cos \theta_{12} = L_{1D}/L_{2D}$ where L_{1D} is the track length along the drift direction and L_{2D} is the track length projected on the reconstruction plane

$$\cos \theta_{12} = \frac{L_{1D}}{L_{2D}} = \frac{L_{\text{drift}}}{\sqrt{L_{\text{drift}}^2 + L_{\text{wire}}^2}}$$
 (5.2)

If the projected track is orthogonal to the drift direction then $L_{\text{drift}} \to 0$ and $\cos \theta_{12} \to 0$, while if the projected track is parallel to drift direction then $L_{\text{2D}} \to L_{\text{drift}}$ and $\cos \theta_{12} \to 1$;

• distribution of $\cos \theta_{23} - \theta_{23}$ is the angle between the 2D track direction on the reconstruction plane and the 3D track direction in space – which can be viewed as $\cos \theta_{23} = L_{\rm 2D}/L_{\rm 3D}$ where $L_{\rm 2D}$ and $L_{\rm 3D}$ have been defined above

$$\cos \theta_{23} = \frac{L_{2D}}{L_{3D}} = \frac{\sqrt{L_{\text{drift}}^2 + L_{\text{wire}}^2}}{\sqrt{L_x^2 + L_y^2 + L_z^2}}$$
 (5.3)

In this case, $\cos \theta_{23} \to 0$ means the track is orthogonal to the reconstruction plane, while $\cos \theta_{23} \to 1$ means that the track lies on the reconstruction plane.

Figure 5.3 shows these angular distributions. Each distribution is made for each of the three reconstruction planes, Induction-1, Induction-2 and Collection, which we know have different orientations in space. Note that Induction-2 and Collection planes are expected to have similar distributions, since their wires are oriented at $\pm 60^{\circ}$ with respect to the horizontal direction – see Section 2.2. Figure 5.3 (top) shows that the number of tracks with $\cos \theta_{13} \rightarrow 1$ is small in all planes, both because of solid angle effects and inefficiencies in Pandora reconstruction.

Figure 5.3 (middle) shows a flat distribution for $\cos \theta_{12} < 0.9$ and a peak for $\cos \theta_{12} \to 1$ both in Induction-2 and Collection planes, while the peak is not observed in Induction-1 plane. This means that the number of the projected tracks parallel to drift tends to 0 in the Induction-1 view, and this is due to the different orientation of wires. Induction-1 plane has horizontal wires, thus cosmic muons — mainly vertical, as seen in Figure 5.2 — tend to be orthogonal to wires.

Figure 5.3 (bottom) shows that the number of tracks with $\cos \theta_{23} \to 0$ is small in all planes, and this is more pronounced in the Induction-1 view, since a track orthogonal to the Induction-1

plane would be an horizontal track. Again, this is expected in a sample of comic muons which have mostly a vertical direction. There is a peak for $\cos \theta_{23} \to 1$ in the Induction-1 view, which means there are many tracks lying on the plane; again, this is expected for geometrical reasons.

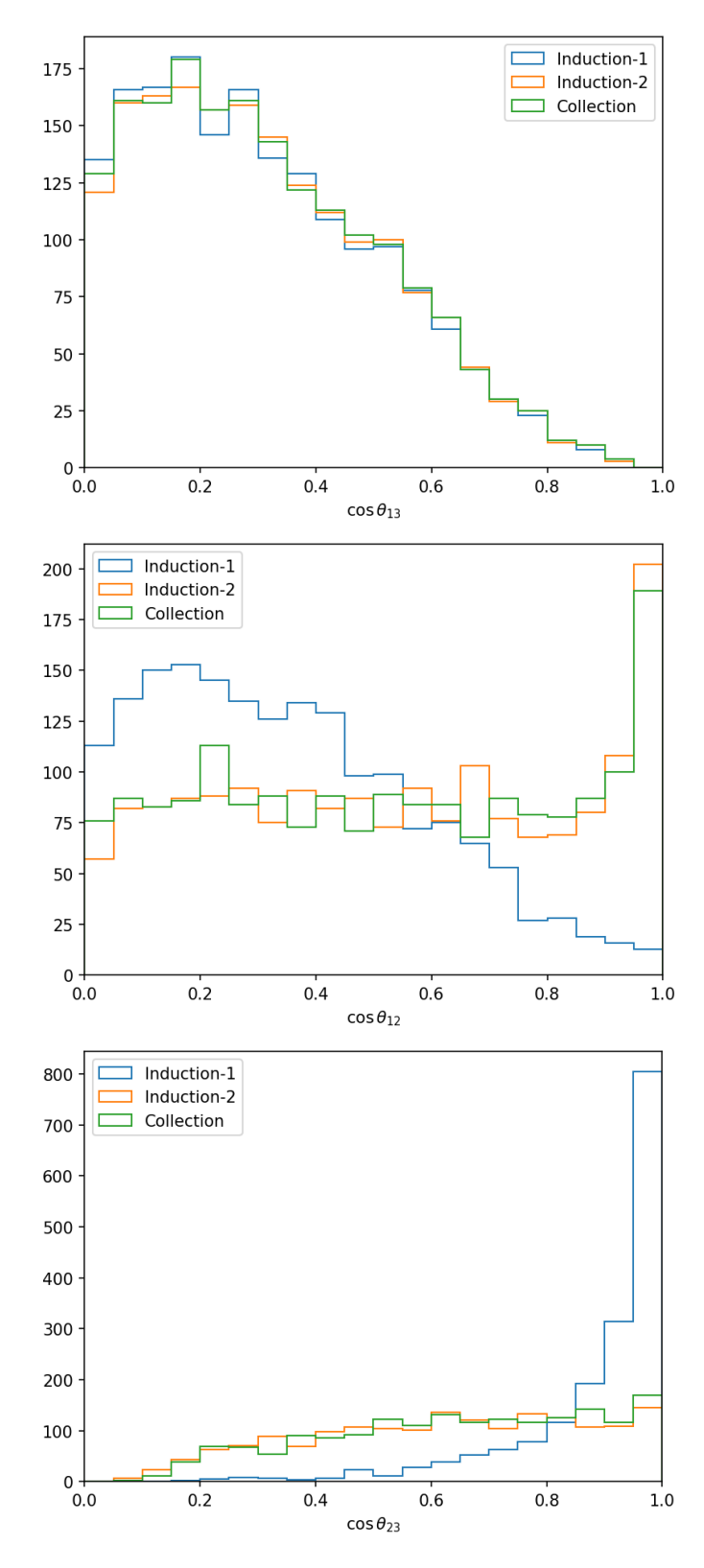


Figure 5.3: (Top) distribution of $\cos \theta_{13}$ on the three reconstruction planes. (Middle) distribution of $\cos \theta_{12}$ on the three reconstruction planes. (Bottom) distribution of $\cos \theta_{23}$ on the three reconstruction planes. The bins are 0.05 wide.

As explained in Subsection 4.2.1, for the "Gran Sasso" algorithm the parameter σ_{3P} quantifies the uncertainty on the hit position by measuring for each point the dispersion δ_{3P} along the drift direction, and is proportional to the RMS of the δ_{3P} distribution. Such single point resolution is not a constant, but depends on the quality of reconstruction of each muon track and on the orientation of the track — since δ_{3P} is computed along the drift direction. It is possible as well to compute the average of σ_{3P} over the different views, which is the one used for the 3D version of "Gran Sasso" algorithm. The σ_{3P} distributions are shown in Figure 5.4.

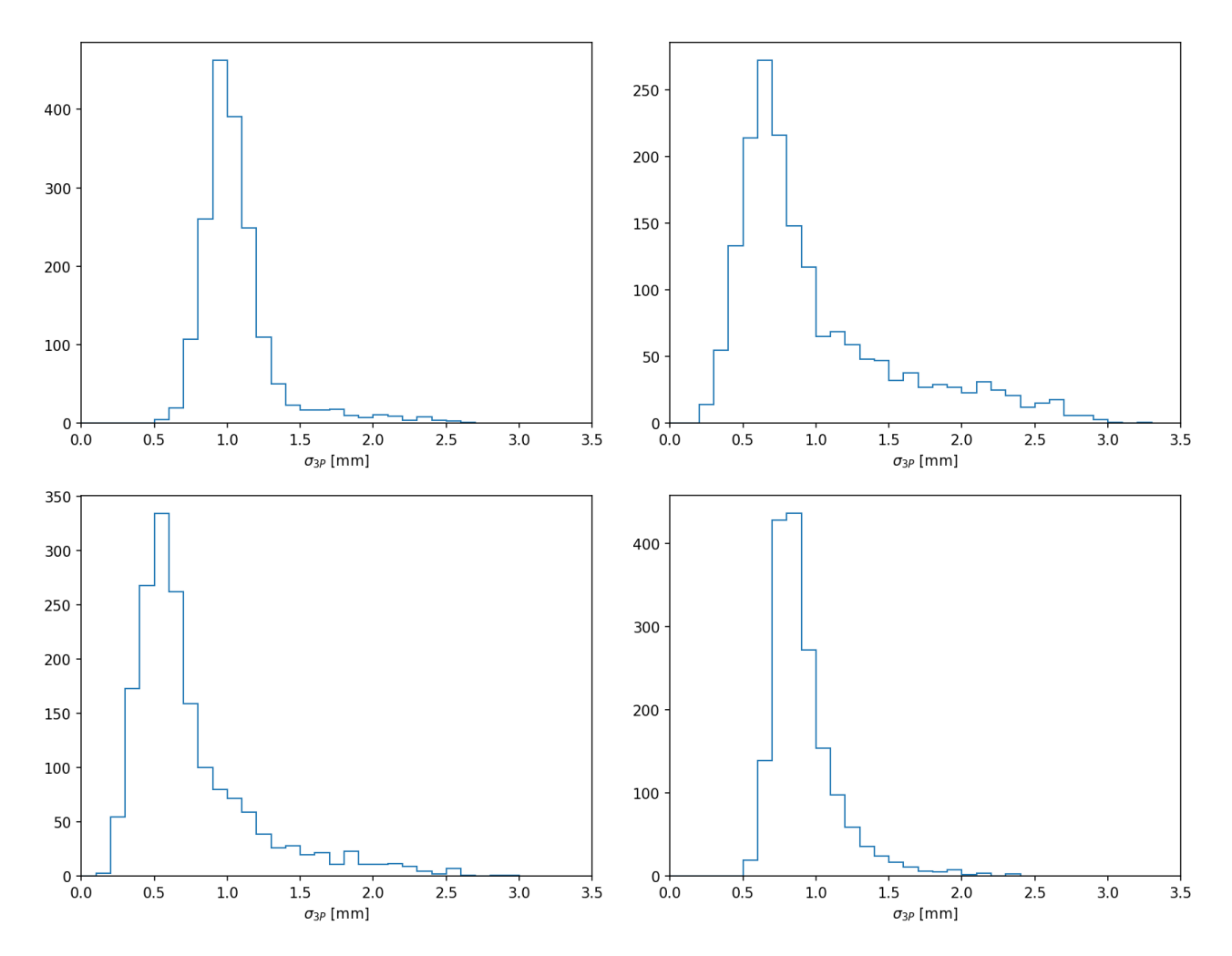


Figure 5.4: (Top left) σ_{3P} distribution in the Induction-1 plane. (Top right) σ_{3P} distribution in the Induction-2 plane. (Bottom left) σ_{3P} distribution in the Collection plane. (Bottom right) distribution of the average of σ_{3P} over the different views. The bins are 0.1 mm wide.

The most probable values (MPV) for these distributions are 0.95 mm for the Induction-1 plane, 0.65 mm for the Induction-2 plane, 0.55 mm for the Collection plane, and 0.85 mm for the σ_{3P} averaged over the three planes. According to Equation (4.9), for average values of $n_{\rm hit} \sim 30$, this corresponds to an angular resolution of the order of $\theta_{3P} \sim 2$ mrad.

Note that the plots in Figure 5.3 for each reconstruction plane do not refer to the total sample of 2072 tracks, but only to the subsample of tracks which has a sufficient number of hits in that specific plane for a MCS fit to be performed. This subsample is defined as the one with

tracks which have at least 3 hits per 14 cm segment and 30 hits in total in the chosen reconstruction plane. Another subsample of tracks can be defined, with only tracks that fulfill such requirements in all planes. The numbers of tracks in these subsamples are reported in Table 5.1.

total number of MC tracks of the sample	2072
number of valid MC tracks in Induction-1 view	1786
number of valid MC tracks in Induction-2 view	1772
number of valid MC tracks in Collection view	1794
number of valid MC tracks in all views	1721

Table 5.1: Total number of MC tracks of the sample, numbers of valid MC tracks in each of the three reconstruction planes, and number of valid MC tracks simultaneously in all reconstruction planes.

Only portions of track that belong to a single TPC have been considered, in order to evaluate the performance of MCS algorithm in a single geometrical frame. Making the algorithm able of performing the fit on tracks with hits belonging to different TPCs is currently in development.

5.2 "Gran Sasso" algorithm performance

The performance of the "Gran Sasso" algorithm, originally developed at Gran Sasso to work on the Collection plane only and extended here to the other reconstruction planes (Induction-1 and Induction-2) is shown in Figure 5.5. The scatter plot in Figure 5.5 (left) shows the comparison between $p_{\rm range}$ and $p_{\rm MCS}$, the histogram in Figure 5.5 (right) shows the distribution of $p_{\rm range}/p_{\rm MCS}-1$. The dominant error in the $p_{\rm range}/p_{\rm MCS}$ ratio comes from $p_{\rm MCS}$, as it is the less precise measurement of the two, and a Gaussian behavior in 1/p is expected due to the Highland formula, as described in Section 4.1. Therefore, by displaying the distribution of $p_{\rm range}/p_{\rm MCS}-1$, so that in this way it is peaked at zero, we would ideally expect a Gaussian distribution. As can be seen in Figure 5.5, the comparison between $p_{\rm MCS}$ and $p_{\rm range}$ for our sample of stopping muon tracks shows a fair agreement, even with a large uncertainty.

The efficiency ε of the algorithm applied in a specific plane is defined here as the ratio between the number of tracks which have a physical value of p_{MCS} and the number of all valid tracks in the chosen plane as reported in Table 5.1. For tracks with a physical value of p_{MCS} , we refer to those tracks with $p_{\text{MCS}} > p_{\text{low}}$ and $p_{\text{MCS}} < p_{\text{high}}$. The lower limit p_{low} is the minimum allowable momentum — and changes for each track — since the energy of the j-th segment, computed according to the energy loss upstream of the segment, must remain positive — see Subsection 4.2. The upper limit p_{high} is an arbitrary value — constant for all tracks — chosen as $1.5 \,\text{GeV} \,\text{c}^{-1}$ to avoid selecting tracks with an unrealistically large reconstructed momentum. The efficiencies ε for each plane are reported in Table 5.2.

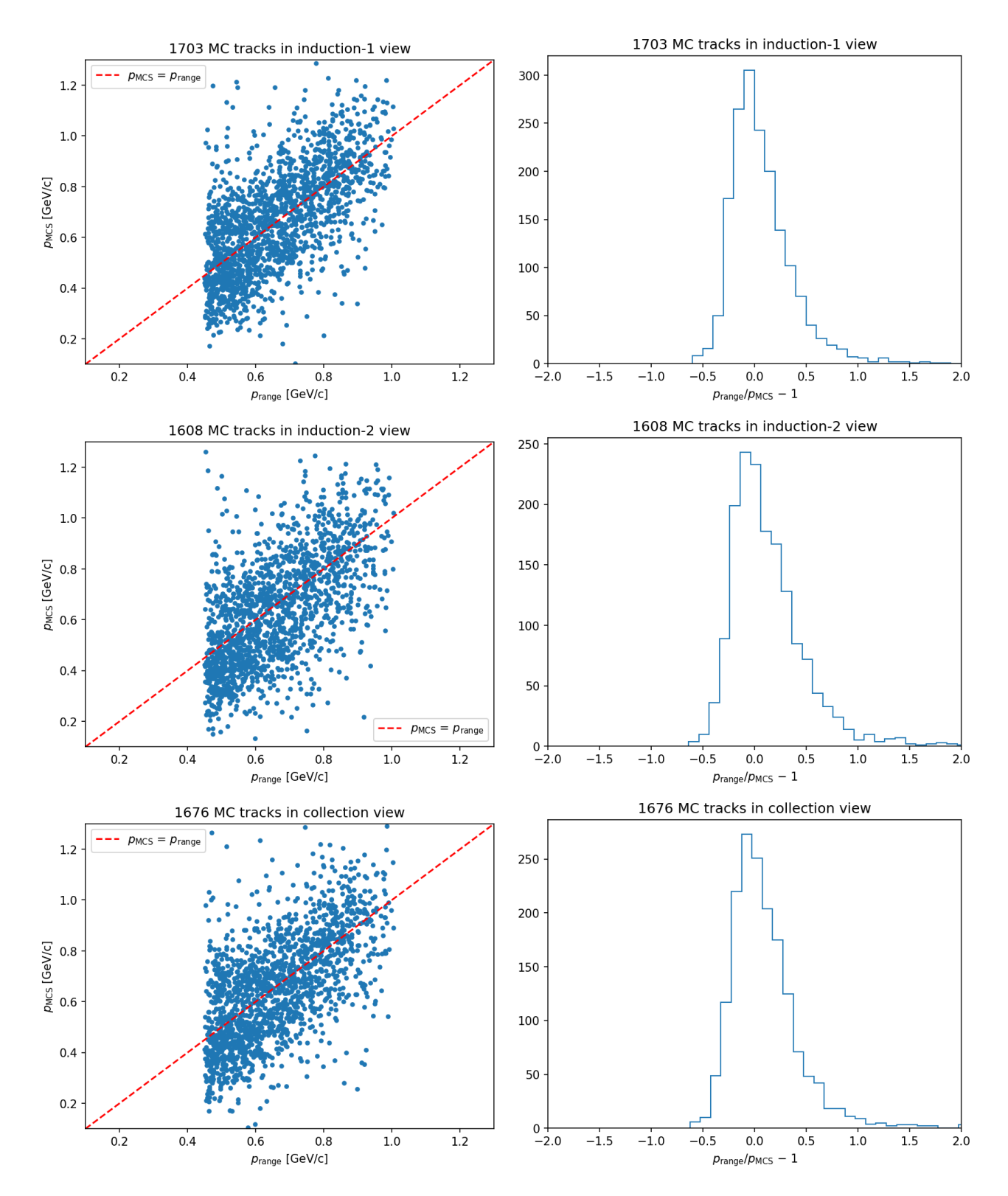


Figure 5.5: (Left) scatter plots of p_{MCS} versus p_{range} ; the red lines represent $p_{\text{MCS}} = p_{\text{range}}$. (Right) distributions of $p_{\text{range}}/p_{\text{MCS}} - 1$, in bins of 0.1. Top plots, middle plots and bottom plots refer to the Induction-1, Induction-2 and Collection plane, respectively.

	Induction-1	Induction-2	Collection
number of valid MC tracks in the plane	1786	1772	1794
number of valid MC tracks with physical $p_{\rm MCS}$	1703	1608	1676
efficiency ε	95%	91%	93%

Table 5.2: Number of valid MC tracks in each of the three reconstruction planes, number of valid MC tracks with physical p_{MCS} and efficiency ε .

I made a profile of these data with respect to range momentum p_{range} , by grouping our sample into bins of width $100 \,\text{MeV}\,\text{c}^{-1}$, with the only exception of the last bin $0.8 - 1.0 \,\text{GeV}\,\text{c}^{-1}$ with a width of $200 \,\text{MeV}\,\text{c}^{-1}$, because of the scarce statistics available in the range $0.9 - 1.0 \,\text{GeV}\,\text{c}^{-1}$.

The two relevant quantities in the profile are the bias and the resolution. The bias quantifies the average difference between p_{MCS} and p_{range} , and is defined as $p_{\text{MCS}}/p_{\text{range}} - 1$. If the bias is positive, it means the algorithm has overestimated p_{MCS} on average with respect to p_{range} ; viceversa, if the bias is negative, it means the algorithm has underestimated p_{MCS} on average with respect to p_{range} . For each bin, to prevent tails from influencing the computation of the resolution, I performed a fit of the distribution $p_{\text{range}}/p_{\text{MCS}} - 1$ with a Gaussian distribution, and the best-fit curve was used to extract the best value of the mean μ , together with its associated uncertainty $\delta\mu$. The bias and the mean μ are related by

$$\mu = \frac{p_{\text{range}}}{p_{\text{MCS}}} - 1 \bigg|_{\text{best-fit}} \quad \Rightarrow \quad \text{bias} = \frac{p_{\text{MCS}}}{p_{\text{range}}} - 1 = \frac{1}{\mu + 1} - 1 \tag{5.4}$$

and therefore the uncertainty associated to the bias is propagated from the uncertainty $\delta\mu$ as

$$\delta \text{bias} = \frac{1}{(\mu + 1)^2} \delta \mu \tag{5.5}$$

The resolution quantifies the width of the distribution and is obtained as the best value of σ from the same Gaussian fit. The resulting bias and resolution are shown in Figure 5.6 for the three reconstruction planes, while a visual example of this procedure for the Collection view is shown in Figure 5.7.

In the three planes, overall, the bias does not appear to deviate significantly from zero. A small negative bias of about 5-7% is observed in the Induction-2 plane at low momentum. The resolution is at the level of 30% in Induction-1, 31% in Induction-2, 34% in Collection plane at low momentum ($p_{\text{range}} \in 0.4 - 0.5 \,\text{GeV}\,\text{c}^{-1}$), and at the level of 16% in Induction-1, 17% in Induction-2, 14% in Collection plane at high momentum ($p_{\text{range}} \in 0.8 - 1.0 \,\text{GeV}\,\text{c}^{-1}$).

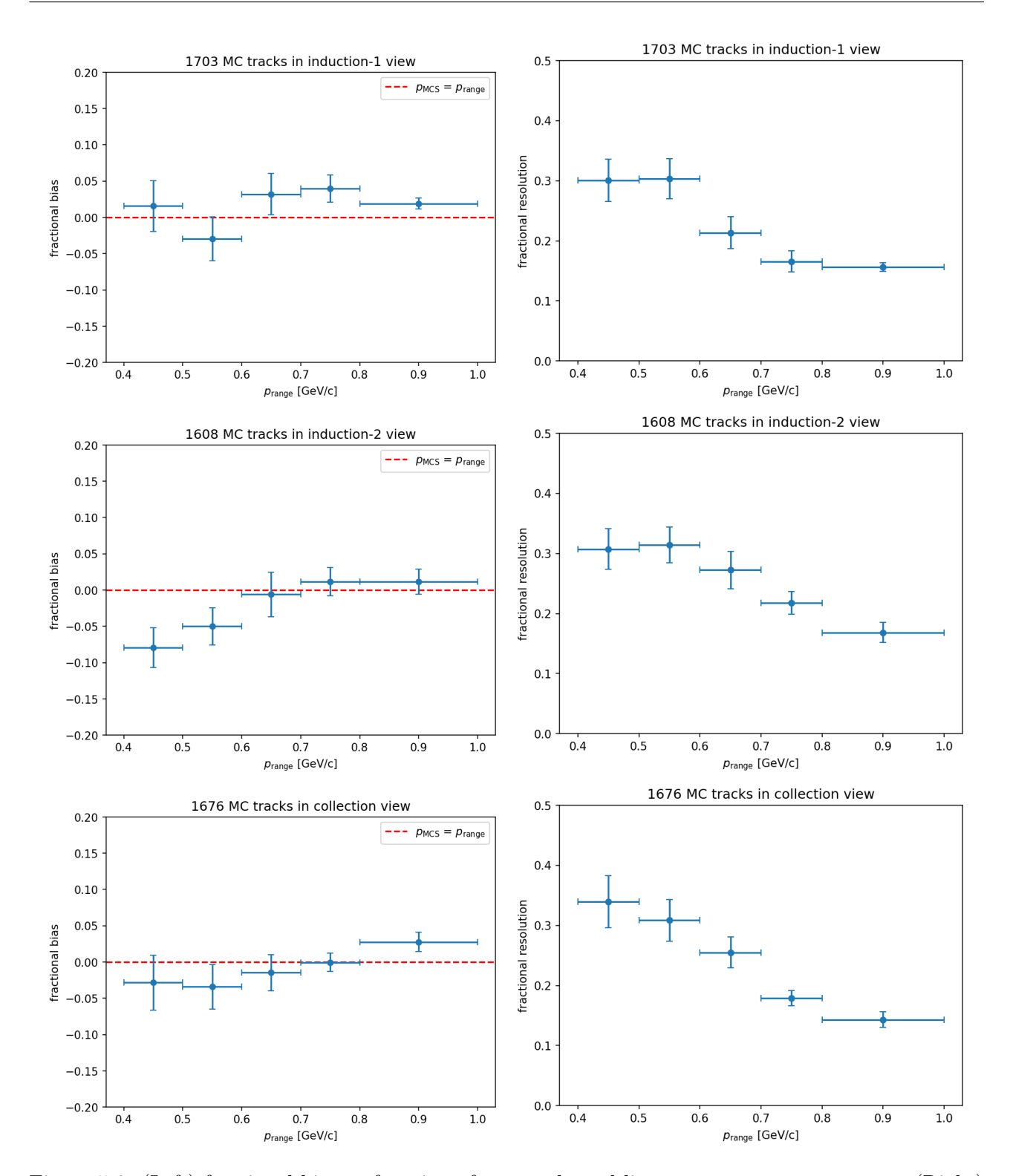


Figure 5.6: (Left) fractional bias as function of p_{range} ; the red lines represent $p_{\text{MCS}} = p_{\text{range}}$. (Right) fractional resolution as function of p_{range} . Top plots, middle plots and bottom plots refer to the Induction-1, Induction-2 and Collection plane, respectively.

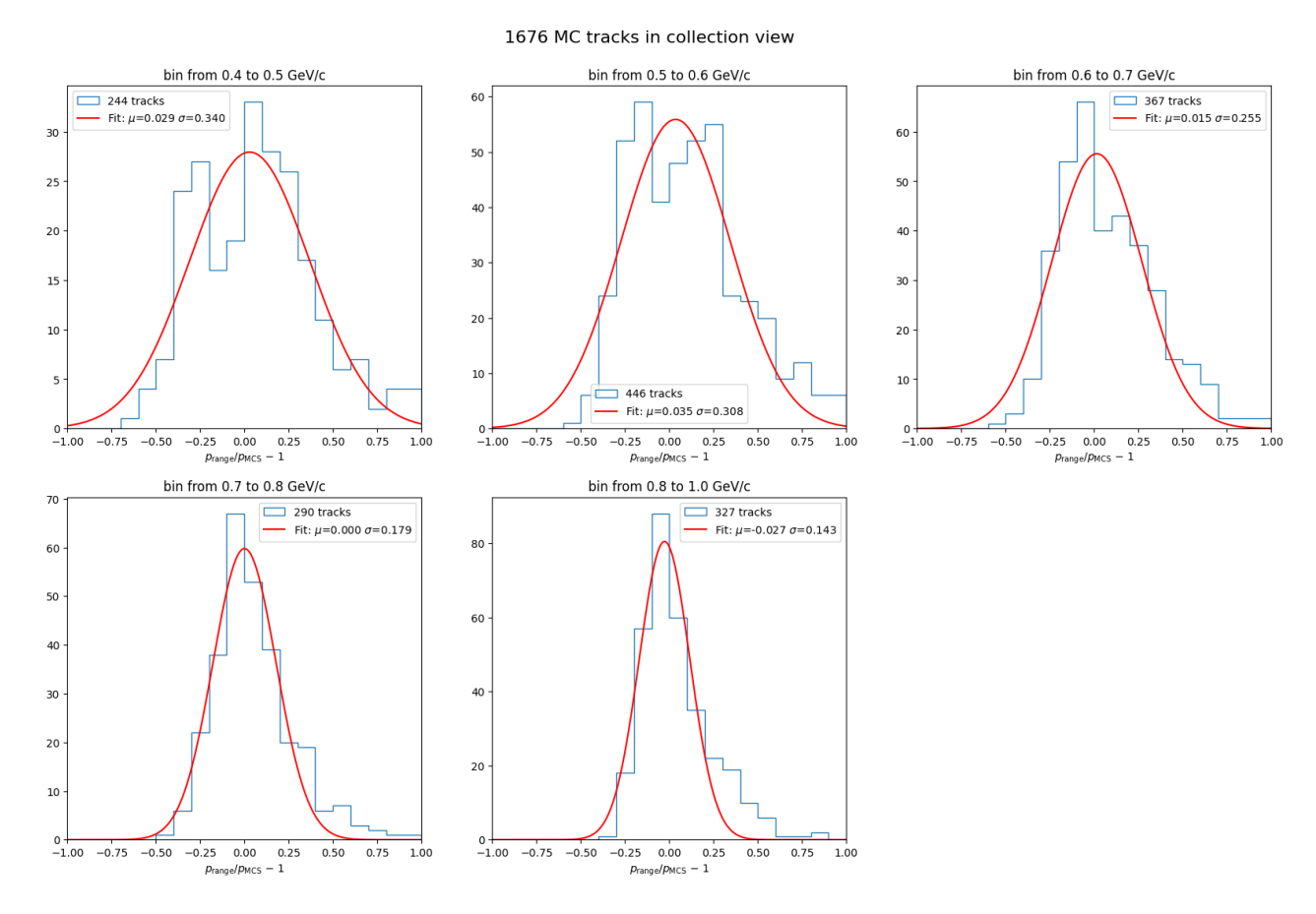


Figure 5.7: Distributions of $p_{\text{range}}/p_{\text{MCS}}-1$ in the Collection plane, in bins of 0.1. The five distributions are relative to the five p_{range} intervals. The red curves represent the Gaussian fit.

The resolution improves as $p_{\rm range}$ increases. This is expected because the resolution depends on the number of segments $n_{\rm seg}$: the longer the track, the larger the number of segments and thus the number of angles, leading to a better calculation of the C_2 function. The results obtained in the Collection plane is compatible with what was observed in previous studies [115]. However, it must be accounted that the resolution has also a dependence on p^2 , as stated in Equation (4.15): this implies that the resolution gets worse as p increases, given that $n_{\rm seg}$ stays constant. It would be interesting to disentangle these two effects by studying the $p_{\rm MCS}$ reconstruction using the same length for all tracks — or, in other words, setting a constant number of segments $n_{\rm seg}$. A "Gran Sasso" algorithm version able of reconstructing muon momentum from a fixed length of track is being developed.

5.2.1 Combining the Collection plane with other planes

We know that the Collection plane has the best signal-to-noise ratio — see Subsection 2.2.1 — however, incorporating information from the Induction planes can enhance the reconstruction by providing complementary measurements. To leverage the full potential of the reconstruction, we attempted to improve the performance of the "Gran Sasso" algorithm by combining the p_{MCS} measurement from 2D hits in the Collection plane with the corresponding measurement from 2D

hits in either Induction-1 or Induction-2 planes, or both. Figure 5.8 illustrates the correlation between the momentum p_{MCS} reconstructed from the Collection plane and the momentum p_{MCS} reconstructed from the Induction planes.

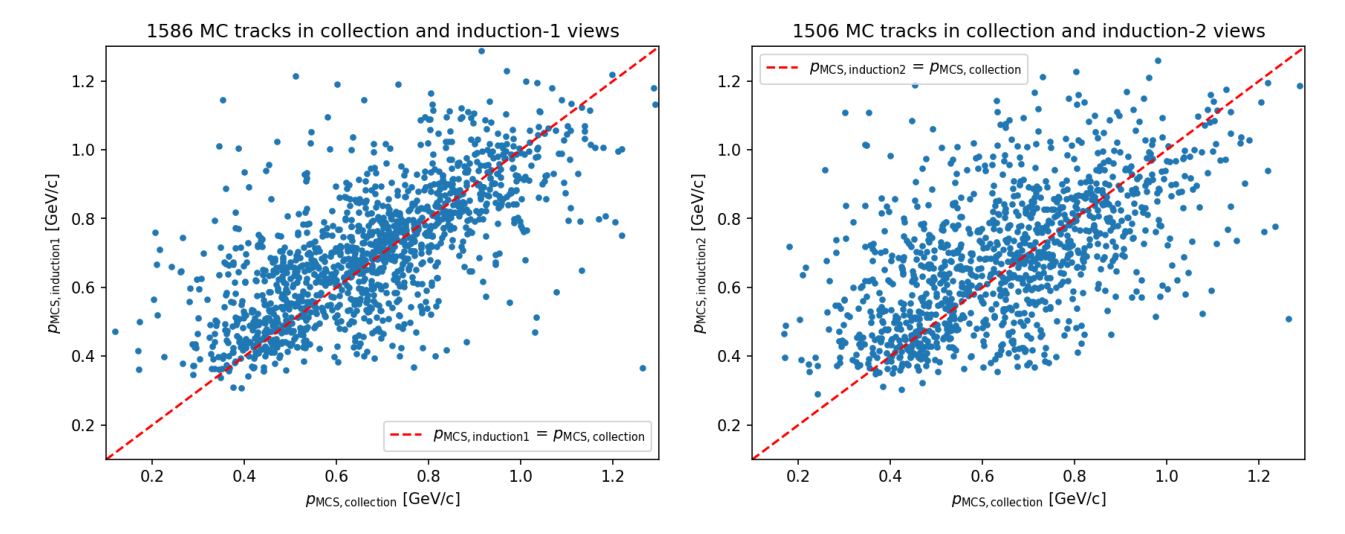


Figure 5.8: (Left) scatter plot of p_{MCS} as measured in the Collection plane versus p_{MCS} as measured in the Induction-2 plane. (Right) scatter plot of p_{MCS} as measured in the Collection plane versus p_{MCS} as measured in the Induction-1 plane.

The correlation coefficient is found to be 0.52 in the case of $Collection \oplus Induction-2$ planes and 0.71 in the case of $Collection \oplus Induction-1$ planes. The momentum p_{MCS} reconstructed in the Induction-1 and Induction-2 planes appears thus partially — but not completely — correlated to the momentum p_{MCS} reconstructed in the Collection plane. Therefore, starting from valid tracks in the Collection plane, it is possible to:

- use the information from Induction-2 plane, for tracks valid not only in the Collection plane but also in the Induction-2 plane, by computing the average of the two reconstructed momenta p_{MCS} in the two different planes (Collection \oplus Induction-2);
- in a similar way, for tracks valid in the Collection and Induction-1 planes, compute the average of the two p_{MCS} measured in the two planes (Collection \oplus Induction-1);
- for tracks valid in all the planes, compute the average of the three p_{MCS} measured in the three planes ($Collection \oplus Induction-2 \oplus Induction-1$);

Combining different planes allows to maximize the information contained in the input: for example, by recovering inefficiencies in a particular view due to reconstruction errors, delta rays, or geometric reasons — such as a track being nearly parallel to the wires of a plane. The partial (but not perfect) correlation between p_{MCS} across different planes indicates that the random effect of measurement errors can be reduced, enhancing the MCS effect. Figure 5.9 shows the scatter plots of p_{range} versus p_{MCS} and the distributions of $p_{\text{range}}/p_{\text{MCS}} - 1$, for the three cases.

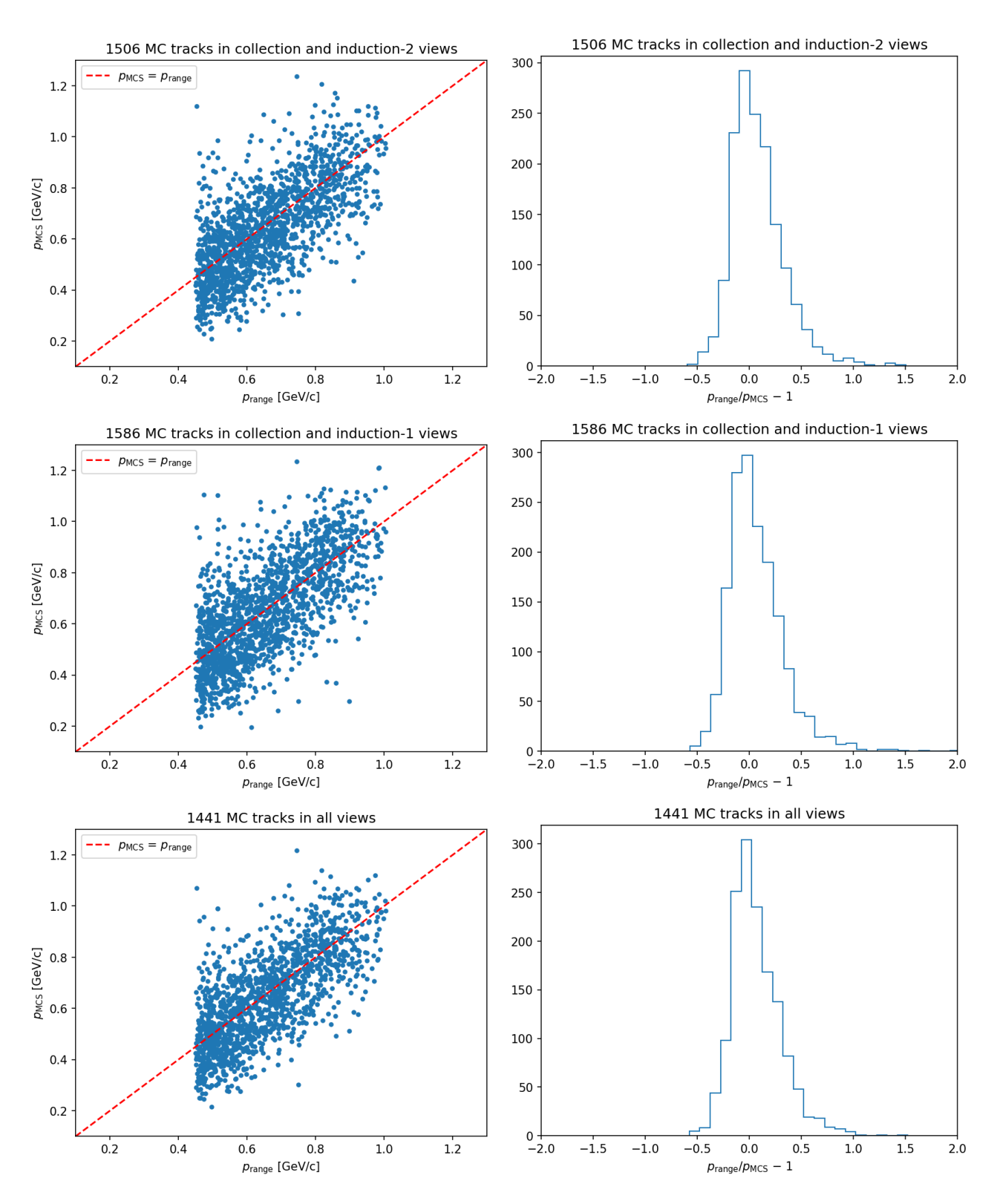


Figure 5.9: (Left) scatter plots of p_{MCS} versus p_{range} ; the red lines represent $p_{\text{MCS}} = p_{\text{range}}$. (Right) distributions of $p_{\text{range}}/p_{\text{MCS}} - 1$, in bins of 0.1. Top plots, middle plots and bottom plots refer to the $Collection \oplus Induction-2$ planes, to the $Collection \oplus Induction-1$ planes, and to the $Collection \oplus Induction-2 \oplus Induction-1$ planes, respectively.

Figure 5.10 shows the fractional bias and resolution for the three cases, as extracted from the scatter plots following the same procedure described in Section 5.2.

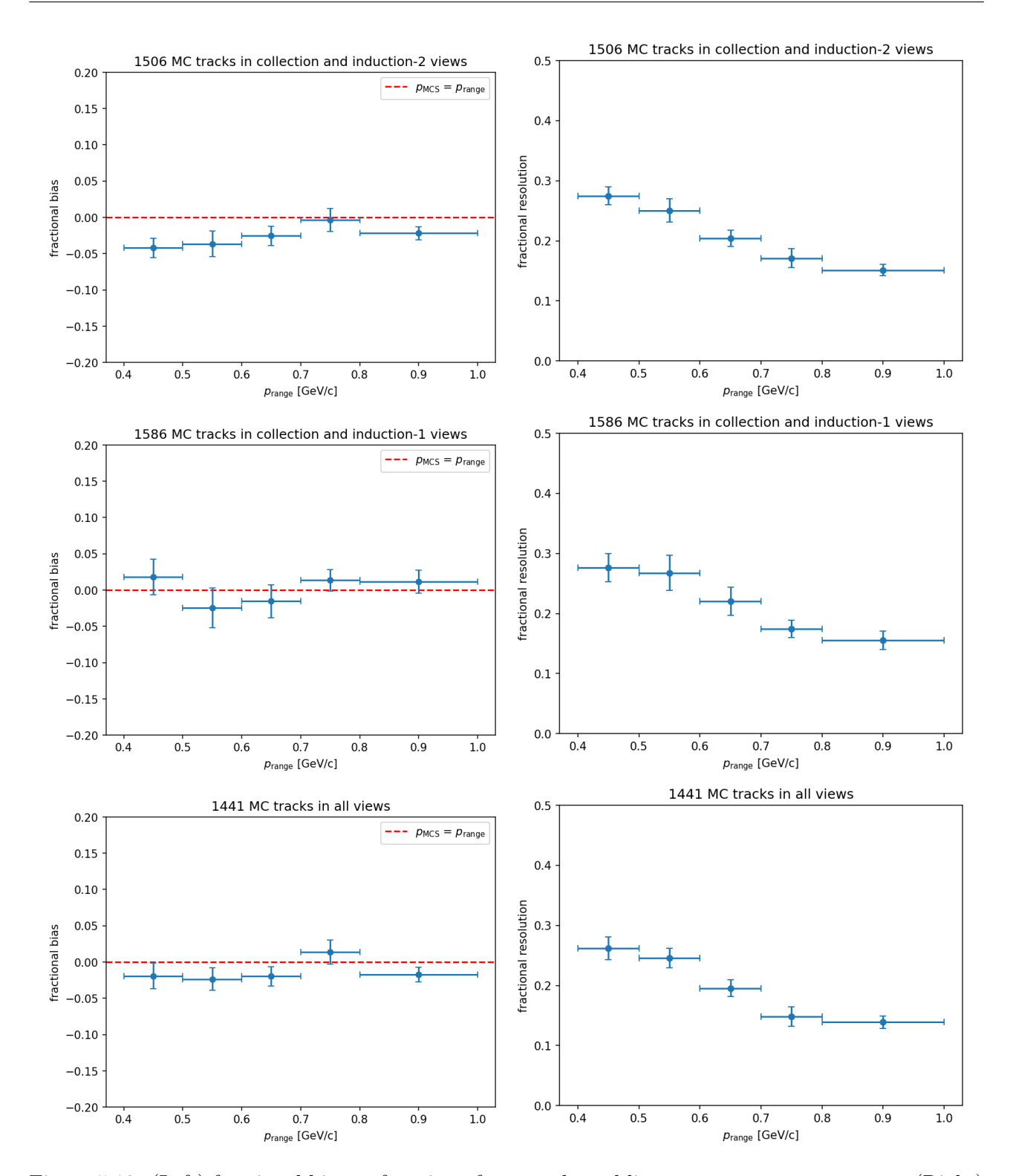


Figure 5.10: (Left) fractional bias as function of $p_{\rm range}$; the red lines represent $p_{\rm MCS} = p_{\rm range}$. (Right) fractional resolution as a function of $p_{\rm range}$. Top plots, middle plots and bottom plots refer to the Collection \oplus Induction-2 planes, to the Collection \oplus Induction-1 planes, respectively.

There is an improvement of the bias and the resolution. The combination of two or three views minimized the fractional bias. The resolution, from 32% at low momentum and 16% at high momentum in a single view, is now at the level of 26% at low momentum and 14% at high momentum with all the views combined.

5.2.2 Extension to 3D for the "Gran Sasso" algorithm

The performance of the 3D version of the "Gran Sasso" algorithm is shown in Figure 5.13 with the scatter plot of p_{range} versus p_{MCS} , the distribution of $p_{\text{range}}/p_{\text{MCS}} - 1$ for all tracks and the distributions of $p_{\text{range}}/p_{\text{MCS}} - 1$ for the five intervals of p_{range} considered.

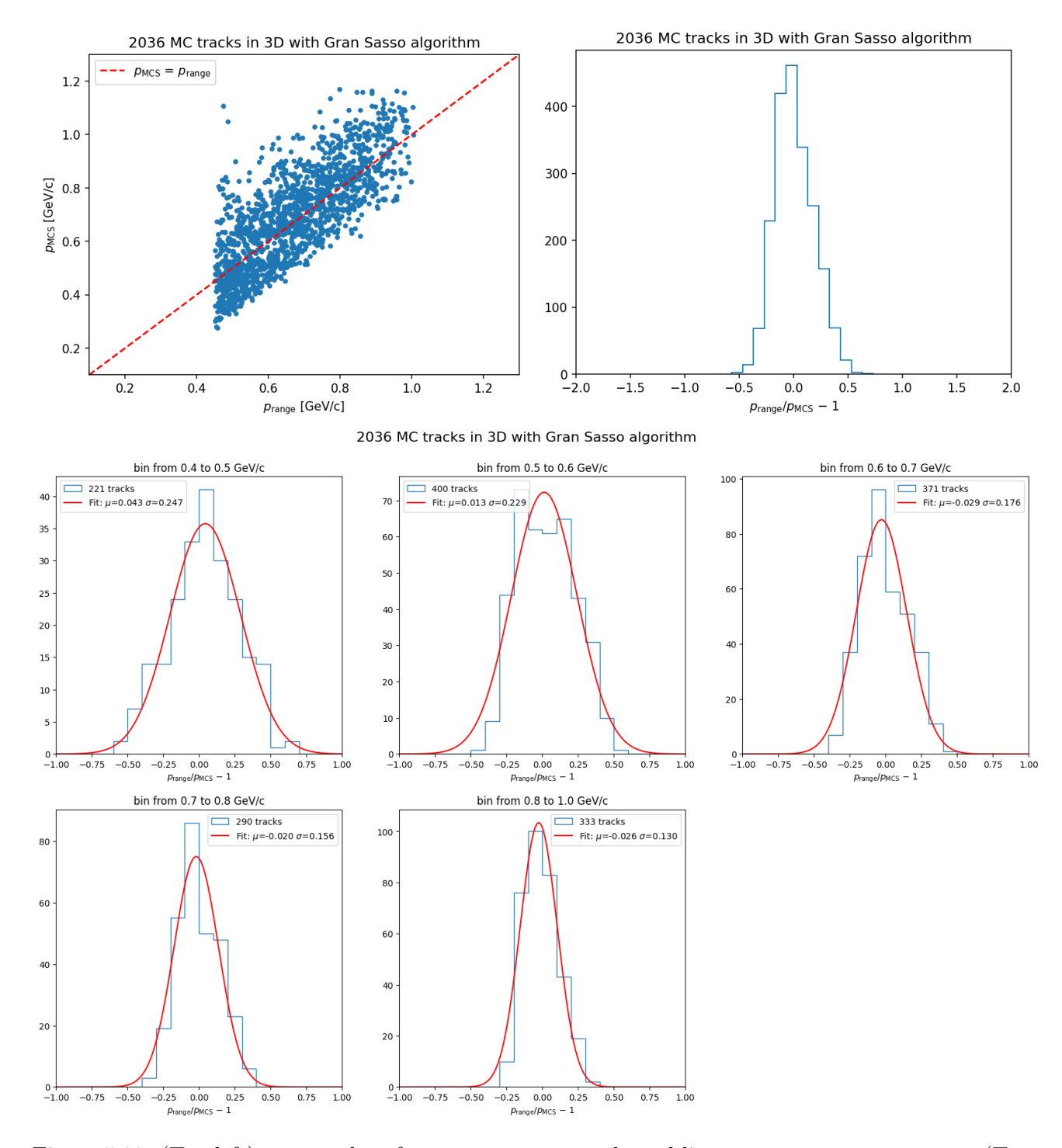


Figure 5.11: (Top left) scatter plot of p_{MCS} versus p_{range} ; the red line represents $p_{\text{MCS}} = p_{\text{range}}$. (Top right) distribution of $p_{\text{range}}/p_{\text{MCS}}-1$, in bins of 0.1. (Bottom) distributions of $p_{\text{range}}/p_{\text{MCS}}-1$ for the five p_{range} intervals, in bins of 0.1; the red curves represent the Gaussian fits.

The efficiency ε of the 3D "Gran Sasso" algorithm, just as defined for the 2D version of the algorithm, is summarized in Table 5.3.

number of valid MC tracks	2072
number of valid MC tracks with physical p_{MCS}	2036
efficiency ε	98%

Table 5.3: Number of valid MC tracks, number of valid MC tracks with physical p_{MCS} and efficiency ε for the 3D version of the "Gran Sasso" algorithm.

Figure 5.12 shows the p_{MCS} bias and resolution for the 3D version of the "Gran Sasso" algorithm, as extracted from the scatter plots used the same procedure described in the previous subsection.

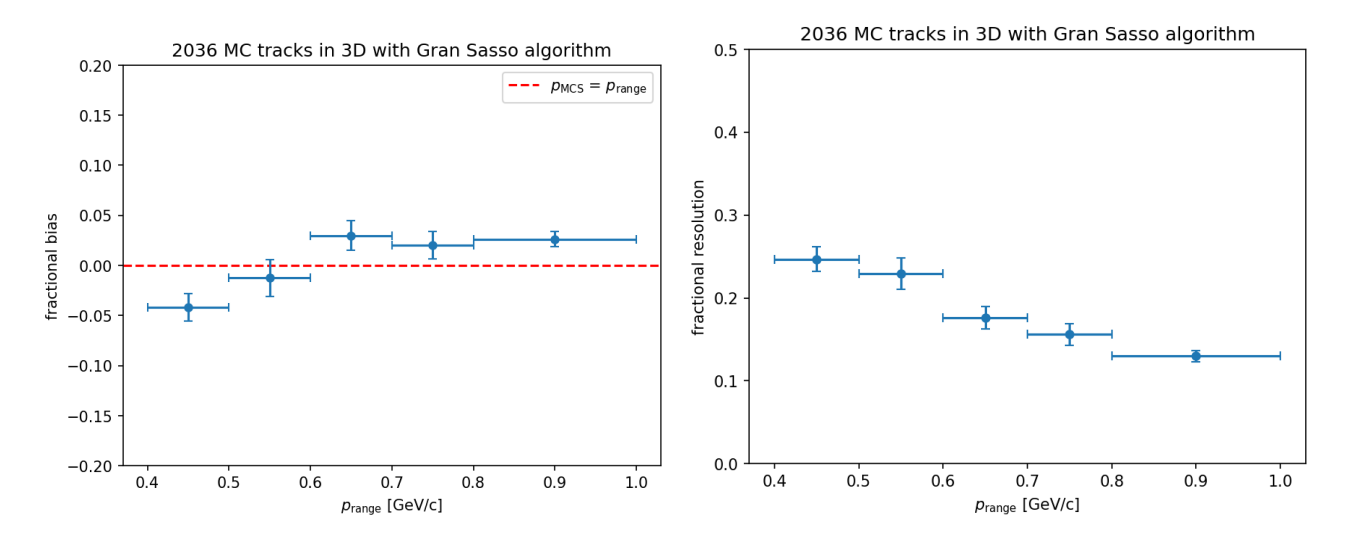


Figure 5.12: (Left) fractional bias as a function of p_{range} ; the red line represents $p_{\text{MCS}} = p_{\text{range}}$. (Right) fractional resolution as a function of p_{range} .

In the 3D version of the algorithm, p_{MCS} shows a small positive bias at high momentum and a small negative bias at low momentum. The resolution is at the level of 25% at low momentum and 13% at high momentum, slightly better than the resolution obtained combining all the views – see Subsection 5.2.1.

5.3 "MicroBooNE" algorithm performance

The performance of the "MicroBooNE" algorithm, originally developed by the MicroBooNE Collaboration and tested here with ICARUS events, is shown in Figure 5.13 with the scatter plot of $p_{\rm range}$ versus $p_{\rm MCS}$, the distribution of $p_{\rm range}/p_{\rm MCS}-1$ for all tracks and the distributions of $p_{\rm range}/p_{\rm MCS}-1$ for the five intervals of $p_{\rm range}$ considered.

The efficiency ε of the "MicroBooNE" algorithm, using the same definition as for the 3D version of the "Gran Sasso" algorithm, is summarized in Table 5.4.

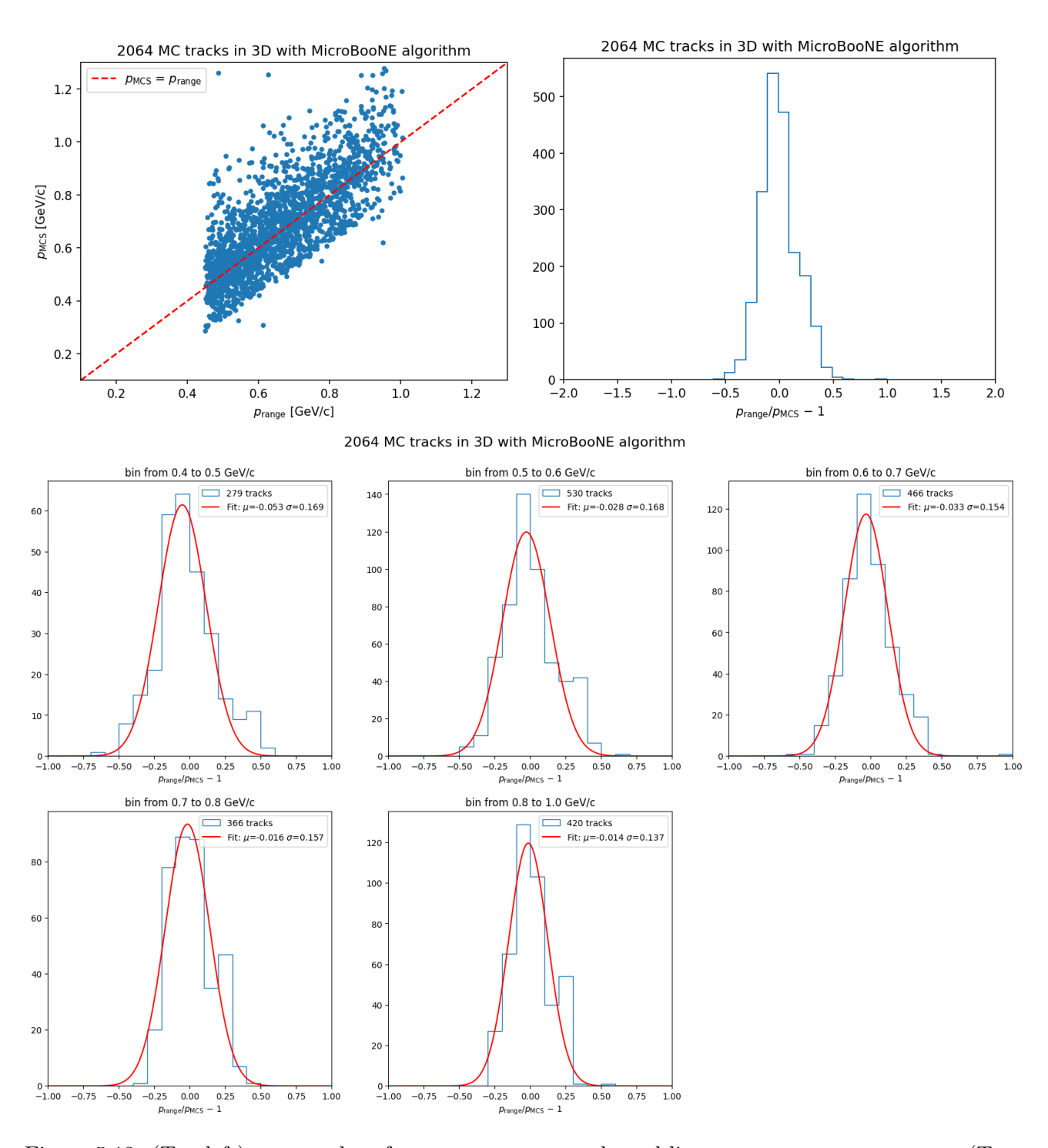


Figure 5.13: (Top left) scatter plot of p_{MCS} versus p_{range} ; the red line represents $p_{\text{MCS}} = p_{\text{range}}$. (Top right) distribution of $p_{\text{range}}/p_{\text{MCS}} - 1$, in bins of 0.1. (Bottom) distributions of $p_{\text{range}}/p_{\text{MCS}} - 1$ for the five p_{range} intervals, in bins of 0.1; the red curves represent the Gaussian fits.

number of valid MC tracks	2072
number of valid MC tracks with physical p_{MCS}	2064
efficiency ε	100%

Table 5.4: Number of valid MC tracks, number of valid MC tracks with physical p_{MCS} and efficiency ε for the "MicroBooNE" algorithm.

Figure 5.14 shows the p_{MCS} bias and resolution for the "MicroBooNE" algorithm, as extracted from the scatter plots used the same procedure described in the previous section.

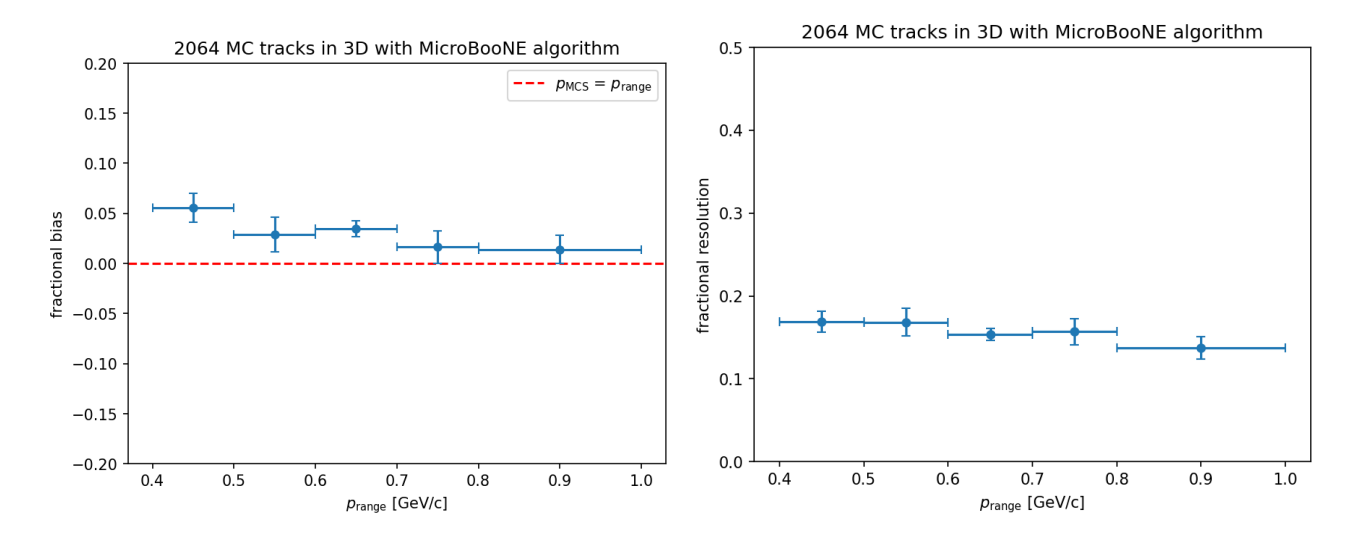


Figure 5.14: (Left) fractional bias as a function of p_{range} ; the red line represents $p_{\text{MCS}} = p_{\text{range}}$. (Right) fractional resolution as a function of p_{range} .

There is a small and flat positive bias over the whole range of momentum, while the resolution ranges from about 17% at low momentum to about 14% at high momentum.

5.4 Results of analysis on MC muon tracks

The analysis of MC stopping muon tracks has provided a detailed evaluation of the MCS-based momentum estimation algorithms applied to the ICARUS events. The "Gran Sasso" algorithm, originally developed for the Collection plane, was successfully extended to the Induction-1 and Induction-2 planes, and a 3D version was developed. The "MicroBooNE" algorithm was also tested in this context. Overall, the "Gran Sasso" algorithm in the three reconstruction views shows reasonable agreement between p_{MCS} and p_{range} , with a slight negative bias in Induction-2 at low momentum and a resolution improving from 32% at low momentum to 16% at high momentum. Combining different views helped mitigate statistical fluctuations and successfully maximize the information taken from the input, improving both bias and resolution. The 3D version exhibits a comparable performance to the combined 2D views, allowing the use of either one depending on the needs. The "MicroBooNE" algorithm displays a small, nearly constant positive bias across all p_{range} ranges and a better resolution at lower momenta compared to the "Gran Sasso" algorithm. These results confirm the validity of MCS momentum estimation for simulated stopping muons in ICARUS, while also highlighting areas for improvement. The observed biases and resolution trends suggest that systematic effects related to reconstruction and detector response should be further investigated, and this study needs to be extended to real data to compare MC simulated muon tracks with experimental real muon tracks.

Chapter 6

MCS analysis on real muon tracks

In this chapter, we used a sample of real cosmic muons to check the performance of the "Gran Sasso" and the "MicroBooNE" algorithms, according to the experimental conditions of ICARUS at FNAL. We do not have the "true" momentum for real cosmic stopping muons, as we have in Monte Carlo, and we will thus use $p_{\rm range}$ in the same way we did for MC stopping cosmic muons. We will compare $p_{\rm range}$ to $p_{\rm MCS}$ to evaluate the performance of the MCS-based momentum estimation method on real muon tracks.

The experimental data sample is the single run 9435: this run is used as reference for many studies at the reconstruction, selection and scanning. Run 9435 has been collected during the Run-2 period on January 29-30, 2023 with a duration of 25 hours and it corresponds to about 15000 events collected with a BNB majority trigger — details can be found in Section 2.2. The selection cuts applied to find real stopping cosmic muons were the same as for finding simulated stopping cosmic muons. Unlike MC tracks, no real tracks were found with inverted reconstructed starting and ending points.

We know that the MCS-based momentum estimation method relies on an accurate trajectory reconstruction, and any detector effect that distorts the hit position reconstruction affects the performance of the momentum estimation. In ICARUS, there are known issues in some well identified regions of the TPC, such as electric field distortions caused near the cathode due to its non-perfectly planarity, which have not yet been simulated in the Monte Carlo models. In order to prevent such effects from biasing the performance of the algorithms on real muons, there is a detector volume fiducialization to exclude these known regions: any hit point closer than 15 cm to the cathode was not considered for the measurement of the scattering angles.

Similarly to what was done in the previous chapter for simulated tracks, in this case as well, to simulate the application of the algorithms to non-stopping tracks, the last three angles - i.e. the last four segments - were excluded from the C_2 function calculation, for the "Gran Sasso" algorithm, and from the likelihood calculation, for the "MicroBooNE" algorithm. This roughly corresponds to discarding the last $\sim 50\,\mathrm{cm}$ of the track.

6.1 Characterization of the muon sample

The sample of real stopping muons includes 1859 tracks with momentum between $0.45\,\mathrm{GeV}\,\mathrm{c}^{-1}$ and $1\,\mathrm{GeV}\,\mathrm{c}^{-1}$. Figure 6.1 shows the distributions of track length L, range momentum p_{range} and cosine of the angles θ_x , θ_y , θ_z between the track direction and the three main directions x,y,z – respectively, the drift direction, the vertical direction, and the beam direction. Consistently with what will be shown later, and similarly to MC, in Figure 6.1 (top right) a distribution of p_{range} in bins of $100\,\mathrm{MeV}\,\mathrm{c}^{-1}$ is shown, grouping tracks with p_{range} between 0.8 and $1.0\,\mathrm{GeV}\,\mathrm{c}^{-1}$ into a single bin, given the lower statistics at higher momenta.

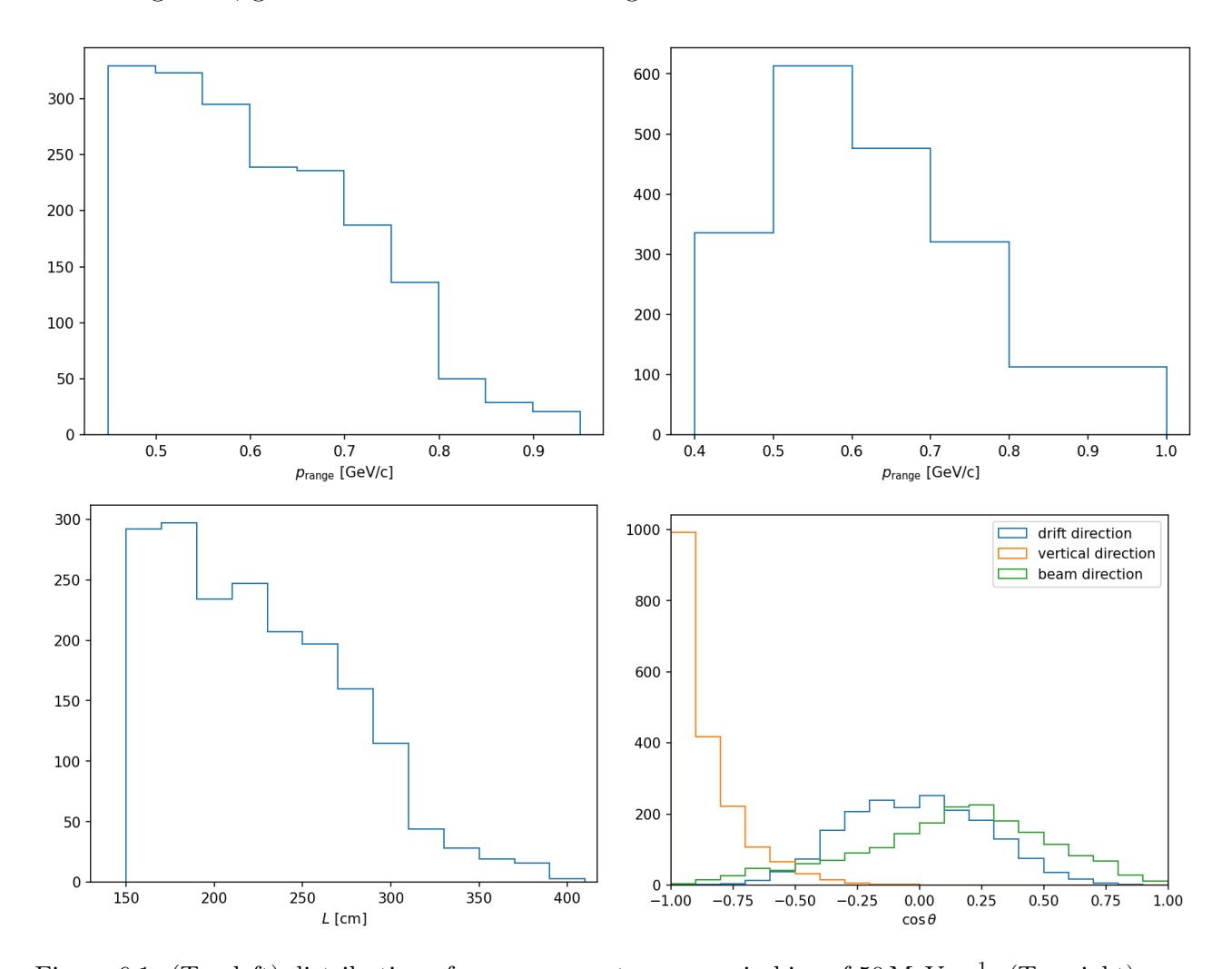


Figure 6.1: (Top left) distribution of range momentum p_{range} in bins of 50 MeV c⁻¹. (Top right) same distribution in bins of 100 MeV c⁻¹, except for the last bin which has a width of 200 MeV c⁻¹. (Bottom left) distribution of length L in bins of 25 cm. (Bottom right) distribution of $\cos \theta$ with respect to the three directions – drift direction x, vertical direction y, beam direction z – in bins of 0.1.

The angular distribution in Figure 6.1 (bottom right) shows that, while along the drift and the beam direction there is no preferred direction, along the vertical direction there is a peak in $\cos \theta_y = -1$ as expected by selecting downgoing cosmic muons, just as there was for MC tracks. Figure 6.2 shows the distributions of $\cos \theta_{13}$, $\cos \theta_{12}$, $\cos \theta_{23}$ as defined in the previous chapter.

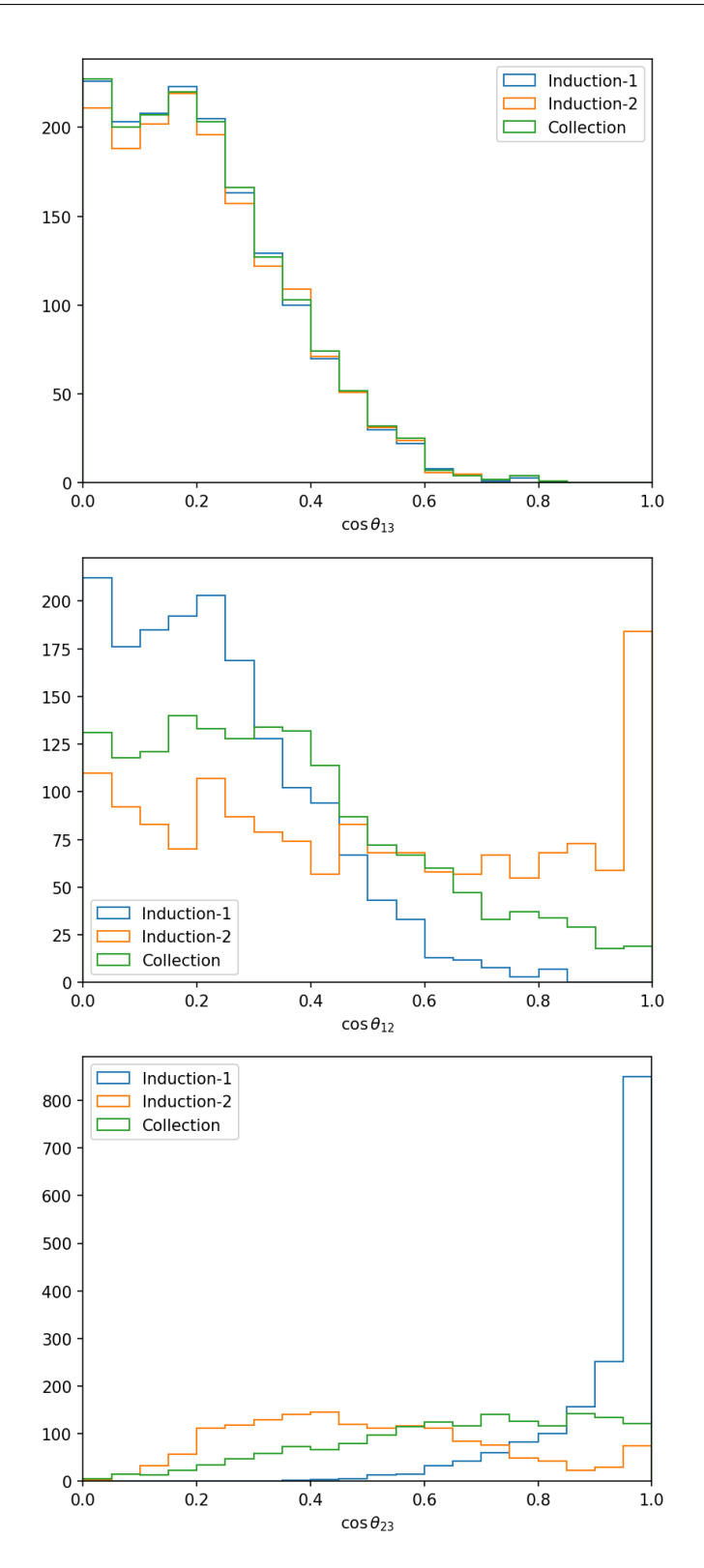


Figure 6.2: (Top) distribution of $\cos \theta_{13}$ on the three reconstruction planes. (Middle) distribution of $\cos \theta_{12}$ on the three reconstruction planes. (Bottom) distribution of $\cos \theta_{23}$ on the three reconstruction planes. The bins are 0.05 wide.

We made each distribution for each of the three reconstruction planes, Induction-1, Induction-2 and Collection, which have different orientations in space. Note that Induction-2 and Collection planes are expected to have similar distributions, since their wires are oriented at $\pm 60^{\circ}$ with respect to the horizontal direction – see Section 2.2.

Figure 6.2 shows that the trend of these distributions is identical to those relative to MC tracks, as can be seen in Figure 5.3, according to what we expect for our sample.

The σ_{3P} distributions are shown in Figure 6.3. Note that in Figure 6.3 (top right) there is a significant tail in the σ_{3P} distribution in the Induction-2 plane, extending up to $\sigma_{3P} = 2.5 \text{ mm}$, which is larger than the tail observed in the MC – see Figure 5.4.

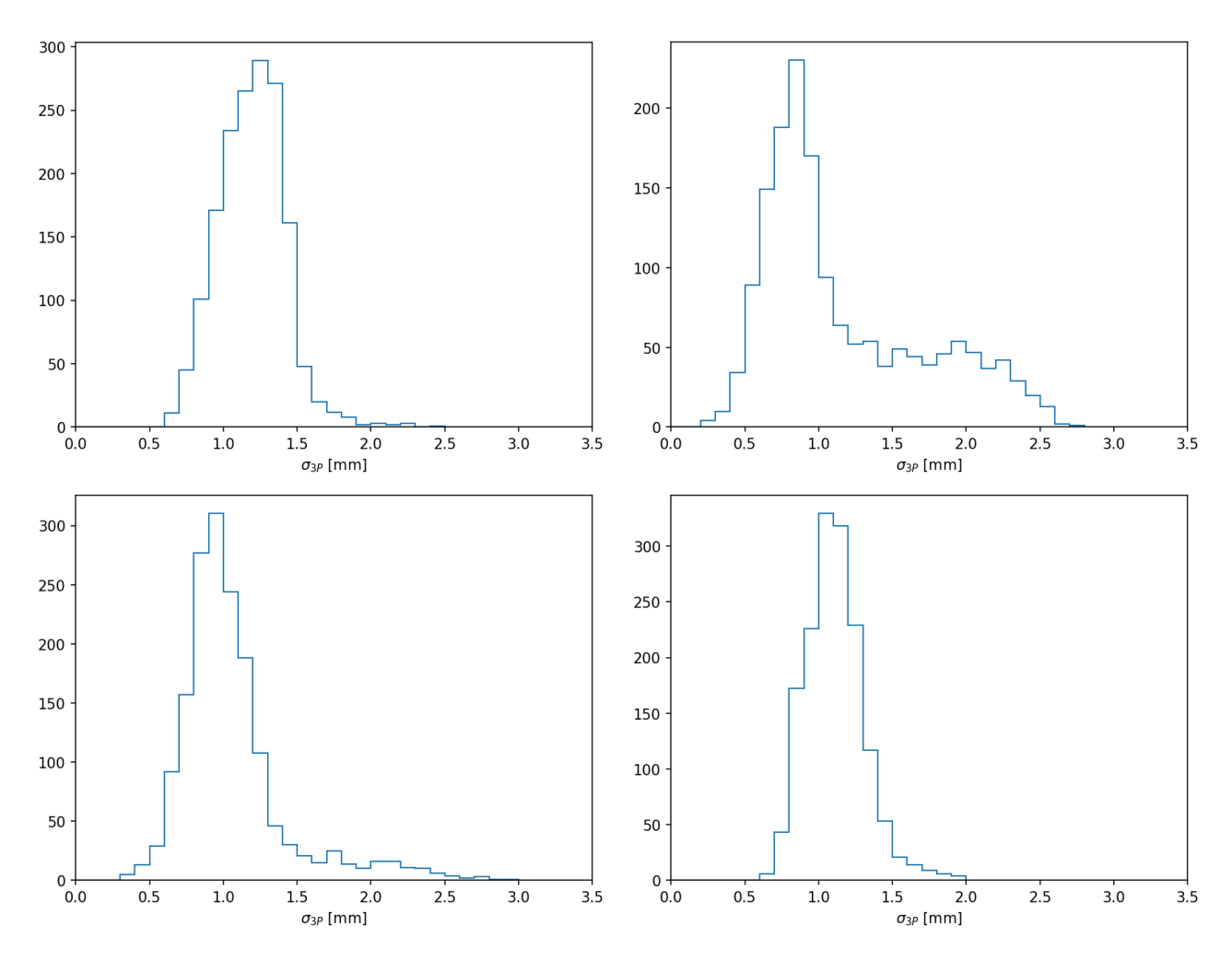


Figure 6.3: (Top left) σ_{3P} distribution in the Induction-1 plane. (Top right) σ_{3P} distribution in the Induction-2 plane. (Bottom left) σ_{3P} distribution in the Collection plane. (Bottom right) distribution of the average of σ_{3P} over the different views. The bins are 0.1 mm wide.

The most probable values (MPV) for these distributions are 1.25 mm for the Induction-1 plane, 0.85 mm for the Induction-2 plane, 0.95 mm for the Collection plane, and 1.05 mm for the σ_{3P} averaged over the three planes. According to Equation (4.9), for average values of $n_{\rm hit} \sim 30$, this corresponds to an angular resolution of the order of $\theta_{3P} \sim 3$ mrad.

Note that the plots in Figure 6.2 for each reconstruction plane do not refer to the total sample of 1859 tracks, but only to the subsample of tracks which has a sufficient number of hits in that specific plane for a MCS fit to be performed. This subsample is defined as the one with tracks which have at least 3 hits per 14 cm segment and 30 hits in total in the chosen reconstruction plane. Another subsample of tracks can be defined, with only tracks that fulfill such require-

ments in all planes. The numbers of tracks¹ in these subsamples are reported in Table 6.1.

total number of real tracks of the sample	1859
number of valid real tracks in Induction-1 view	1647
number of valid real tracks in Induction-2 view	1599
number of valid real tracks in Collection view	1654
number of valid real tracks in all views	1547

Table 6.1: Total number of real tracks of the sample, numbers of valid real tracks in each reconstruction plane, and number of valid real tracks simultaneously in all reconstruction planes.

6.2 "Gran Sasso" algorithm performance

The performance of the "Gran Sasso" algorithm on real muon tracks is shown in Figure 6.4. The scatter plot in Figure 6.4 (left) shows the comparison between p_{range} and p_{MCS} . The histogram in Figure 6.4 (right) shows the distribution of $p_{\text{range}}/p_{\text{MCS}}-1$. The efficiencies ε for each plane are reported in Table 6.2.

	Induction-1	Induction-2	Collection
number of valid real tracks in the plane	1647	1599	1654
number of valid real tracks with physical p_{MCS}	1505	1309	1427
efficiency ε	91%	82%	86%

Table 6.2: Number of valid real tracks in each of the three reconstruction planes, number of valid real tracks with physical p_{MCS} and efficiency ε .

The comparison between p_{MCS} and p_{range} shown in Figure 6.4 for our sample of real stopping muon tracks shows again a fair agreement, even with a large uncertainty.

¹Our data sample would have contained about 20% more muons. Due to a software issue with the Gran Sasso algorithm, we chose not to use these muons for the MicroBooNE analysis either, as this would have introduced a significant efficiency difference. The cause of the issue is now well understood, but reprocessing the data would have been too time-consuming, so we decided to exclude this 20% of muons from all analyses.

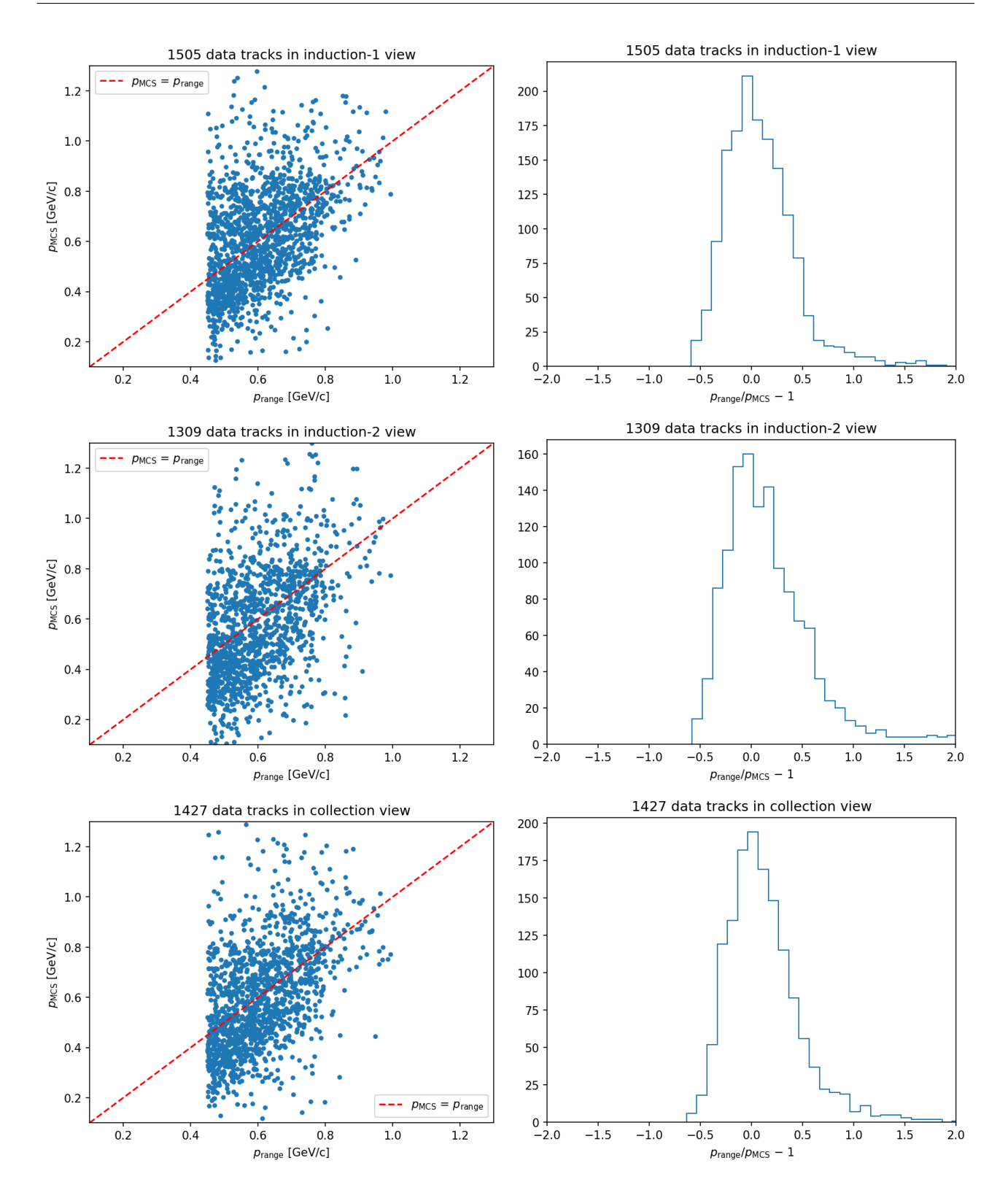


Figure 6.4: (Left) scatter plots of p_{MCS} versus p_{range} ; the red line represents $p_{\text{MCS}} = p_{\text{range}}$. (Right) distributions of $p_{\text{range}}/p_{\text{MCS}} - 1$, in bins of 0.1. Top plots, middle plots and bottom plots refer to the Induction-1, Induction-2 and Collection plane, respectively.

I made a profile of these data with respect to range momentum p_{range} , by grouping our sample into bins of width $100 \,\text{MeV}\,\text{c}^{-1}$, with the only exception of the last bin $0.8 - 1.0 \,\text{GeV}\,\text{c}^{-1}$ with a width of $200 \,\text{MeV}\,\text{c}^{-1}$, because of the scarce statistics available in the range $0.9 - 1.0 \,\text{GeV}\,\text{c}^{-1}$.

Fractional bias and resolution – definitions can be found in Section 5.2 – are shown in Figure 6.5 for the three reconstruction planes.

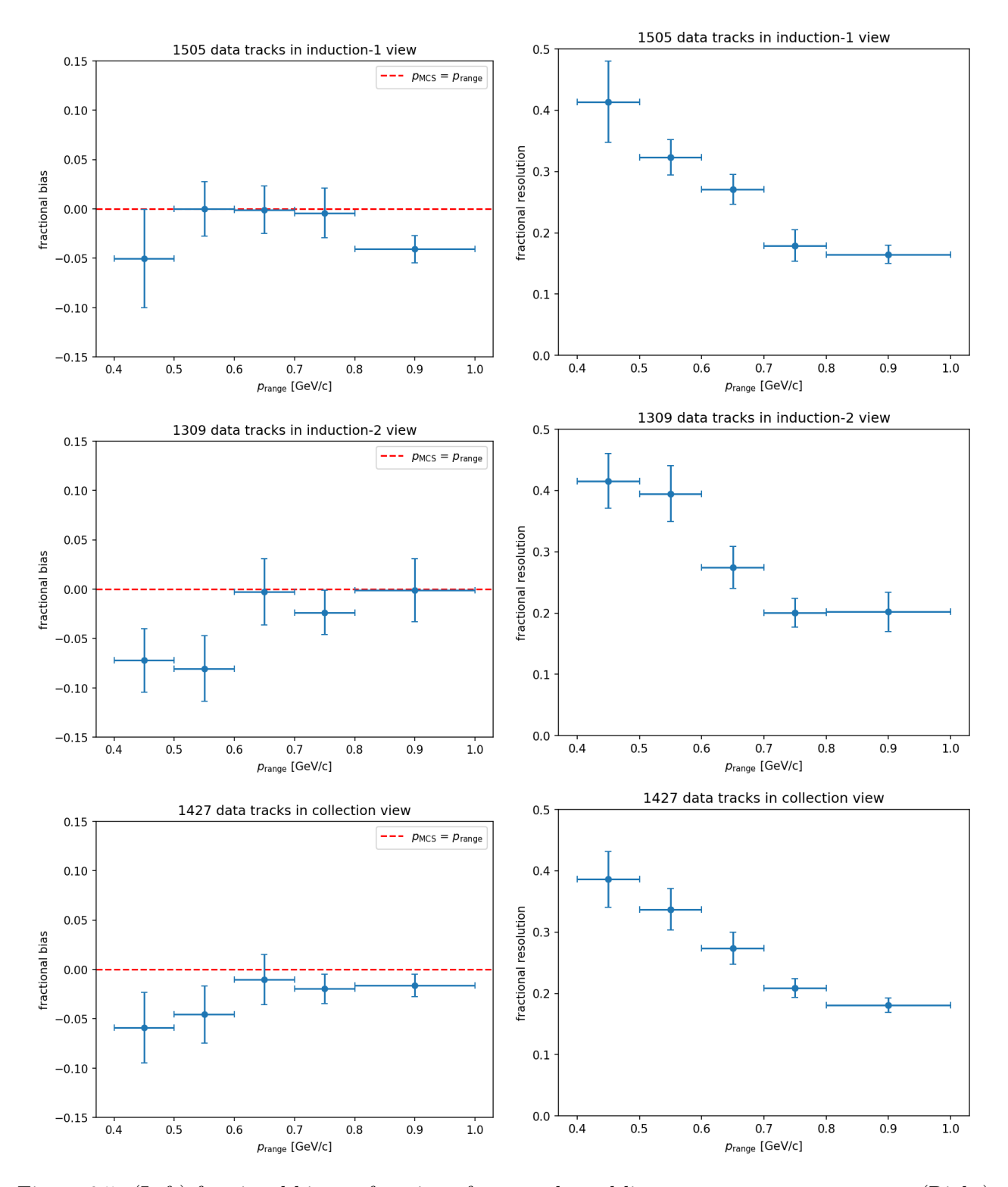


Figure 6.5: (Left) fractional bias as function of p_{range} ; the red line represents $p_{\text{MCS}} = p_{\text{range}}$. (Right) fractional resolution as function of p_{range} . Top plots, middle plots and bottom plots refer to the Induction-1, Induction-2 and Collection plane, respectively.

A small negative bias of about 5-7% is observed in all the planes at low momentum: it seems to be larger in the Induction-2 plane, and in any case larger than what is seen in MC.

The resolution is at the level of 41% in Induction-1, 42% in Induction-2, 39% in Collection plane at low momentum ($p_{\text{range}} \in 0.4 - 0.5 \,\text{GeV}\,\text{c}^{-1}$), and at the level of 17% in Induction-1, 20% in Induction-2, 18% in Collection plane at high momentum ($p_{\text{range}} \in 0.8 - 1.0 \,\text{GeV}\,\text{c}^{-1}$). Overall, the performance appears to be slightly worse in the data compared to MC. This could be the hint of some detector effects which have not yet been simulated in current MC models.

6.2.1 Combining the Collection plane with other planes

As stated in Subsection 5.2.1, combining different planes allows to maximize the information contained in the input. Figure 6.6 shows the correlation between the p_{MCS} reconstructed from the Collection plane and the p_{MCS} reconstructed from the Induction planes.

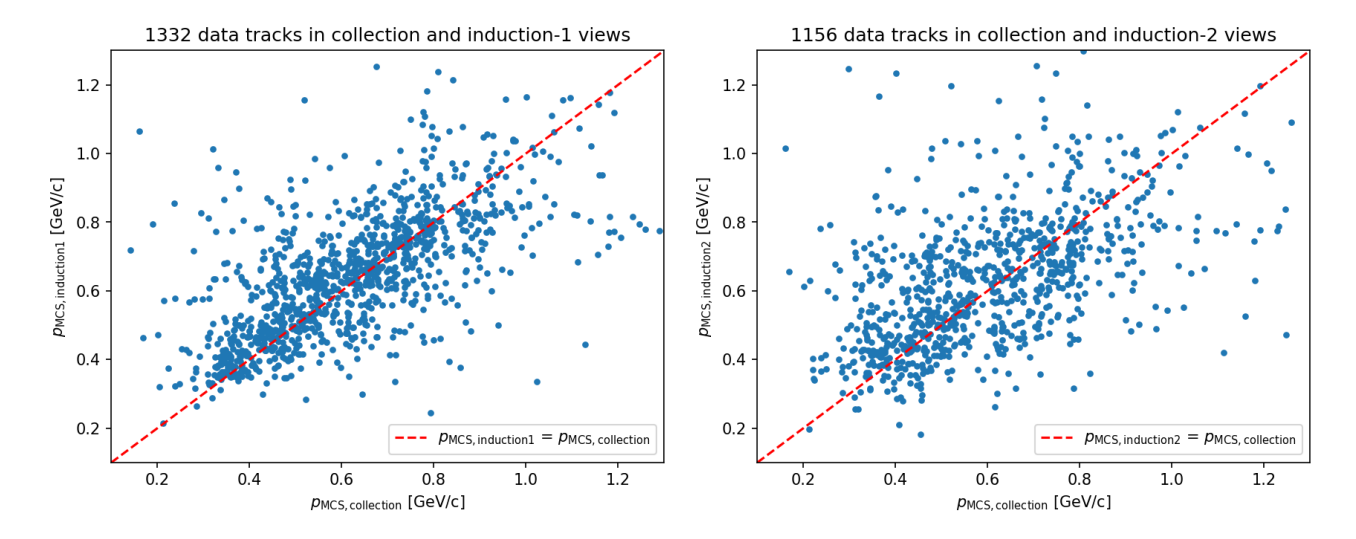


Figure 6.6: (Left) scatter plot of p_{MCS} as measured in the Collection plane versus p_{MCS} as measured in the Induction-2 plane. (Right) scatter plot of p_{MCS} as measured in the Collection plane versus p_{MCS} as measured in the Induction-1 plane.

The correlation coefficient is found to be 0.46 in the case of $Collection \oplus Induction-2$ planes and 0.69 in the case of $Collection \oplus Induction-1$ planes. The momentum p_{MCS} reconstructed in the Induction-1 and Induction-2 planes appear thus partially, but not completely, correlated to the momentum p_{MCS} reconstructed in the Collection plane. Starting from valid tracks in the Collection plane, similarly to what was done with MC – see Subsection 5.2.1 – it is possible to compute the average of p_{MCS} in Collection and Induction-2 planes ($Collection \oplus Induction-2$), the average of p_{MCS} in Collection and Induction-1 planes ($Collection \oplus Induction-1$), and the average of p_{MCS} in all the planes ($Collection \oplus Induction-2 \oplus Induction-1$).

Figure 6.7 shows the scatter plots of p_{range} versus p_{MCS} and the distributions of $p_{\text{range}}/p_{\text{MCS}} - 1$, for these three different cases.

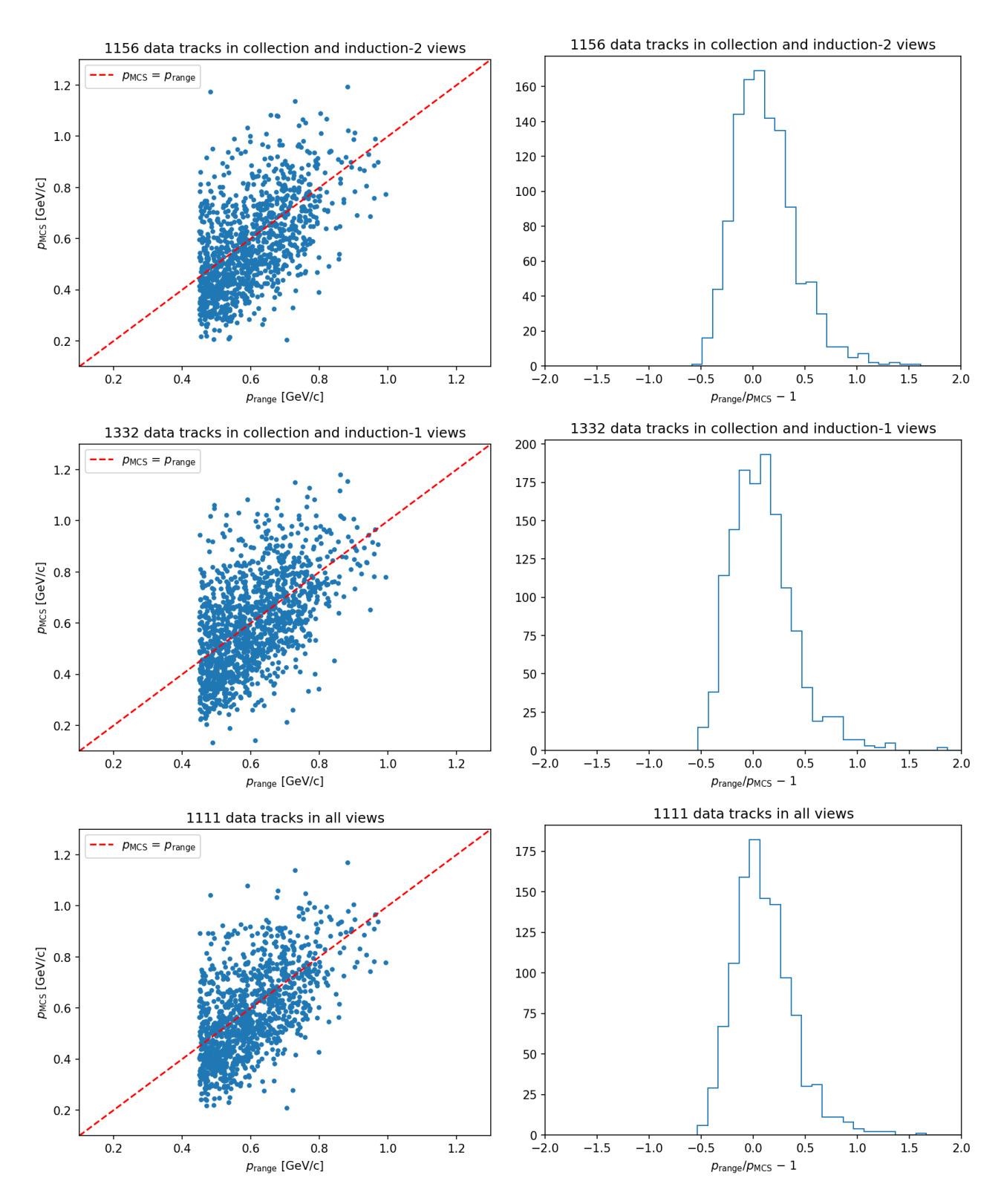


Figure 6.7: (Left) scatter plots of p_{MCS} versus p_{range} ; the red line represents $p_{\text{MCS}} = p_{\text{range}}$. (Right) distributions of $p_{\text{range}}/p_{\text{MCS}} - 1$, in bins of 0.1. Top plots, middle plots and bottom plots refer to the $Collection \oplus Induction-2$ planes, to the $Collection \oplus Induction-1$ planes, and to the $Collection \oplus Induction-2 \oplus Induction-1$ planes, respectively.

Figure 6.8 shows the fractional bias and resolution for the three cases, as extracted from the scatter plots following the same procedure described in Section 5.2.

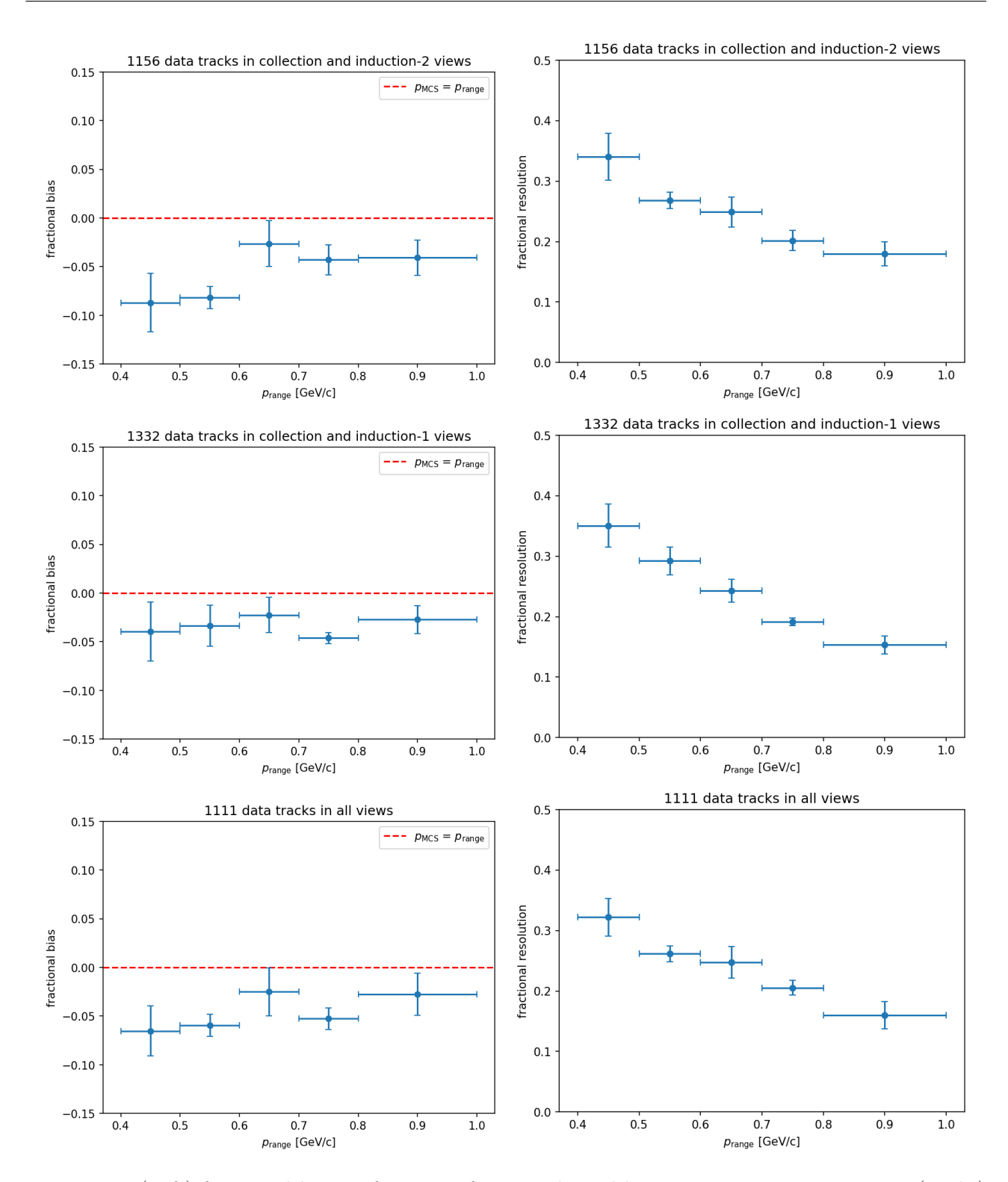


Figure 6.8: (Left) fractional bias as function of $p_{\rm range}$; the red line represents $p_{\rm MCS} = p_{\rm range}$. (Right) fractional resolution as a function of $p_{\rm range}$. Top plots, middle plots and bottom plots refer to the Collection \oplus Induction-2 planes, to the Collection \oplus Induction-1 planes, and to the Collection \oplus Induction-2 \oplus Induction-1 planes, respectively.

There is a slight improvement of the resolution. The combination of two or three views slightly decrease the fractional bias. The resolution, from about 40% at low momentum and about 18% at high momentum in a single view, is now at the level of 32% at low momentum and 16% at high momentum, with all the views combined.

6.2.2 Extension to 3D for the "Gran Sasso" algorithm

The performance of the 3D version of the "Gran Sasso" algorithm, with our sample of real muon tracks, is shown in Figure 6.11 with the scatter plot of $p_{\rm range}$ versus $p_{\rm MCS}$, the distribution of $p_{\rm range}/p_{\rm MCS}-1$ for all tracks and the distributions of $p_{\rm range}/p_{\rm MCS}-1$ for the five intervals of $p_{\rm range}$ considered.

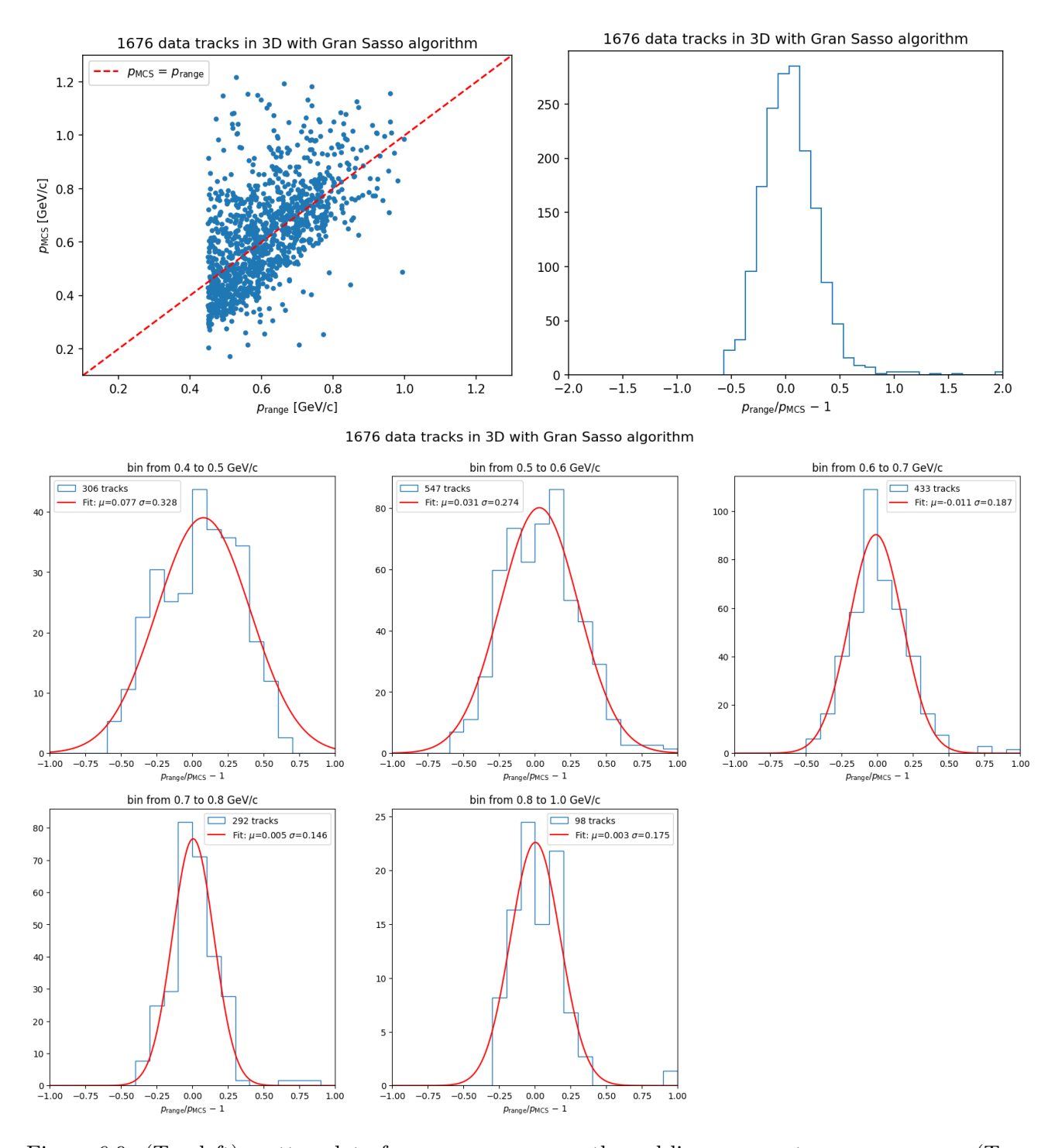


Figure 6.9: (Top left) scatter plot of p_{MCS} versus p_{range} ; the red line represents $p_{\text{MCS}} = p_{\text{range}}$. (Top right) distribution of $p_{\text{range}}/p_{\text{MCS}}-1$, in bins of 0.1. (Bottom) distributions of $p_{\text{range}}/p_{\text{MCS}}-1$ for the five p_{range} intervals, in bins of 0.1; the red curves represents the Gaussian fits.

The efficiency ε of the 3D "Gran Sasso" algorithm, just as defined for the 2D version of the algorithm, is summarized in Table 6.3.

number of valid MC tracks	1859
number of MC tracks with physical p_{MCS}	1676
efficiency ε	90%

Table 6.3: Number of valid real tracks, number of valid real tracks with physical p_{MCS} and efficiency ε for the 3D version of the "Gran Sasso" algorithm.

Figure 6.10 shows the p_{MCS} bias and resolution for the 3D version of the "Gran Sasso" algorithm, as extracted from the scatter plots used the same procedure described in the previous chapter.

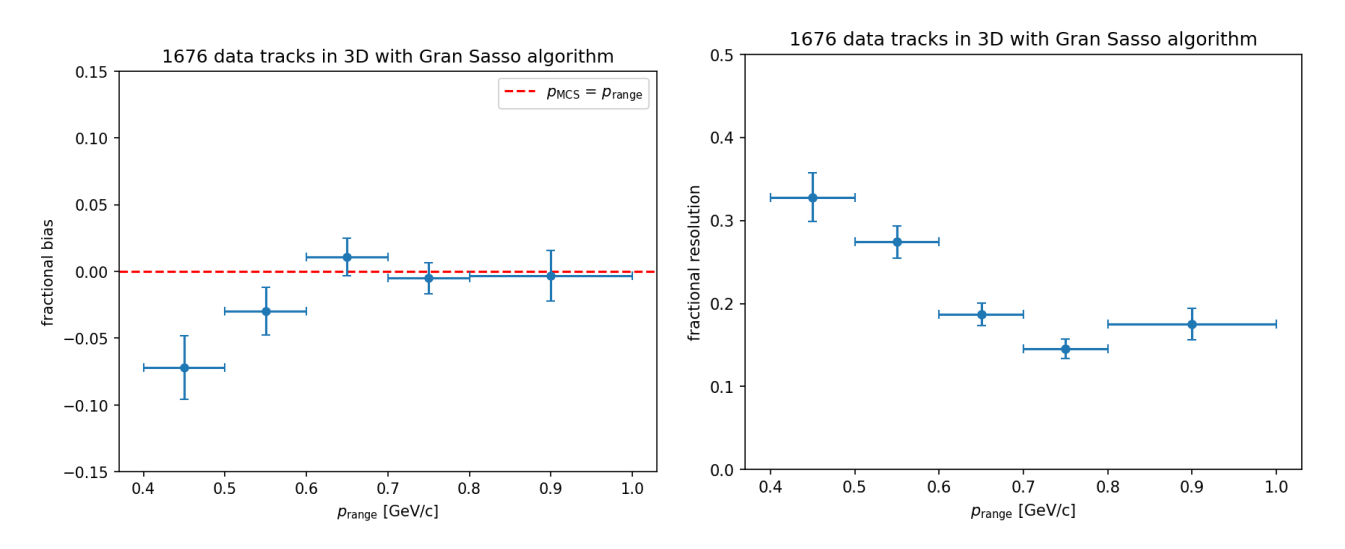


Figure 6.10: (Left) fractional bias as a function of p_{range} ; the red line represents $p_{\text{MCS}} = p_{\text{range}}$. (Right) fractional resolution as a function of p_{range} .

In the 3D version of the algorithm, p_{MCS} shows a small negative bias at low momentum. The resolution is at the level of 33% at low momentum and 18% at high momentum, slightly better than combining all the views.

6.3 "MicroBooNE" algorithm performance

The performance of the "MicroBooNE" algorithm, originally developed by the MicroBooNE Collaboration and tested here with ICARUS events, is shown in Figure 6.11 with the scatter plot of $p_{\rm range}$ versus $p_{\rm MCS}$, the distribution of $p_{\rm range}/p_{\rm MCS}-1$ for all tracks and the distributions of $p_{\rm range}/p_{\rm MCS}-1$ for the five intervals of $p_{\rm range}$ considered.

The efficiency ε of the "MicroBooNE" algorithm, using the same definition as for the 3D version of the "Gran Sasso" algorithm, is summarized in Table 6.4.

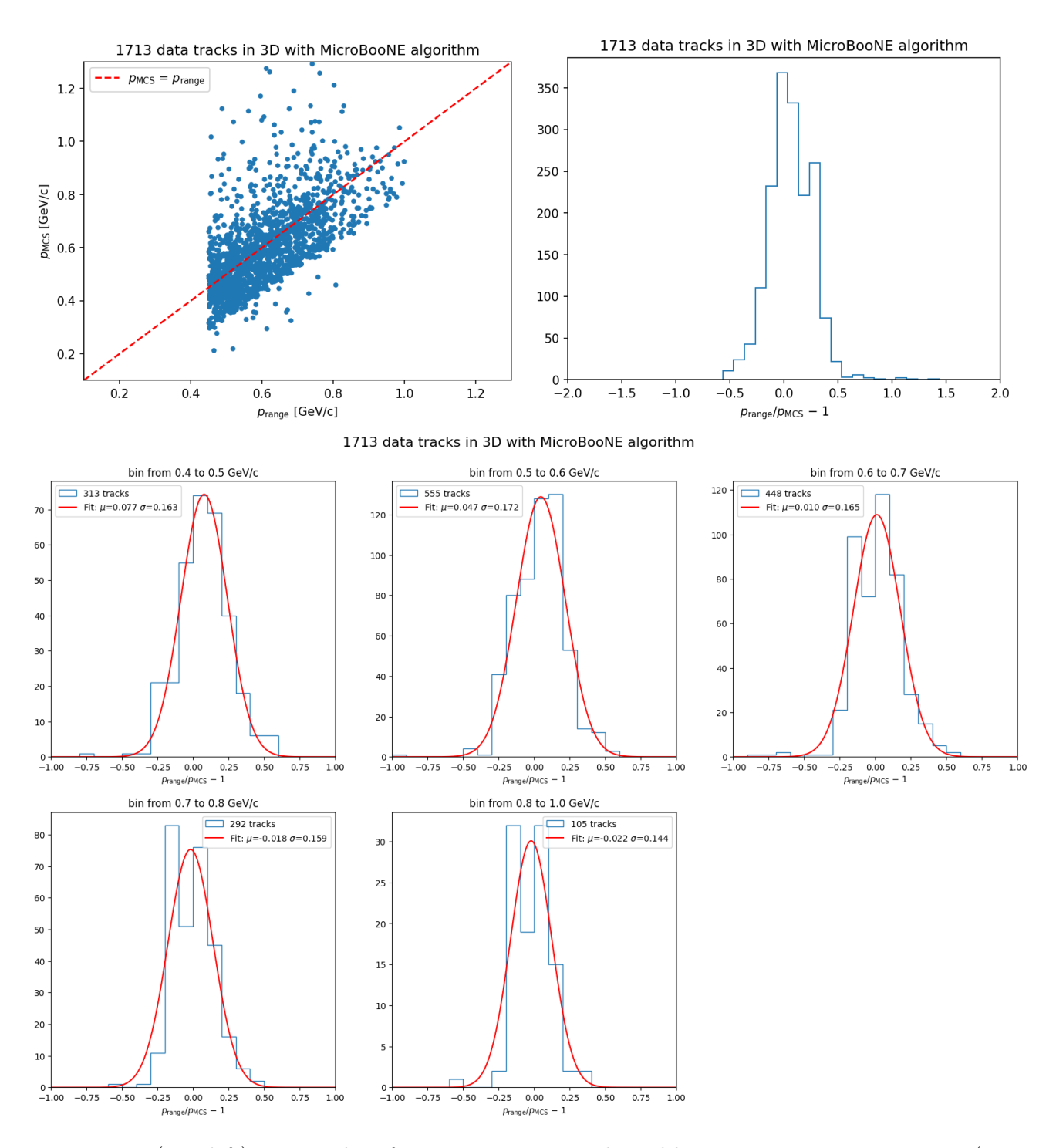


Figure 6.11: (Top left) scatter plot of p_{MCS} versus p_{range} ; the red line represents $p_{\text{MCS}} = p_{\text{range}}$. (Top right) distribution of $p_{\text{range}}/p_{\text{MCS}} - 1$, in bins of 0.1. (Bottom) distributions of $p_{\text{range}}/p_{\text{MCS}} - 1$ for the five p_{range} intervals, in bins of 0.1; the red curves represents the Gaussian fits.

number of valid real tracks	1859
number of valid real tracks with physical p_{MCS}	1713
efficiency ε	92%

Table 6.4: Number of valid real tracks, number of valid real tracks with physical p_{MCS} and efficiency ε for the "MicroBooNE" algorithm.

Figure 6.12 shows the p_{MCS} bias and resolution for the "MicroBooNE" algorithm, as extracted from the scatter plots used the same procedure described in the previous chapter.

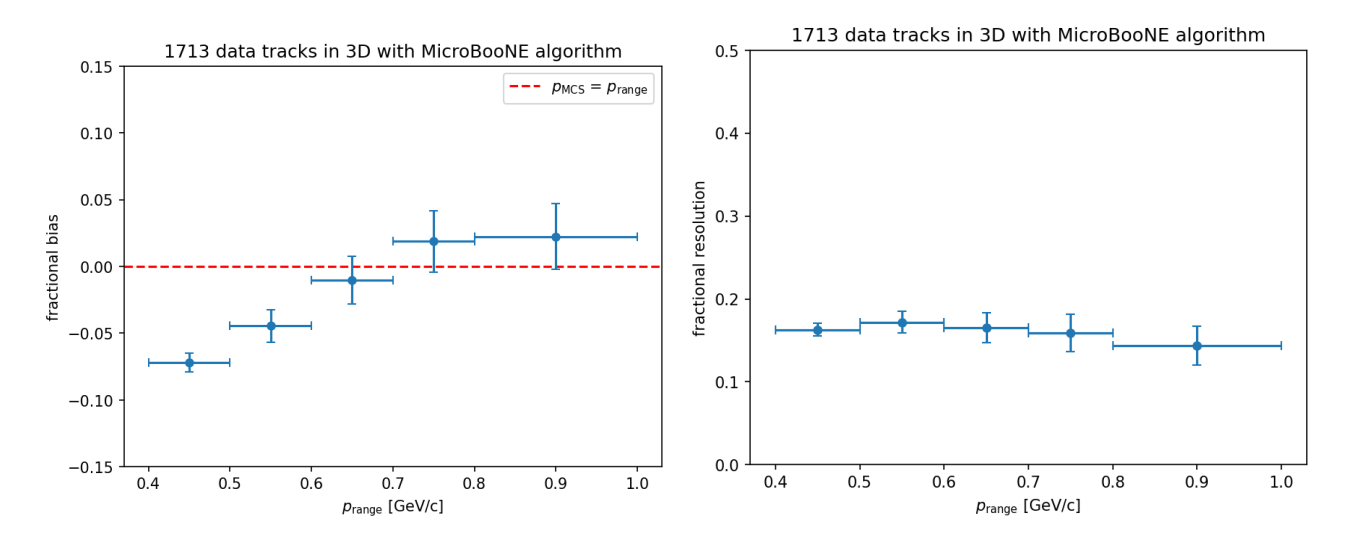


Figure 6.12: (Left) fractional bias as a function of p_{range} ; the red line represents $p_{\text{MCS}} = p_{\text{range}}$. (Right) fractional resolution as a function of p_{range} .

There is a small positive bias at high momentum and a small negative bias at low momentum. Resolution ranges from about 16% at low momentum to about 14% at high momentum.

6.4 Results of analysis on real muon tracks

The analysis of real stopping muon tracks in ICARUS has provided a direct validation of the "Gran Sasso" and "MicroBooNE" MCS-based momentum estimation algorithms under actual detector conditions. Compared to Monte Carlo simulations, real data exhibit a slightly worse resolution and a small negative bias, particularly at low momentum. This discrepancy might indicate the presence of detector effects — such as non-uniformities of the cathode planarity — for which there is not a detailed simulation yet.

As in the MC analysis, the "Gran Sasso" algorithm shows an overall good agreement between $p_{\rm MCS}$ and $p_{\rm range}$, with an improvement in resolution when multiple views are combined. The resolution, initially between 40% at low momentum and 18% at high momentum in a single view, improves to 32% at low momentum and 16% at high momentum when all views are used together. The 3D version of the algorithm provides comparable performance, confirming its validity as an alternative approach. The "MicroBooNE" algorithm, tested on real data, maintains a small bias and a stable resolution, ranging from 16% at low momentum to 14% at high momentum, in line with expectations from MC. These results demonstrate that MCS-based momentum estimation remains a viable approach in ICARUS, though real data suggest that additional systematic uncertainties must be accounted for.

Conclusions

The Short Baseline Neutrino program at Fermilab represents a major experimental initiative aimed at investigating the possible presence of sterile neutrinos through the study of short-baseline neutrino oscillations. The ICARUS-T600 detector plays a key role within this program, serving as the far detector in the SBN program which also includes MicroBooNE and the near detector SBND. ICARUS employs the Liquid Argon Time Projection Chamber (LArTPC) technology, which enables exceptional spatial resolution in track reconstruction and an accurate calorimetric reconstruction. This is achieved by matching information through the read-out of the drift electron signal by three anode wire planes with different orientations. This capability is crucial for characterizing neutrino interactions in the energy range $0-3\,\mathrm{GeV}$ and for testing anomalies observed in previous experiments such as LSND and MiniBooNE, but also for some precision measurements of neutrino-Argon cross sections.

ICARUS is designed to analyze neutrino events produced by both the BNB (Booster Neutrino Beam) and the NuMI (Neutrinos at the Main Injector) beamlines, enabling a broad spectrum of studies on fundamental neutrino properties. Its strategic position within the SBN program allows for oscillation measurements with high sensitivity, verifying the potential existence of a sterile component in the neutrino oscillation framework. Simultaneously, the experiment provides fundamental data for improving theoretical models of neutrino-nucleon interactions in liquid Argon, contributing to the advancement of LArTPC technology in preparation for future experiments such as DUNE (Deep Underground Neutrino Experiment).

One of the fundamental aspects of neutrino physics is the determination of the momentum p of the charged particles produced in the neutrino interactions. In the case of muons, which serve as a crucial signature in charged current (CC) neutrino events, momentum measurement is essential for kinematic reconstruction and event selection. ICARUS does not have a magnetic field for track curvature, thus necessitating alternative strategies for momentum determination. The technique that reconstructs momentum via Multiple Coulomb Scattering (MCS) exploits the statistical relationship between the multiple scattering experienced by a charged particle traveling through a medium and its momentum, parametrized by the Highland formula.

Specifically, any MCS algorithm estimates the momentum of a muon by measuring the angular deviation of the track due to scattering off Argon nuclei. This approach provides a valuable alternative to the range-based method, which directly measures track length to infer the muon

kinetic energy. The main advantage of MCS is that it can be applied to muons that do not stop within the detector, for which the range-based method is not applicable. This makes the MCS algorithm an essential tool for ICARUS analyses, enabling the extraction of crucial information on muon kinematics in neutrino interaction events, whereas no other method successfully works.

The state-of-the-art is represented by two algorithms, conventionally named "Gran Sasso" and "MicroBooNE" algorithms, which were tested on a sample of cosmic stopping muons in ICARUS. This thesis presented a detailed analysis of momentum reconstruction performance through MCS, conducted on both MC and real data. It first focused on validating the algorithm on simulated muons, comparing the reconstructed momentum p_{MCS} with the range-based estimated momentum p_{range} . The "Gran Sasso" algorithm was tested on different reconstruction views (Induction-1, Induction-2, and Collection) demonstrating that combining information from multiple planes improves the accuracy of the momentum estimate.

The main results obtained from Monte Carlo tracks are as follows:

- the resolution of p_{MCS} improves with increasing momentum, ranging from about 32% at low momentum ($p \in 0.4 0.5 \,\text{GeV}\,\text{c}^{-1}$) to 16% at high momentum ($p \in 0.8 1.0 \,\text{GeV}\,\text{c}^{-1}$);
- the bias remains close to zero for the Induction-1 and Collection views; a slight negative bias of about 6% is observed in the Induction-2 view for momenta $p < 0.6 \,\mathrm{GeV}\,\mathrm{c}^{-1}$
- extending the "Gran Sasso" algorithm to the 3D reconstruction resulted in a resolution comparable to that of combining the three 2D views;
- the "MicroBooNE" algorithm, tested under the same conditions, exhibits an almost constant positive bias of 2-4% across the entire momentum range and better resolution at low energies, compared to the "Gran Sasso" algorithm.

The analysis was then extended to real tracks, allowing for the verification of the algorithms effectiveness under experimental conditions. The results indicate an overall performance slightly worse than in MC simulations, suggesting the presence of detector effects not fully modeled in the MC. The key experimental results include:

- the momentum resolution of the "Gran Sasso" algorithm in individual views is worse compared to MC, ranging from about 40% at low momentum to 18% at high momentum;
- using all reconstruction views combined, the resolution improves to 32% at low momentum and 16% at high momentum;
- the "MicroBooNE" algorithm exhibits a slightly better resolution, with 16% at low momentum and 14% at high momentum, confirming the trend observed in MC.

These results demonstrate that the MCS algorithm is an effective tool to measure the muon momentum in ICARUS, but also highlight the challenges associated with applying this technique to real data. The comparison between MC and data has helped identify the main discrepancies and suggested possible improvement strategies, including refining systematic corrections and improving detector calibration.

Future efforts should focus on optimizing reconstruction algorithms and reducing systematic uncertainties to fully exploit the potential of ICARUS in neutrino oscillation and interaction studies. Specifically, the performance of the algorithms can be studied as a function of track length instead of momentum from range. One could attempt to optimize the segment length, currently set to 14 cm—equal to the radiation length of Argon—as well as the minimum number of segments, or alternatively the minimum track length, required to obtain a reasonable result. In fact, using segments shorter than 14 cm increases the number of angles, thereby improving the resolution. It is also interesting to study the performance of the algorithms by using a fixed track length (the first L meters) to evaluate the resolution trend as a function of p^2 , as described in Chapter 4. Finally, the core of the algorithm could be improved by incorporating effects such as the removal of delta rays, or by testing it on new MC simulations where the electric field distortion near the cathode is properly modeled.

Overall, the results obtained from this analysis are significant from a physics perspective, as they will enable at least a twofold increase in the statistics of BNB ν_{μ} CC interactions and a threefold increase in the statistics of NuMI ν_{μ} CC interactions. This is crucial for improving the study of neutrino oscillations in the ν_{μ} disappearance channel and searching for 3+1 oscillations.

Appendix A: Covariance matrices

The χ^2 -like function (called C_2 function) designed by the "Gran Sasso" algorithm to compare the observed deflections on a track with the expected deflections for a given momentum p is

$$C_2(p) = V^T C^{-1}(p)V (6.1)$$

where V is a $2n_{\rm seg}-3$ vector that contains all the observed scattering angles, both the $n_{\rm seg}-2$ computed with the polygonal approach and the $n_{\rm seg}-1$ computed with the linear-fit approach

$$V = \begin{pmatrix} V_{\text{poly}} \\ V_{\text{lin}} \end{pmatrix} \tag{6.2}$$

and C(p) is a matrix that expresses the expected scattering angles and their mutual correlations

$$C(p) = \begin{pmatrix} C_{\text{poly}}(p) & C_{\text{mix}}(p) \\ {}^{T}C_{\text{mix}}(p) & C_{\text{lin}}(p) \end{pmatrix}$$

$$(6.3)$$

Sub-matrices $C_{\text{poly}}(p)$, $C_{\text{lin}}(p)$ refer to the polygonal and linear-fit scattering angles respectively, while $C_{\text{mix}}(p)$ accounts for their cross-correlation introduced by the MCS. Both $C_{\text{poly}}(p)$ and $C_{\text{lin}}(p)$ are sum of a MCS component and a component due to measurement error contribution:

$$C_{\text{poly}}(p) = C_{\text{poly}}^{\text{MCS}}(p) + C_{\text{poly}}^{\text{meas}}$$
(6.4)

$$C_{\rm lin}(p) = C_{\rm lin}^{\rm MCS}(p) + C_{\rm lin}^{\rm meas} \tag{6.5}$$

The covariance sub-matrix $C_{\text{poly}}^{\text{MCS}}(p)$ describes the MCS contribution to the angles computed according to the polygonal approach, and has the 5-diagonal symmetrical form

$$C_{\text{poly}}^{\text{MCS}}(p) = \begin{pmatrix} \theta_{1}^{2} & \alpha_{\text{poly}}^{+}\theta_{1}\theta_{2} & \alpha_{\text{poly}}^{++}\theta_{1}\theta_{3} & 0 & \dots \\ \alpha_{\text{poly}}^{+}\theta_{2}\theta_{1} & \theta_{2}^{2} & \alpha_{\text{poly}}^{+}\theta_{2}\theta_{3} & \alpha_{\text{poly}}^{++}\theta_{2}\theta_{4} & \dots \\ \alpha_{\text{poly}}^{++}\theta_{3}\theta_{1} & \alpha_{\text{poly}}^{+}\theta_{3}\theta_{2} & \theta_{3}^{2} & \alpha_{\text{poly}}^{+}\theta_{3}\theta_{4} & \dots \\ 0 & \alpha_{\text{poly}}^{++}\theta_{4}\theta_{2} & \alpha_{\text{poly}}^{+}\theta_{4}\theta_{3} & \theta_{4}^{2} & \dots \\ \vdots & \vdots & \vdots & \vdots & \ddots \end{pmatrix}$$
(6.6)

due to the fact that three segments are involved in the polygonal scattering angle definition. Here $\theta_i = \theta_{\text{MCS}}(p_i)$ as stated in (4.8) is the polygonal scattering angle at the *i*-th segment, and constants α_{poly}^+ , $\alpha_{\text{poly}}^{++}$ were numerically computed with a model simulating individual Coulomb scatterings on a large number of tracks.

The covariance sub-matrix $C_{\text{poly}}^{\text{meas}}$ represents the contribution of the measurement error which is defined within a single segment, excluding any correlation between the different segments: therefore, since the factor θ_{3P}^2 express the independent angular uncertainty due to the single point resolution, it gets multiplied by a matrix that expresses the correlation between deflection at consecutive segments — and is not momentum-dependent:

$$C_{\text{poly}}^{\text{meas}} = \theta_{3P}^{2} \begin{pmatrix} 1 & -2/3 & 1/6 & 0 & \dots \\ -2/3 & 1 & -2/3 & 1/6 & \dots \\ 1/6 & -2/3 & 1 & -2/3 & \dots \\ 0 & 1/6 & -2/3 & 1 & \dots \\ \vdots & \vdots & \vdots & \vdots & \ddots \end{pmatrix}$$

$$(6.7)$$

The covariance sub-matrix $C_{\text{lin}}^{\text{MCS}}(p)$ describes the MCS contribution to the angles computed according to the linear-fit approach, and has the 3-diagonal symmetrical form

$$C_{\text{lin}}^{\text{MCS}}(p) = \begin{pmatrix} \theta_{0,1}^2 & \alpha_{\text{lin}}^+ \theta_{0,1} \theta_{1,2} & 0 & \dots \\ \alpha_{\text{lin}}^+ \theta_{1,2} \theta_{0,1} & \theta_{1,2}^2 & \alpha_{\text{lin}}^+ \theta_{1,2} \theta_{2,3} & \dots \\ 0 & \alpha_{\text{lin}}^+ \theta_{2,3} \theta_{1,2} & \theta_{2,3}^2 & \dots \\ \vdots & \vdots & \vdots & \ddots \end{pmatrix}$$
(6.8)

since only two segments are required in the linear-fit scattering angle definition. Here $\theta_{i,i+1} = \theta_{\text{MCS}}(p_{i,i+1})$ is the linear-fit scattering angle between the *i*-th segment and the *i*+1-th segment, and constant α_{lin}^+ was numerically computed in a similar way of α_{poly}^+ and $\alpha_{\text{poly}}^{++}$. The covariance sub-matrix $C_{\text{lin}}^{\text{meas}}$ represents the contribution of the measurement error and is given by

$$C_{\text{lin}}^{\text{meas}} = \theta_{3P}^{2} \begin{pmatrix} 1 & -1/2 & 0 & \dots \\ -1/2 & 1 & -1/2 & \dots \\ 0 & -1/2 & 1 & \dots \\ \vdots & \vdots & \vdots & \vdots & \ddots \end{pmatrix}$$

$$(6.9)$$

 $C_{\text{mix}}(p)$ has only MCS component, since measurement errors are defined within a single segment, excluding any correlation between different segments. The only covariance terms derive from the definition of the deflection angles as difference between neighboring segments: the same segment appears in 3 (2) deflection angles in the polygonal (linear-fit) case. Single-point measurement

errors for the polygonal and the linear-fit procedures are fully uncorrelated between each other:

$$C_{\text{mix}}(p) = C_{\text{mix}}^{\text{MCS}}(p) = \begin{pmatrix} \beta^{+}\theta_{1}\theta_{0,1} & \beta^{+}\theta_{1}\theta_{1,2} & \beta^{++}\theta_{1}\theta_{2,3} & 0 & \dots & \dots \\ \beta^{++}\theta_{2}\theta_{0,1} & \beta^{+}\theta_{2}\theta_{1,2} & \beta^{+}\theta_{2}\theta_{2,3} & \beta^{++}\theta_{2}\theta_{3,4} & 0 & \dots \\ 0 & \beta^{++}\theta_{3}\theta_{1,2} & \beta^{+}\theta_{3}\theta_{2,3} & \beta^{+}\theta_{3}\theta_{3,4} & \beta^{++}\theta_{3}\theta_{4,5} & \dots \\ \vdots & \vdots & \vdots & \vdots & \vdots & \ddots \end{pmatrix}$$
(6.10)

Basically, each polygonal term is correlated to 4 different linear-fit terms and viceversa, because the polygonal term involves 3 segments (i-1, i, i+1) while the linear term involves only 2 segments (i, i+1). The numerically computed constants β^+ , β^{++} parameterize the cases when the polygonal and linear-fit terms share two and one common segments respectively.

The numerical coefficients in the sub-matrices $C_{\text{poly}}^{\text{meas}}$ and $C_{\text{lin}}^{\text{meas}}$ are obtained by considering the correlation between adjacent segments. Recall that, for example, in the linear-fit approach, the same segment is used to compute two different angles. Since the C_2 function considers the deflections $\theta_{i,i+1}$ as the differences between the ψ_i directions of adjacent segments, the ψ_i direction of a single segment appears in two different $\theta_{i,i+1}$ values: $\theta_{i-1,i} = \psi_i - \psi_{i-1}$ and $\theta_{i,i+1} = \psi_{i+1} - \psi_i$. The off-diagonal term gives the correlation between $\theta_{i-1,i}$ and $\theta_{i,i+1}$, which is negative because they are correlated through ψ_i that has opposite effects: if ψ_i is underestimated, then $\theta_{i-1,i}$ will be underestimated too but $\theta_{i,i+1}$ will be overestimated. The value -1/2 comes from the fact that the correlated part is one of two terms that have, on average, the same variance, so the anti-correlation affects, on average, half the value of $\theta_{i-1,i}$. The coefficients in the correlation sub-matrix $C_{\text{poly}}^{\text{meas}}$ are obtained in the same way.

Note that this analysis involves Gaussian contribution to the various errors, while the physical MCS deflection angle distribution also exhibits significant non-Gaussian tails which can affect the MCS momentum measurement. Therefore, single scattering terms contributing more than 3σ to the C_2 function are excluded from the computation.

Bibliography

- [1] W. Pauli, Dear radioactive ladies and gentlemen, Physics Today, 31 (1978), p. 27.
- [2] L. M. Brown, The idea of the neutrino, Physics Today, 31 (1978), pp. 23–28, doi:10. 1063/1.2995181.
- [3] C. D. Ellis and W. A. Wooster, *The average energy of disintegration of radium E*, Proceedings of the Royal Society A, 117 (1927), pp. 109–123, doi:10.1098/rspa.1927.0168.
- [4] L. MEITNER AND W. ORTHMANN, Über eine absolute bestimmung der energie der primären β -Strahlen von radium E, Zeitschrift für Physik, 60 (1930), pp. 143–155, doi:10.1007/Bf01339819.
- [5] E. Fermi, Tentativo di una teoria dell'emissione dei raggi beta, Ricerca Scientifica, 4 (1933), pp. 491–495.
- [6] E. AMALDI, From the discovery of the neutron to the discovery of nuclear fission, Physics Reports, 111 (1984), pp. 1–332, doi:10.1016/0370-1573(84)90214-X.
- [7] F. L. WILSON, Fermi's Theory of Beta Decay, American Journal of Physics, 36 (1968), pp. 1150–1160, doi:10.1119/1.1974382.
- [8] F. CLOSE, Neutrino, 2010.
- [9] C. L. COWAN AND F. REINES, *Detection of the free neutrino*, Physics Review Journal, 92 (1953), pp. 830–831, doi:10.1103/PhysRev.92.830.
- [10] C. L. COWAN, F. REINES, ET AL., Detection of the free neutrino: A Confirmation, Science, 124 (1956), pp. 103–104, doi:10.1126/science.124.3212.103.
- [11] G. Danby et al., Observation of High-Energy Neutrino Reactions and the Existence of Two Kinds of Neutrinos, Physical Review Letters, 9 (1962), pp. 36–44, doi:10.1103/PhysRevLett.9.36.
- [12] M. L. PERL ET AL., Evidence for Anomalous Lepton Production in e⁺e⁻ Annihilation, Physical Review Letters, 35 (1975), pp. 1489–1492, doi:10.1103/PhysRevLett.35.1489.

[13] K. KODAMA ET AL., Observation of tau neutrino interactions, Physics Letters B, 504 (2001), pp. 218–224, doi:10.1016/S0370-2693(01)00307-0, arXiv:hep-ex/0012035.

- [14] D. DECAMP ET AL., A Precise Determination of the Number of Families With Light Neutrinos and of the Z Boson Partial Widths, Physics Letters B, 235 (1990), pp. 399–411, doi:10.1016/0370-2693(90)91984-J.
- [15] G. Alexander et al., Electroweak parameters of the Z⁰ resonance and the Standard Model: the LEP Collaborations, Physics Letters B, 276 (1992), pp. 247–253, doi:10.1016/0370-2693(92)90572-L.
- [16] B. Holstein, The theory of almost everything: The standard model, the unsung triumph of modern physics, Physics Today, 59 (2006), pp. 49–50.
- [17] M. GOLDHABER ET AL., *Helicity of Neutrinos*, Physical Review Journals, 109 (1958), pp. 1015–1017, doi:10.1103/PhysRev.109.1015.
- [18] D. Griffiths, Introduction to elementary particles, 2008.
- [19] R. S. Jones, Muon-neutrino disappearance with multiple liquid argon time projection chambers in the Fermilab Booster neutrino beam., PhD Thesis, Liverpool University, 2021, doi:10.17638/03143192.
- [20] M. Sajjad Athar et al., Neutrinos and their interactions with matter, Progress in Particle and Nuclear Physics, 129, 104019 (2023), doi:10.1016/j.ppnp.2022.104019, arXiv:2206.13792.
- [21] M. SAJJAD ATHAR ET AL., Neutrinos and their interactions, The European Physical Journal Special Topics, 230 (2021), pp. 4215–4220, doi:10.1140/epjs/s11734-021-00302-x, arXiv:2111.12328.
- [22] V. D. BARGER ET AL., The Physics of Neutrinos, Princeton University Press, 2012.
- [23] B. Pontecorvo, Inverse beta processes and nonconservation of lepton charge, Zhurnal Eksperimental'noi i Teoreticheskoi Fiziki, 34 (1957), p. 247.
- [24] B. Pontecorvo, Neutrino Experiments and the Problem of Conservation of Leptonic Charge, Zhurnal Eksperimental'noi i Teoreticheskoi Fiziki, 53 (1967), pp. 1717–1725.
- [25] V. N. GRIBOV AND B. PONTECORVO, Neutrino astronomy and lepton charge, Physics Letters B, 28 (1969), p. 493, doi:10.1016/0370-2693(69)90525-5.
- [26] R. Davis, Jr. et al., Search for neutrinos from the sun, Physical Review Letters, 20 (1968), pp. 1205–1209, doi:10.1103/PhysRevLett.20.1205.
- [27] P. Anselmann et al., Solar neutrinos observed by GALLEX at Gran Sasso., Physics Letters B, 285 (1992), pp. 376–389, doi:10.1016/0370-2693(92)91521-A.

[28] J. N. ABDURASHITOV ET AL., Measurement of the solar neutrino capture rate with gallium metal, Physical Review C, 60, 055801 (1999), doi:10.1103/PhysRevC.60.055801, arXiv:astro-ph/9907113.

- [29] K. S. HIRATA ET AL., Observation of a small atmospheric ν_{μ}/ν_{e} ratio in Kamiokande, Physics Letters B, 280 (1992), pp. 146–152, doi:10.1016/0370-2693(92)90788-6.
- [30] Q. R. Ahmad et al., Measurement of the rate of $\nu_e + d \rightarrow p + p + e^-$ interactions produced by ⁸B solar neutrinos at the Sudbury Neutrino Observatory, Physical Review Letters, 87, 071301 (2001), doi:10.1103/PhysRevLett.87.071301, arXiv:nucl-ex/0106015.
- [31] T. J. HAINES ET AL., Calculation of Atmospheric Neutrino Induced Backgrounds in a Nucleon Decay Search, Physical Review Letters, 57 (1986), pp. 1986–1989, doi:10.1103/PhysRevLett.57.1986.
- [32] M. NAKAHATA ET AL., Atmospheric Neutrino Background and Pion Nuclear Effect for Kamioka Nucleon Decay Experiment, Journal of the Physical Society of Japan, 55 (1986), p. 3786, doi:10.1143/JPSJ.55.3786.
- [33] Y. Fukuda et al., Evidence for oscillation of atmospheric neutrinos, Physical Review Letters, 81 (1998), pp. 1562–1567, doi:10.1103/PhysRevLett.81.1562, arXiv:hep-ex/9807003.
- [34] G. Bellini et al., *Neutrino oscillations*, Advances in High Energy Physics, 2014, 191960 (2014), doi:10.1155/2014/191960, arXiv:1310.7858.
- [35] Z. Maki, M. Nakagawa, and S. Sakata, Remarks on the unified model of elementary particles, Progress of Theoretical Physics, 28 (1962), pp. 870–880, doi:10.1143/PTP.28.870.
- [36] C. Giunti and C. W. Kim, Fundamentals of Neutrino Physics and Astrophysics, 2007.
- [37] R. L. WORKMAN ET AL., *Review of Particle Physics*, Progress of Theoretical and Experimental Physics, 2022 (2022), doi:10.1093/ptep/ptac097.
- [38] V. D. BARGER ET AL., Matter Effects on Three-Neutrino Oscillations, Physical Review D, 22 (1980), pp. 2718–2726, doi:10.1103/PhysRevD.22.2718.
- [39] S. P. MIKHEYEV AND A. Y. SMIRNOV, Resonance Amplification of Oscillations in Matter and Spectroscopy of Solar Neutrinos, Soviet Journal of Nuclear Physics, 42 (1985), pp. 913–917.
- [40] K. EGUCHI ET AL., First results from KamLAND: Evidence for reactor anti-neutrino disappearance, Physical Review Letters, 90, 021802 (2003), doi:10.1103/PhysRevLett. 90.021802, arXiv:hep-ex/0212021.

[41] R. TRIOZZI, Study of the trigger system performance of the ICARUS-T600 detector at Fermilab exposed to the Booster and NuMI neutrino beams, Master's Thesis, Università degli Studi di Padova, 2023, https://hdl.handle.net/20.500.12608/52881.

- [42] M. THOMSON, Modern particle physics, Cambridge University Press, New York, 2013, doi:10.1017/CB09781139525367.
- [43] K. ABE ET AL., Solar Neutrino Measurements in Super-Kamiokande-IV, Physical Review D, 94, 052010 (2016), doi:10.1103/PhysRevD.94.052010, arXiv:1606.07538.
- [44] G. Bellini et al., Precision measurement of the 7Be solar neutrino interaction rate in Borexino, Physical Review Letters, 107, 141302 (2011), doi:10.1103/PhysRevLett.107. 141302, arXiv:1104.1816.
- [45] A. GANDO ET AL., Reactor On-Off Antineutrino Measurement with KamLAND, Physical Review D, 88, 033001 (2013), doi:10.1103/PhysRevD.88.033001, arXiv:1303.4667.
- [46] M. G. Aartsen et al., Measurement of Atmospheric Neutrino Oscillations at 6–56 GeV with IceCube DeepCore, Physical Review Letters, 120, 071801 (2018), doi:10.1103/PhysRevLett.120.071801, arXiv:1707.07081.
- [47] M. APOLLONIO ET AL., Search for neutrino oscillations on a long baseline at the CHOOZ nuclear power station, The European Physical Journal C, 27 (2003), pp. 331–374, doi:10. 1140/epjc/s2002-01127-9, arXiv:hep-ex/0301017.
- [48] Y. ABE ET AL., Indication of Reactor $\bar{\nu}_e$ Disappearance in the Double Chooz Experiment, Physical Review Letters, 108, 131801 (2012), doi:10.1103/PhysRevLett.108.131801, arXiv:1112.6353.
- [49] F. P. An et al., Observation of electron-antineutrino disappearance at Daya Bay, Physical Review Letters, 108, 171803 (2012), doi:10.1103/PhysRevLett.108.171803, arXiv:1203.1669.
- [50] J. K. Ahn et al., Observation of Reactor Electron Antineutrino Disappearance in the RENO Experiment, Physical Review Letters, 108, 191802 (2012), doi:10.1103/PhysRevLett.108.191802, arXiv:1204.0626.
- [51] N. AGAFONOVA ET AL., Final Results of the OPERA Experiment on ν_{τ} Appearance in the CNGS Neutrino Beam, Physical Review Letters, 121, 139901 (2018), doi:10.1103/PhysRevLett.120.211801, arXiv:1804.04912.
- [52] K. ABE ET AL., Updated T2K measurements of muon neutrino and antineutrino disappearance using 3.6 × 10²¹ protons on target, Physical Reviews D, 108, 072011 (2023), doi:10.1103/PhysRevD.108.072011, arXiv:2305.09916.

[53] M. A. ACERO ET AL., Improved measurement of neutrino oscillation parameters by the NOvA experiment, Physical Reviews D, 106, 032004 (2022), doi:10.1103/PhysRevD.106. 032004, arXiv:2108.08219.

- [54] V. V. Barinov et al., Search for electron-neutrino transitions to sterile states in the BEST experiment, Physical Reviews C, 105, 065502 (2022), doi:10.1103/PhysRevC.105.065502, arXiv:2201.07364.
- [55] C. GIUNTI ET AL., Gallium Anomaly: critical view from the global picture of ν_e and $\overline{\nu_e}$ disappearance, Journal of High Energy Physics, 10 (2022), p. 164, doi:10.1007/JHEP10(2022)164, arXiv:2209.00916.
- [56] G. MENTION ET AL., The Reactor Antineutrino Anomaly, Physical Review D, 83, 073006 (2011), doi:10.1103/PhysRevD.83.073006, arXiv:1101.2755.
- [57] A. P. Serebrov et al., The result of the Neutrino-4 experiment, sterile neutrinos, dark matter and the Standard Model, (2023), arXiv:2306.09962.
- [58] C. ATHANASSOPOULOS ET AL., Evidence for $\nu_{\mu} \rightarrow \nu_{e}$ neutrino oscillations from LSND, Physical Review Letters, 81 (1998), pp. 1774–1777, doi:10.1103/PhysRevLett.81.1774, arXiv:nucl-ex/9709006.
- [59] A. AGUILAR ET AL., Evidence for neutrino oscillations from the observation of $\bar{\nu}_e$ appearance in a $\bar{\nu}_{\mu}$ beam, Physical Reviews D, 64, 112007 (2001), doi:10.1103/PhysRevD. 64.112007, arXiv:hep-ex/0104049.
- [60] A. A. AGUILAR-AREVALO ET AL., Updated MiniBooNE neutrino oscillation results with increased data and new background studies, Physical Reviews D, 103, 052002 (2021), doi:10.1103/PhysRevD.103.052002, arXiv:2006.16883.
- [61] P. ABRATENKO ET AL., Search for an Excess of Electron Neutrino Interactions in MicroBooNE Using Multiple Final-State Topologies, Physical Review Letters, 128, 241801 (2022), doi:10.1103/PhysRevLett.128.241801, arXiv:2110.14054.
- [62] M. A. Acero et al., White Paper on Light Sterile Neutrino Searches and Related Phenomenology, (2022), arXiv:2203.07323.
- [63] B. Armbruster et al., Upper limits for neutrino oscillations muon-anti-neutrino —> electron-anti-neutrino from muon decay at rest, Physical Review D, 65, 112001 (2002), doi:10.1103/PhysRevD.65.112001, arXiv:hep-ex/0203021.
- [64] A. P. SEREBROV ET AL., Search for sterile neutrinos with the Neutrino-4 experiment and measurement results, Physical Review D, 104, 032003 (2021), doi:10.1103/PhysRevD. 104.032003, arXiv:2005.05301.

[65] Y. DECLAIS ET AL., Search for neutrino oscillations at 15-meters, 40-meters, and 95-meters from a nuclear power reactor at Bugey, Nuclear Physics B, 434 (1995), pp. 503-534, doi:10.1016/0550-3213(94)00513-E.

- [66] Y. J. KO ET AL., Sterile Neutrino Search at the NEOS Experiment, Physical Review Letters, 118, 121802 (2017), doi:10.1103/PhysRevLett.118.121802, arXiv:1610.05134.
- [67] J. ASHENFELTER ET AL., First search for short-baseline neutrino oscillations at HFIR with PROSPECT, Physical Review Letters, 121, 251802 (2018), doi:10.1103/PhysRevLett.121.251802, arXiv:1806.02784.
- [68] H. Almazán et al., STEREO neutrino spectrum of ²³⁵U fission rejects sterile neutrino hypothesis, Nature, 613 (2023), pp. 257–261, doi:10.1038/s41586-022-05568-2, arXiv:2210.07664.
- [69] C. Rubbia, The Liquid Argon Time Projection Chamber: A New Concept for Neutrino Detectors, (1977).
- [70] C. VIGNOLI ET AL., *ICARUS 600 ton: A status report*, Nuclear Physics B Proceedings Supplements, 85 (2000), pp. 119–124, doi:10.1016/S0920-5632(00)00493-X.
- [71] M. Antonello et al., Experimental search for the "LSND anomaly" with the ICARUS detector in the CNGS neutrino beam, European Physical Journal C, 73 (2013), p. 2345, doi:10.1140/epjc/s10052-013-2345-6, arXiv:1209.0122.
- [72] R. Acciarri et al., A Proposal for a Three Detector Short-Baseline Neutrino Oscillation Program in the Fermilab Booster Neutrino Beam, (2015), arXiv:1503.01520.
- [73] P. A. MACHADO, O. PALAMARA, AND D. W. SCHMITZ, *The Short-Baseline Neutrino Program at Fermilab*, Annual Review of Nuclear and Particle Science, 69 (2019), pp. 363–387, doi:10.1146/annurev-nucl-101917-020949, arXiv:1903.04608.
- [74] A. A. AGUILAR-AREVALO ET AL., The Neutrino Flux Prediction at MiniBooNE, Physical Reviews D, 79, 072002 (2009), doi:10.1103/PhysRevD.79.072002, arXiv:0806.1449.
- [75] R. Acciarri et al., Long-Baseline Neutrino Facility (LBNF) and Deep Underground Neutrino Experiment (DUNE): Conceptual Design Report, Volume 2: The Physics Program for DUNE at LBNF, (2015), arXiv:1512.06148.
- [76] R. Acciarri et al., Long-Baseline Neutrino Facility (LBNF) and Deep Underground Neutrino Experiment (DUNE): Conceptual Design Report, Volume 1: The LBNF and DUNE Projects, (2016), arXiv:1601.05471.
- [77] P. Abratenko et al., First Measurement of Inclusive Muon Neutrino Charged Current Differential Cross Sections on Argon at $E_{\nu} \sim 0.8$ GeV with the MicroBooNE Detector,

Physical Review Letters, 123, 131801 (2019), doi:10.1103/PhysRevLett.123.131801, arXiv:1905.09694.

- [78] P. Adamson et al., The NuMI Neutrino Beam, Nuclear Instruments and Methods in Physics Research A, 806 (2016), pp. 279–306, doi:10.1016/j.nima.2015.08.063, arXiv:1507.06690.
- [79] M. G. CATANESI ET AL., Particle identification algorithms for the HARP forward spectrometer, Nuclear Instruments and Methods in Physics Research A, 572 (2007), pp. 899–921, doi:10.1016/j.nima.2006.11.071.
- [80] M. DIWAN, M. POTEKHIN, B. VIREN, X. QIAN, AND C. ZHANG, A novel method for event reconstruction in Liquid Argon Time Projection Chamber, Journal of Physics: Conference Series, 762 (2016), p. 012033, doi:10.1088/1742-6596/762/1/012033.
- [81] M. Antonello et al., Experimental observation of an extremely high electron lifetime with the ICARUS-T600 LAr-TPC, Journal of Instrumentation, 9 (2014), p. P12006, doi:10.1088/1748-0221/9/12/P12006, arXiv:1409.5592.
- [82] S. AMERIO ET AL., Design, construction and tests of the ICARUS T600 detector, Nuclear Instruments and Methods in Physics Research A, 527 (2004), pp. 329–410, doi:10.1016/j.nima.2004.02.044.
- [83] L. Bagby et al., New read-out electronics for ICARUS-T600 liquid Argon TPC. Description, simulation and tests of the new front-end and ADC system, Journal of Instrumentation, 13 (2018), p. P12007, doi:10.1088/1748-0221/13/12/P12007, arXiv:1805.03931.
- [84] M. Antonello et al., Precise 3D track reconstruction algorithm for the ICARUS T600 liquid argon time projection chamber detector, Advanced in High Energy Physics, 2013 (2013), p. 260820, doi:10.1155/2013/260820, arXiv:1210.5089.
- [85] L. Bagby et al., Overhaul and Installation of the ICARUS-T600 Liquid Argon TPC Electronics for the FNAL Short Baseline Neutrino Program, Journal of Instrumentation, 16 (2021), p. P01037, doi:10.1088/1748-0221/16/01/P01037, arXiv:2010.02042.
- [86] M. ARTERO PONS, Study of the reconstruction of ν_{μ} CC QE events from the Booster Neutrino Beam with the ICARUS detector, PhD Thesis, Università degli Studi di Padova, 2024, https://hdl.handle.net/11577/3512958.
- [87] B. Ali-Mohammadzadeh et al., Design and implementation of the new scintillation light detection system of ICARUS T600, Journal of Instrumentation, 15 (2020), p. T10007, doi:10.1088/1748-0221/15/10/T10007, arXiv:2006.05261.

[88] M. Bonesini et al., The laser diode calibration system of the ICARUS T600 detector at FNAL, Journal of Instrumentation, 15 (2020), p. C05042, doi:10.1088/1748-0221/15/05/C05042, arXiv:2003.12883.

- [89] F. Poppi, The Cosmic Ray Tagger system of the ICARUS detector at Fermilab, Proceeding of Science, ICHEP2022 (2022), p. 580, doi:10.22323/1.414.0580.
- [90] K. Biery et al., artdaq: An Event-Building, Filtering, and Processing Framework, IEEE Transactions on Nuclear Science, 60 (2013), pp. 3764 3771, doi:10.1109/TNS. 2013.2251660.
- [91] E. L. SNIDER AND G. PETRILLO, LArSoft: Toolkit for Simulation, Reconstruction and Analysis of Liquid Argon TPC Neutrino Detectors, Journal of Physics: Conference Series, 898 (2017), p. 042057, doi:10.1088/1742-6596/898/4/042057.
- [92] C. Adams et al., Ionization electron signal processing in single phase LArTPCs. Part I. Algorithm Description and quantitative evaluation with MicroBooNE simulation, Journal of Instrumentation, 13 (2018), p. P07006, doi:10.1088/1748-0221/13/07/P07006, arXiv:1802.08709.
- [93] C. Adams et al., Ionization electron signal processing in single phase LArTPCs. Part II. Data/simulation comparison and performance in MicroBooNE, Journal of Instrumentation, 13 (2018), p. P07007, doi:10.1088/1748-0221/13/07/P07007, arXiv:1804.02583.
- [94] J. S. MARSHALL AND M. A. THOMSON, The Pandora software development kit for particle flow calorimetry, Journal of Physics: Conference Series, 396 (2012), p. 022034, doi:10.1088/1742-6596/396/2/022034.
- [95] R. Acciarri et al., The Pandora multi-algorithm approach to automated pattern recognition of cosmic-ray muon and neutrino events in the MicroBooNE detector, The European Physical Journal C, 78 (2018), p. 82, doi:10.1140/epjc/s10052-017-5481-6, arXiv:1708.03135.
- [96] R. L. WORKMAN ET AL., *Review of Particle Physics*, Progress of Theoretical and Experimental Physics, 2022 (2022), p. 083C01, doi:10.1093/ptep/ptac097.
- [97] H. BICHSEL, Straggling in Thin Silicon Detectors, Reviews of Modern Physics., 60 (1988), pp. 663–699, doi:10.1103/RevModPhys.60.663.
- [98] G. Putnam and D. W. Schmitz, Effect of diffusion on the peak value of energy loss observed in a LArTPC, Journal of Instrumentation, 17 (2022), p. P10044, doi:10.1088/ 1748-0221/17/10/P10044, arXiv:2205.06745.
- [99] P. ABRATENKO ET AL., Measurement of space charge effects in the MicroBooNE LArTPC using cosmic muons, Journal of Instrumentation, 15 (2020), p. P12037, doi:10.1088/1748-0221/15/12/P12037, arXiv:2008.09765.

[100] R. ACCIARRI ET AL., A Study of Electron Recombination Using Highly Ionizing Particles in the ArgoNeuT Liquid Argon TPC, Journal of Instrumentation, 8 (2013), p. P08005, doi:10.1088/1748-0221/8/08/P08005, arXiv:1306.1712.

- [101] J. B. BIRKS, Scintillations from Organic Crystals: Specific Fluorescence and Relative Response to Different Radiations, Proceedings of the Physical Society A, 64 (1951), pp. 874–877, doi:10.1088/0370-1298/64/10/303.
- [102] P. Abratenko et al., Angular dependent measurement of electron-ion recombination in liquid argon for ionization calorimetry in the ICARUS liquid argon time projection chamber, (2024), arXiv:2407.12969.
- [103] D. E. GROOM ET AL., Muon stopping power and range tables 10-MeV to 100-TeV, Atomic Data and Nuclear Data Tables, 78 (2001), pp. 183–356, doi:10.1006/adnd.2001. 0861.
- [104] J.-M. Alameddine et al., *The particle-shower simulation code CORSIKA 8*, PoS, ICRC2023 (2023), p. 310, doi:10.22323/1.444.0310, arXiv:2308.05475.
- [105] S. AGOSTINELLI ET AL., *GEANT4-a simulation toolkit*, Nuclear Instruments and Methods in Physics Research A, 506 (2003), pp. 250–303, doi:10.1016/S0168-9002(03) 01368-8.
- [106] C. Andreopoulos et al., The GENIE Neutrino Monte Carlo Generator: Physics and User Manual, (2015), arXiv:1510.05494.
- [107] M. BONESINI ET AL., An innovative technique for TPB deposition on convex window photomultiplier tubes, Journal of Instrumentation, 13 (2018), p. P12020, doi:10.1088/ 1748-0221/13/12/P12020, arXiv:1807.07123.
- [108] R. VEENHOF, GARFIELD, recent developments, Nuclear Instruments and Methods in Physics Research A, 419 (1998), pp. 726–730, doi:10.1016/S0168-9002(98)00851-1.
- [109] H. KOLANOSKI AND N. WERMES, Particle Detectors, Oxford University Press, 6 2020.
- [110] W. R. Leo, Techniques for Nuclear and Particle Physics Experiments, Springer, 1994, doi:10.1007/978-3-642-57920-2.
- [111] E. Keil, E. Zeitler, and W. Zinn, SINGLE AND PLURAL SCATTERING OF CHARGED PARTICLES, (1960).
- [112] G. Moliere, Theorie der Streuung schneller geladener Teilchen I. Einzelstreuung am abgeschirmten Coulomb-Feld, Zeitschrift für Naturforschung A, 2 (1947), p. 133.
- [113] V. L. HIGHLAND, Some Practical Remarks on Multiple Scattering, Nuclear Instruments and Methods, 129 (1975), p. 497, doi:10.1016/0029-554X(75)90743-0.

[114] A. Ankowski et al., Measurement of through-going particle momentum by means of multiple scattering with the ICARUS T600 TPC, Eur. Phys. J. C, 48 (2006), pp. 667–676, doi:10.1140/epjc/s10052-006-0051-3, arXiv:hep-ex/0606006.

- [115] M. Antonello et al., Muon momentum measurement in ICARUS-T600 LAr-TPC via multiple scattering in few-GeV range, Journal of Instrumentation, 12 (2017), p. P04010, doi:10.1088/1748-0221/12/04/P04010, arXiv:1612.07715.
- [116] P. ABRATENKO ET AL., Determination of muon momentum in the MicroBooNE LArTPC using an improved model of multiple Coulomb scattering, Journal of Instrumentation, 12 (2017), p. P10010, doi:10.1088/1748-0221/12/10/P10010, arXiv:1703.06187.